Modeling Magnetic Nanoparticles: Application to Hyperthermia

by

© **Razyeh Behbahani**

A thesis submitted to the School of Graduate Studies in partial fulfillment of the requirements for the degree of Doctor of Philosophy.

Department of Physics and Physical Oceanography

Memorial University of Newfoundland

October 2021

St. John's, Newfoundland and Labrador, Canada

Abstract

Using the Landau-Lifshitz-Gilbert (LLG) equation in micromagnetic simulations, we model magnetic nanoparticles composed of nanorods for application in magnetic nanoparticle hyperthermia, a developing cancer treatment. We use a scaling approach based on the renormalization group (RG) to calculate magnetization-field hysteresis loops that are invariant with simulation cell size, with the objective of decreasing the simulation time at clinically relevant field parameters. In addition, we introduce a time scaling approach that involves the sweep rate of the oscillating external field and the damping constant α in the LLG equation, which allows for up to three orders of magnitude faster simulations. Equipped with the RG and time scaling tools, we explore a macrospin model in which a complex nanoparticle is represented by a single magnetization vector with appropriate effective magnetic parameters. To evaluate this model, we calculate loops for single particles and particles interacting in pairs, chains and triangles of three particles, and in a cluster of thirteen nanoparticles. Motivated by recent experimental studies that reported successful hyperthermia treatment in the absence of perceptible heating of tissue, we report on local hysteresis loops of individual nanoparticles within clusters, highlighting the role of magnetostatic interactions between nanoparticles in the complex heating and magnetization dynamics of groups of nanoparticles.

To those who sacrifice their comfort to make the world a better place!

Acknowledgements

I would like to express my deep and sincere gratitude to my supervisors, Dr. Ivan Saika-Voivod and Dr. Martin Plumer for giving me the opportunity to do research under their supervision and providing invaluable guidance throughout my PhD.

I could not imagined having better advisors and mentors in my life. They motivate me with their marvelous training, encouragement and support and I have been blessed with their kindness and good-will beyond what one gets even from their family. I will be in debt all my life and endeavour to pass on to others at least part of the kindheartedness I received.

I also thank my supervision committee members, Dr. Kristin Poduska and Dr. Mykhaylo Evstigneev, for their support during my PhD. I would like to thank Dr. Johan van Lierop for his input on defining the research problem and sharing his experience in magnetic hyperthermia. I also thank Dr. Martin Leblanc, my mentor for the first two years of my PhD, who was a big help especially when I started using OOMMF and Compute Canada. I also appreciate the help I received from Dr. Shahrazad Malek in scripting and her friendship. I would like to thank Dr. Amir Taheridehkordi for his friendship and productive discussions we had during my course work. I would like to thank Dr. Mikko Karttunen who hosted my stay in his group at Western University as a visiting graduate student and his practical suggestions for the project and presentations.

I thank Michael J. Donahue for discussions and his expert guidance on how to vary magnetostatic interactions while keeping other interaction strengths fixed within OOMMF, and thank Jonathan Leliaert for his guidance on employing the new version of Vinamax. I would like to thank Dr. Hossein Abbasi, Dr. Hosein Aghahosseini Naeini and Dr. Peyman Nayebi who familiarized me with the world of magnetism, introduced me to computational physics and kindly supported me on the way to

starting doctoral studies.

I appreciate my parents' devotion for withstanding my absence when I left to follow my dreams, and special thanks go to my husband, Ali, for his heartwarming company, support and encouragement.

Statement of contributions

This is a manuscript style thesis comprised of two peer-reviewed papers published in the Journal of Physics Condensed Matter, and one manuscript in preparation. The thesis author (Razyeh Behbahani) is the main contributor for all of the manuscripts included in this thesis, sharing authorship with Dr. Ivan Saika-Voivod and Dr. Martin Plumer, the co-supervisors for this graduate project. The first paper is entitled *Coarse-graining in micromagnetic simulations of dynamic hysteresis loops*, and was published in June 2020 (Ch. 3), as a letter. The second is *Multiscale modelling of magnetostatic effects on magnetic nanoparticles with application to hyperthermia*, published in April 2021 (Ch. 4), and the third one, entitled *Micromagnetic simulation of clusters of nanoparticles*, is in preparation (Ch. 5). In all three works, Dr. Saika-Voivod and Dr. Plumer provided guidance for checking the results of the computer codes, analyzing data and writing the manuscripts. As the main contributor, Razyeh Behbahani wrote the analysis codes used in this thesis, carried out literature reviews and wrote first drafts of the manuscripts. The published manuscripts resulted from a back-and-forth process of writing and editing between student and co-supervisors.

IOP, the publisher of our articles, allows for the inclusion of published articles within a thesis. From https://publishingsupport.iopscience.iop.org/permissions-faqs/

> Upon transfer of copyright, IOP and/or the copyright owner grants back to authors a number of rights. These include the right to include the Final Published Version of the article in your research thesis or dissertation. Please include citation details and, for online use, a link to the Version of Record.

Table of contents

Title page i

Abstract ii

Acknowledgements iv

Statement of contributions vi

Table of contents vii

List of tables xi

List of figures xii

List of symbols xv

List of abbreviations xvii

1 Introduction 1

1.1 Hyperthermia and the motivation for this study 1

1.2 Magnetic materials 3

1.3 Heating 5

1.3.1 General discussion 5

1.3.2 Heat calculations 10

1.4 Magnetic structure and interactions . . . 13
1.4.1 Crystal structure of Fe_3O_4 . . . 13
1.4.2 Zeeman Energy . . . 15
1.4.3 Exchange Interactions . . . 15
1.4.4 Anisotropy . . . 19
1.4.4.1 Magneto-crystalline anisotropy . . . 19
1.4.4.2 Surface anisotropy . . . 20
1.4.4.3 Shape anisotropy . . . 22
1.4.5 Dipole Interactions . . . 23
1.5 Micromagnetics . . . 25
1.6 Magnetic properties of Fe_3O_4 . . . 28
1.7 Hyperthermia . . . 29
1.7.1 Experimental studies . . . 29
1.7.2 Simulations . . . 33
1.8 Model of study . . . 36
1.9 Outline . . . 37

Bibliography **40**

2 Methods **46**

2.1 Stoner-Wohlfarth model . . . 47
2.1.1 Analytical solution for SW model at $T = 0$ . . . 49
2.1.2 Approximate analytical solution for the SW model at finite T . . . 51
2.2 Magnetization dynamics with LLG equation and numerical solution . . . 53
2.2.1 Numerical schemes . . . 55
2.2.2 Our code for a single SW particle . . . 57
2.2.3 OOMMF software for multiple moments . . . 59

2.2.3.1 Heisenberg model: finding the exchange constant A using T_c 60
2.2.4 Coarse-graining 63
2.2.4.1 Renormalization Group 64
2.2.4.2 Momentum shell Renormalization Group 67
2.2.4.3 Grinstein and Koch's RG approach 72

Bibliography **75**

3 Coarse-graining in micromagnetic simulations of dynamic hysteresis loops **77**

3.1 Introduction 78
3.2 The model 79
3.3 Coarse-graining 82
3.4 SR/α scaling 88
3.5 Conclusions 90

Bibliography **92**

4 Multiscale modelling of magnetostatic effects on magnetic nanoparticles with application to hyperthermia **96**

4.1 Introduction 97
4.2 The model 101
4.3 Coarse-graining and demagnetization 104
4.4 Coarse-graining for multiple nanorods 111
4.5 Nanoparticles 113
4.6 Interacting nanoparticles 116
4.7 Conclusions 118

Bibliography **126**

5 Micromagnetic simulation of clusters of nanoparticles **131**

5.1 Introduction 132

5.2 The model 136

5.3 Effective anisotropy in complex NPs 139

5.4 Multiple NP heating efficiency 143

5.4.1 Chained particles 143

5.4.2 Triangular order: when the internal structure matters 144

5.4.3 NPs in an FCC structure 146

5.5 Local vs global loops 149

5.5.1 Chains and triangles 150

5.5.2 FCC structure 153

5.6 SR/α scaling for multiple NPs 155

5.7 Conclusions 159

Bibliography **162**

6 Summary and future work **167**

6.1 Summary 167

6.2 Future work 169

Bibliography **173**

A Magnetostatics Induced Shape Anisotropy **174**

Bibliography **180**

List of tables

1.1 Experimental parameters for MNPH in the Dennis et al. study 30

4.1 The K_{eff} and $M_{\text{s}}^{\text{eff}}$ of MSs equivalent to simulated nanorods and NPs . 111

5.1 Particle coordinates at FCC structure 154

List of figures

1.1 a) A typical hysteresis loop, b) major and minor loops 7

1.2 Fe_3O_4 crystal structure 14

1.3 Surface anisotropy effects for small spherical NPs 21

1.4 Dipole interactions 24

1.5 Comparing magnetic field of a bar magnet and a magnetic dipole . . . 27

1.6 Tumour volume change under application of MNPs and AMF in an experimental study 31

1.7 SLP as a function of field parameters and direction for Resovist, γ-Fe_2O_3 and Fe_3O_4 32

1.8 The effect of shape anisotropy on the coercivity 33

1.9 Hysteresis loops for magnetite NPs with different aspect ratios 34

1.10 Hysteresis loops for different particle sizes in different field parameters . 35

1.11 Simulation model of nanoparticles made of nanorods 36

2.1 Stoner-Wohlfarth (SW) particle a) diagram b) energy profile 48

2.2 Individual and average hysteresis loops for different directions of applied field on a single magnetization vector 50

2.3 Schematic sketch of the Euler and RK4 integration schemes 57

2.4 SW particle spin dynamics from numerical integration of the LLG Eq, showing a) the effect of damping, and b) a comparison of Euler and RK4 solvers. 58

2.5 Comparing results from OOMMF and our own code for a single SW particle . . . 59

2.6 Comparing simulation results from OOMMF with analytical solutions for SW model at zero and finite T . . . 61

2.7 Heisenberg model a) $m - T$ b) $\chi - T$. . . . 62

3.1 Simulation model of nanorods comprised of different size micromagnetic cells . . . 80

3.2 Hysteresis loop of nanorods made of different size cells before and after RG coarse graining at $T = 310$ K . . . 83

3.3 Modified $M(b)$ accounts for more accurate description of $M(T)$ . . . 86

3.4 Invariance of MH loops with combined RG scaling of magnetic quantities, larger time step with block size, and SR/α scaling . . . 89

4.1 Coarse-graining model of a magnetite nanorod, building block of NPs . 101

4.2 Nanorods hysteresis loops before and after applying the modified RG coarse graining, and extending it to include magnetostatics . . . 105

4.3 MS model equivalent to Fe_3O_4 and γ-Fe_2O_3 nanorods . . . 110

4.4 RG coarse graining for a bundle of 8 nanorods . . . 112

4.5 NPs composed of 10 nanorods with different arrangements as $10z$, $8z2y$ and $6z4y$ and equivalent MSs . . . 113

4.6 Applied field direction on NPs determines the effective anisotropy of equivalent MSs . . . 115

4.7 Hysteresis loops of two magnetite $6z4y$ NPs as a function of interparticle distance compared to their equivalent MSs . . . 117

4.8 Dependence of MH loops on Δt for nanorods composed of cells of side length ba_0 for $b = 1, 2, 4, 8$ . . . 121

4.9 Effect of inter-rod magnetostatic and exchange interactions . . . 125

5.1 Impact of two uniaxial anisotropies on the hysteresis loop of the MS model . . . 140

5.2 Loop area comparison for NPs and equivalent MSs with single and double uniaxial anisotropies . . . 141

5.3 Effect of anisotropy axis distribution on a NP hysteresis loop . . . 142

5.4 Hysteresis loops of three chained NPs and equivalent MSs as a function of interparticle distance . . . 143

5.5 Hysteresis loops of three NPs and equivalent MSs in triangular order as a function of interparticle distance . . . 145

5.6 Loop area as a function of inter-particle distance for three NPs and MSs in triangular order . . . 146

5.7 Loop comparison of three NPs and MSs, with different anisotropy orders, arranged in a triangle of side length $2.5d$. . . . 147

5.8 Hysteresis loops of NPs and MSs in an FCC structure as a function of interparticle distance . . . 148

5.9 Loop area as a function of particle distance for clusters of complex NPs and MSs in an FCC structure. . . . 149

5.10 Local hysteresis loops for three MSs in a chain and triangular orders . . 151

5.11 Local hysteresis loops for MSs in an FCC structure at closest interparticle distance ($r = d$) . . . 156

5.12 Local hysteresis loops for MSs in an FCC structure, when $r = 1.5d$ . . . 157

5.13 Test of SR/α scaling for NP simulations in OOMMF . . . 158

5.14 Test of SR/α scaling for MS simulations in Vinamax . . . 159

A.1 Magnetostatics effect on the hysteresis loop compared to the uniaxial anisotropie's impact at zero and finite T . . . 179

List of symbols

α	Damping constant
γ	Gyromagnetic ratio
δ	Domain wall width
ζ	RG scaling factor
η	Damping coefficient
$\boldsymbol{\mu}$	Magnetic moment
μ_0	Vaccume permeability
μ_B	Bohr magneton
ρ	Mass density
σ	Domain wall energy per unit area
τ_M	Measurement characteristic time
τ_R	Reversal characteristic time
χ	Magnetic susceptibility
ω	Angular frequency
A	Exchange constant
D	Exchange stiffness constant
f	Frequency
g	Electron g-factor
H_0	Magnetic field amplitude
H_k	Anisotropy field
H_d	Demag field
H_c	Coercive field (Coercivity)
J_AA, J_AB, J_BB	Exchange integrals
k_B	Boltzmann constant
K	Anisotropy energy density
K_c	Cubic anisotropy energy density
K_S	Surface anisotropy energy density
K_sh	Shape anisotropy energy density
K_u	Uniaxial anisotropy energy density
K_V	Bulk material anisotropy energy density
l_ex	exchange length

M_s	Saturation magnetization
M_r	Remanent magnetization
$\mathbf{N}$	Demagneitization tensor
$N_\perp$	Demag factor perpendicular to the rotational symmetry axis
$N_\parallel$	Demag factor along the rotational symmetry axis
r_c	Critical size
t	time
T	Temperature in kelvins
T_N	Néel temperature
T_c	Critical temperature
T_C	Curie temperature
T_V	Verwey temperature

List of abbreviations

2D	two dimensional
AC	Alternating current
AMF	Alternating magnetic field
DC	Direct current
FCC	Face centered cubic
LLG	Landau-Lifshitz-Gilbert
MH	Magnetization–Magnetic Field, as in MH hysteresis loop
MION	Magnetic iron oxide nanoparticle
MNH	Magnetic nanoparticle hyperthermia
MNP	Magnetic nanoparticle
MRI	Magnetic Resonance Imaging
MS	Macrospin
NP	Nanoparticle
ODE	Ordinary differential equation
OOMMF	Object oriented micromagnetic framework
RG	Renormalization group
RK4	4th-order Runge–Kutta
SLP	Specific loss power
SAR	Specific absorption rate
SPM	Superparamagnetic
SR	Sweep rate
sLLG	Stochastic Landau-Lifshitz-Gilbert
SW	Stoner–Wohlfarth
TEM	Transmission electron microscopy

Chapter 1

Introduction

1.1 Hyperthermia and the motivation for this study

Curing diseases like cancer, with no universally effective treatment protocol, has inspired many research studies. Beyond the current standard treatments, including surgery, chemotherapy, and radiotherapy, new therapies such as thermo-therapy are being investigated. Thermo-therapy is based on exploiting the higher sensitivity of cancerous tissues to heat compared to normal tissues. Due to the particular tissue structure of tumors, they undergo cell death at temperatures in the range $41-46°C$ [1]. Magnetic nanoparticle hyperthermia (MNH) is a type of thermo-therapy that uses magnetic nanoparticles to increase the tumour tissue's temperature. Magnetic nanoparticles are delivered to the tumour, either through targeting* or direct injection, and are subjected to an alternating magnetic field (AMF).

The potential of selective heating without consequential side effects makes hyperthermia a promising option compared to conventional cancer treatments. Moreover,

*Targeting refers to increasing the concentration of nanoparticles at the tumour, e.g. by trapping them magnetically, or coating them with molecules that preferentially bind to the tumour [2].

magnetic hyperthermia can be used as a secondary treatment to enhance the efficiency of primary treatments like chemotherapy and radiotherapy [3–6]; heating tumor tissue increases blood perfusion and leads to greater chemotherapy drug delivery and supplies higher reactive oxygen species, which makes tumors more sensitive to radiotherapy [7, 8].

This method is promising for its potential precise control of dose and tissue specificity. Pre-clinical studies point to the requirement of selective and homogeneous heat generation, as insufficient temperature increase in parts of the tumor can trigger multiplication of surviving tumor cells [9], while overheating can damage healthy surrounding tissues. Providing sufficient magnetic material and applying AMF with suitable parameters for conducting a non-injurious and highly efficient treatment is challenging. Therefore, understanding the primary effectual parameters for heat production in magnetic nanoparticles is necessary for developing an optimized hyperthermia treatment.

In MNH, choosing an efficient magnetic material that is biocompatible is the first concern. Among magnetic materials, Co and Ni are highly magnetic but also toxic. In contrast, an average human adult carries $3.5-4$ grams of iron, which is an essential element for red blood cells, and iron oxide nanoparticles, in particular magnetite (Fe_3O_4) or maghemite (γ-Fe_2O_3), are commonly used on account of their lower toxicity [7]. Also, it is desirable to elevate the temperature with as few nanoparticles as possible, i.e., to have higher heat generation per unit mass of particles. Magnetic nanoparticles' (MNP) heat generation under application of an alternating current (AC) field can be through different processes such as magnetization reversal, called Néel relaxation, or NPs rotation, called Brownian relaxation, or through eddy currents (see section 1.3).

The heating efficiency, usually measured in terms of the specific loss power (SLP),

also referred to as specific absorption rate (SAR), depends on the MNP properties, such as their size, shape, magnetocrystalline anisotropy and saturation magnetization, as well as the frequency (f) and amplitude (H_0) of the applied field. Higher values of f and H_0 result in higher SLP. However, medical restrictions limit the applicable values to avoid collateral tissue damages due to unwanted heating through eddy currents.

In this thesis, the goal is to simulate the magnetic response of magnetite nanoparticles to an AMF that gives rise to heating. Our model for the MNPs reflects those used in an experimental study, which were roughly spherical assemblies of fairly long and narrow nanorods (rectangular prisms) [10]. This chapter provides a brief review of the physical concepts pertaining to magnetic materials, a summary of possible heating mechanisms and heat calculations, followed by magnetic structure and interactions that need to be considered. Then, after a brief review of selected literature on hyperthermia, we describe the model we study through micromagnetic simulation.

1.2 Magnetic materials

Magnetism emerges from motions of electrically charged particles. Orbital and spin properties of atomic electric charge, as well as spin-orbit coupling, produces the so-called magnetic moment of the material [11].

A major factor that defines the magnetic properties of a material is the exchange interaction. For example, ferromagnets and antiferromagnets show strong negative and positive exchange interactions favoring parallel and antiparallel spins, respectively. Above a material's critical temperature, thermal fluctuations overcome all the exchange interactions, and the material loses magnetic order, becoming a paramagnet. Materials with no exchange interactions are generally divided into diamagnets

and paramagnets.

Identification of different types of magnetic materials is based on their magnetic status below their critical temperature. Materials with no net magnetic moments in zero applied field include diamagnets, paramagnets, and antiferromagnets. In contrast, ferromagnets and ferrimagnets have a net magnetic moment even in zero applied field.

Diamagnetism arises from the paired electrons in the material for which the spin and angular momenta counteract each other (total angular momentum quantum number $J = 0$). Diamagnetism can be understood qualitatively from a classical perspective. An external magnetic field will tend to cause moving charges to undergo circular motion. This circular motion can be thought of in terms of a current in a loop, which in turn will give rise to a magnetic field, one which opposes the external field. Therefore, all materials have some degree of diamagnetism due to their electron pairs, and this is not highly temperature-dependent. In the absence of effects arising from unpaired electrons, only the diamagnetic response is present, and such materials are termed diamagnetic.

In contrast, paramagnetism arises from unpaired electrons ($J \neq 0$), the magnetic moment of which align with the applied field, providing a net magnetic moment that dominates their negative diamagnetic response. With no exchange interactions, individual atomic magnetic moments do not align in the absence of an external field, leading to zero net magnetic moment.

Antiferromagnets have a strong positive exchange interaction, resulting in antiparallel order of neighbouring magnetic moments in the absence of a magnetic field. This results in zero net magnetization for the material below its critical temperature, which is called Néel temperature (T_{N}) in this case. A strong magnetic field can overcome

the exchange interactions and align the magnetic moments to the field.

Moreover, other classes, including ferromagnets and ferrimagnets, have a net magnetic moment with or without exposure to an external magnetic field. Ferromagnets have a strong negative exchange interaction that induces parallel alignment of neighbouring magnetic moments and a net magnetic moment below the critical temperature, called the Curie temperature (T_C). Applying a magnetic field aligns the magnetic moments of the material parallel to the field. Ferrimagnets are similar to the antiferromagnets, except neighboring antiparallel magnetic moments have different magnitudes; consequently, there is a net magnetic moment below T_C. In other words, ferrimagnets can be considered as weaker ferromagnets [12]. However, an applied magnetic field can overcome the exchange interactions in ferrimagnets and align the magnetic moments to the external magnetic field. Two magnetic iron oxides of interest for hyperthermia applications, magnetite, Fe_3O_4, and maghemite, γ-Fe_2O_3, are ferrimagnets.

1.3 Heating

1.3.1 General discussion

The key feature of magnetic NPs is embedded in their response to an applied magnetic field. Nanoparticles smaller than 50 nm are generally single domain, and their magnetization tends to align with the applied field. This alignment can occur via different rotation mechanisms. A common process involves a particle's magnetic moment rotating inside the particle to align with the field through so-called Néel relaxation. The delayed response of the magnetic moment (M) in aligning with the changing field (H) is quantified through an MH hysteresis loop, and the enclosed area of the loop is

a measure of the magnetic energy added to the system, which is usually assumed to be dissipated as heat. Another process involves the whole particle rotating to align its magnetic moment with the field. This is called Brownian rotation, and the friction between NPs and the surrounding fluid molecules results in heating. The relevant aligning process is the one that occurs on a shorter time scale.

In the Néel process, the changing field alters the magnetization's stable positions and an energy barrier separates the energy minima due to magnetic crystalline anisotropy. When the size of NPs is smaller than $15 - 20$ nm, thermal fluctuations provide the required energy for the magnetization to flip before the whole nanoparticle rotates. So, for these particles, Néel relaxation is dominant and their Brownian rotation is usually ignored due to its longer relaxation time [13]. Various studies have used Néel-rotation particles for magnetic hyperthermia applications [13–21]. In contrast, for larger single domain nanoparticles, in the size range of $20 - 80$ nm, the Brownian and Néel relaxation times can be comparable [13, 22]. For the numerical study of the magnetization dynamics, micromagnetic software such as Object-Oriented MicroMagnetic Framework (OOMMF) [23], MuMax [24], and Vinamax [25] are widely used, which all simulate the magnetization of immobile particles.

The magnetization dynamics of ferro and ferrimagnets under exposure of an oscillating magnetic field, via the Néel relaxation, is investigated by analysing their MH hysteresis loops. As shown in Fig. 1.1a, loops yield important characteristic information about the material, such as its saturation magnetization (M_s), remanent magnetization (M_r), coercive field or coercivity (H_c), anisotropy energy density (K) and the characteristic response time of the system's magnetization to the changing field. M_s is the maximal magnetic moment per unit of volume, i.e., the magnetization in the high field limit. M_r is the magnetization that persists when the applied field

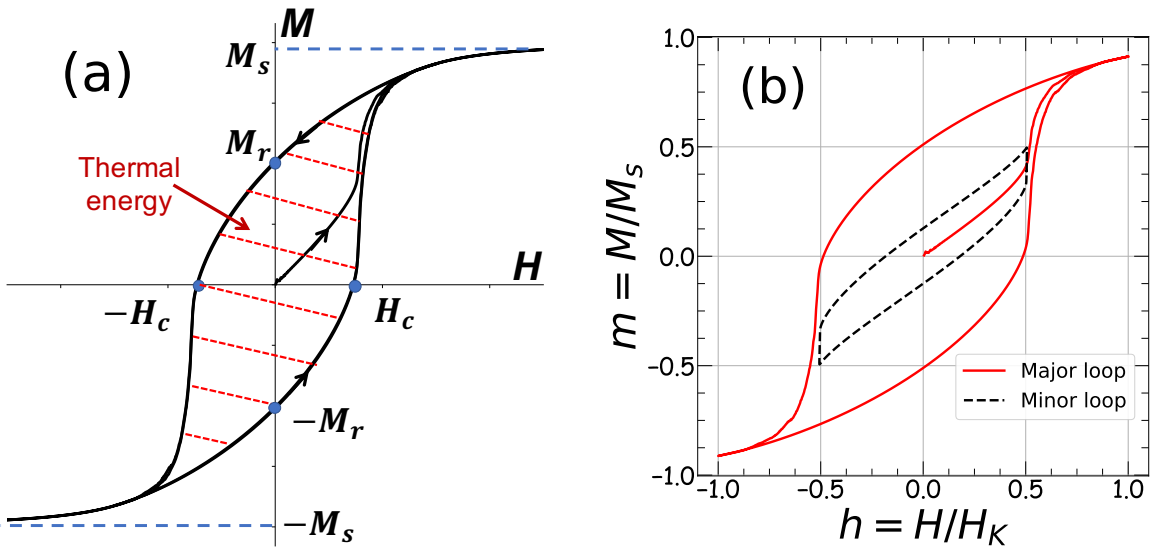

Figure 1.1: a) A typical hysteresis loop for a magnetic material under application of one cycle of an alternating magnetic field. b) Major and minor hysteresis loops based on the applied field amplitude ($T = 0$).

has decreased to zero. H_c is the magnetic field at which the magnetization falls to zero, or equivalently, the field required to reverse the magnetization. Hysteresis loops are a dynamic property and depend on the temperature and the characteristics of the applied field. In most cases, the loop features are determined by thermodynamically metastable magnetic states.

When a material has preferred directions for its magnetic moment it is said to display anisotropy. In the case of uniaxial anisotropy, there is a single preferred "easy axis". At $T = 0$, for the case where the field is applied along the easy axis, $H_c = H_k = 2K/(\mu_0 M_s)$, where μ_0 is the free space permeability. The quantity H_k is called the anisotropy field [26]. Various effects attribute to the anisotropy energy density, namely the matter's crystalline structure (providing so-called magnetocrystalline anisotropy), shape anisotropy (arising from magnetostatic interactions within non-spherical particles), the particle's surface anisotropy, and colloidal anisotropy (which

is an effect of other particles in the surrounding liquid – their aggregation can encourage a specific alignment for the magnetic moments) [12]. Magnetocrystalline, shape and surface anisotropy are discussed below in later sections.

Depending on the amplitude of the applied field, in comparison to the anisotropy field, hysteresis loops are divided into two main types, major and minor loops [12]. A major loop starts from a saturated magnetization state, goes to negative saturation, and then returns to the starting point. Generally, the field strength needed to reach the saturated state is $H \simeq H_k$. At $T = 0$, when the field is along the anisotropy axis, the MH loop is a rectangle with side lengths $2M_\mathrm{s}$ and $2H_k$, and the magnetization flips from M_s to $-M_\mathrm{s}$ at $H = -H_k$. This case gives the maximum loop area for the system, $4M_\mathrm{s}H_k$, which in turn dictates the maximum heat released from one loop cycle. If the maximum applied field magnitude is less than H_k, magnetization saturation will not occur, resulting in a minor loop, as shown in Fig. 1.1b. Note that in the figure, the loops are presented as averages over field directions with respect to the anisotropy axis, in which case $H_c = H_k/2$.

While exchange interactions favour spin alignment between neighbours, weaker but longer-range magnetostatic interactions can favour anti-alignment, and so having a large collection of aligned spins becomes energetically unfavourable at some length scale. The length scale of the magnetic moments' collective alignment is determined by the competition between exchange, anisotropy and magnetostatics (i.e., dipolar interactions). Ferromagnets are usually identified with materials that include magnetic domains separated by borders or so-called domain walls. Domain walls, which enclose regions where all the magnetic moments are aligned (apart from thermal fluctuations), form when the energy cost for enlarging the domain exceeds the energy cost for domain wall formation. When particles are small enough, only a single domain is

present. Different studies report that for magnetite, NPs below $70 - 100$ nm in size exhibit a single domain magnetic structure [27–29]. For particles exceeding 1000 nm in size, multidomain structures are observed, while for sizes between 100 and 1000 nm, intermediate vortex-like structures are reported [29]. In addition to the type of material, the single domain size limit depends on different factors, such as the shape of the particles, their synthesis methodology, and heat treatments [30]. These size regimes are consistent with an expression for domain wall width $\delta_{\text{bulk}} = \pi\sqrt{A/K}$ [11, 26], which evaluates to approximately 100 nm for magnetite (which has cubic anisotropy); a system needs to be significantly larger than δ to accommodate multiple domains.

For very small NPs of ferromagnetic (or ferrimagnetic) material, while they comprise a single domain, their response to an external field will be superparamagnetic (SPM), where the hysteresis curves are closed. Experimentally, this SPM response is observed for NPs smaller than $25 - 30$ nm [27, 28], and arises from the ability of thermal fluctuations at room temperature to effect spontaneous magnetization reversal on short-enough time scales. To understand this semi-quantitatively, we begin by noting that the energy barrier to magnetization reversal is approximately equal to KV. If this is on the order of thermal energy at room temperature, then $KV = k_{\text{B}}T$. For spherical particles, $V = 4\pi r^3/3$, at $T = 300$ K, of magnetite, $K = 10^4$ J/m^3, this corresponds to a diameter of approximately 10 nm [9], which approximately agrees with experimental observation. These SPM NPs exhibit closed hysteresis curves with zero M_r and H_c when the measurement time, τ_{M}, is longer than the reversal time, τ_{R}, the characteristic time for spontaneous magnetization flips. Hence, for small particles, the low-frequency regime that results in no hysteresis is called the SPM regime.

1.3.2 Heat calculations

An applied magnetic field tends to align magnetic moments in the field direction, and the degree of alignment depends on the field magnitude and material properties. By switching the polarity of an AC field, the magnetization direction also changes. The time between the field change and the magnetization response depends on the field characteristics like frequency and amplitude and particle properties such as anisotropy, temperature and size. The size dependence can be understood in the case when the exchange is strong, and all the spins in a small particle act as a single spin; in this limiting case, the energy barrier to magnetization flipping, due to anisotropy, is KV. The time lag of magnetization alignment in response to a changing field results in an open magnetization-field (MH) hysteresis loop. For an infinitesimal process, the work done on the sample, i.e., the energy that needs to be absorbed by the sample in order for moments to align with the field, is [12, 31],

$$dW = \mu_0 \mathbf{H} \cdot d\mathbf{M}, \tag{1.1}$$

and the thermodynamic identity becomes $dE = TdS + \mu_0 \mathbf{H} \cdot d\mathbf{M}$. From this, by considering the Gibbs free energy $G = E - TS - \mu_0 \mathbf{M} \cdot \mathbf{H}$,* one can obtain the reversible work done on the system due to an infinitesimal change in the field (at constant T) to be $dW = -\mu_0 \mathbf{M} \cdot d\mathbf{H}$. In a cycle of the AC field, the system returns to its initial state ($\Delta E = 0$) and conservation of energy implies the conversion of work into heat. The heat released by the magnetic sample into the environment is,

$$Q = -\mu_0 \oint \mathbf{M} \cdot d\mathbf{H}. \tag{1.2}$$

*Some authors refer to this expression for magnetic systems as the Helmholtz free energy.

Therefore, the enclosed area in the hysteresis loop represents the heat dissipation in the system (see Fig. 1.1).

Within a linear approximation (small field), the magnetization can be expressed in terms of the complex susceptibility $\chi = \chi' - i\chi''$. For an AC field $H(t)$=Re$[H_0 e^{i\omega t}]$, the resulting magnetization is,

$$M(t) = H_0(\chi' \cos\omega t + \chi'' \sin\omega t), \tag{1.3}$$

where χ' and χ'' denote the in-phase and out-of-phase components of χ respectively*[13].

Within the linear approximation, the heating energy commonly calculated as the electromagnetic power lost per unit mass of the magnetic material, called specific loss power (SLP), can be expressed in terms of the imaginary component of the susceptibility by [13, 32],

$$\mathrm{SLP}(f, H_0) = \mu_0 \pi \chi''(f) H_0^2 f/\rho, \tag{1.4}$$

where ρ is the mass density of the magnetic material, f is the AC frequency and χ'' is given by,

$$\chi''(f) = \chi_0 \phi/(1+\phi^2), \tag{1.5}$$

where $\chi_0 = \mu_0 M_s^2 V/(k_B T)$, and $\phi = f\tau_R = \tau_R/\tau_M$, the ratio of the relaxation time

*By substituting $M(t)$ and $H(t)$ into Eq. 1.2, only the χ'' component survives, and

$$Q = \omega \mu_0 H_0^2 \chi'' \int_0^{2\pi/\omega} \sin^2(\omega t) dt.$$

For $f = \omega/2\pi$, the power dissipation per unit volume is,

$$P = fQ = \mu_0 \pi \chi'' f H_0^2.$$

τ_{R} and the measurement time, τ_{M} (the period of the AC field). The characteristic reversal time for immobilized particles with volume V, the Néel relaxation time, is given by [9],

$$\tau_{\mathrm{R}} = \tau_0 \exp \frac{KV}{k_{\mathrm{B}}T}, \quad \tau_0 \sim 10^{-9} - 10^{-10} \text{ s}, \tag{1.6}$$

where τ_0 is the period associated with the so-called attempt frequency f_0, or frequency of approaching the barrier; Brown [33] showed that f_0 is a function of parameters such as the magnetization damping constant α, K, M_{s}, T and V.

At low-frequencies (in the SPM regime with $\tau_{\mathrm{R}} < \tau_{\mathrm{M}}$), SLP is proportional to the frequency squared ($\simeq \mu_0 \chi_0 \pi H_0^2 f^2 \tau_{\mathrm{R}}/\rho$), whereas for high frequencies ($\tau_{\mathrm{R}} > \tau_{\mathrm{M}}$) SLP ($\simeq \mu_0 \chi_0 \pi H_0^2 \ /\rho\tau_{\mathrm{R}}$) is frequency independent. Thus, the linear theory predicts a frequency threshold beyond which heating does not increase. However, the linear theory also predicts a peak in SLP as a function of particle size, and thus predicts an optimal range of particle sizes for magnetic hyperthermia. Thus, the linear theory provides a starting point for understanding magnetic hyperthermia, particularly when minor hysteresis loops are involved, in terms of the dependence of heating on frequency and particle size.

In addition to the selective therapeutic heating with MNPs, radio frequency AC fields can result in Joule heating in both cancerous and healthy tissues due to induced eddy currents within those tissues. The later, of course, is undesirable. The absorbed power is proportional to the squares of field amplitude and frequency, and is given by [32],

$$P = \sigma \cdot G \cdot (H_0 \cdot f \cdot r)^2, \tag{1.7}$$

where σ is the electrical conductivity, G is a geometric coefficient, and r is the radius of the coil producing the field. Preclinical studies [34] reported the general thermal effects (due to eddy currents) are tolerable in human test subjects, as long as $H_0 f \leq C =$

5×10^{-9} A/(m.s). Therefore, the sweep rate of the AC field is limited to SR $= dH/dt = 4H_0 f \leq 20 \times 10^{-9}$ A/(m.s)= 0.25 Oe/ns. Moreover, to restrict the Brownian motion and rotation of NPs, using a frequency of at least 100 kHz is recommended [32]. Thus, a reasonable set of field parameters to use is $H_0 = 500$ Oe (0.05 T) and $f = 125$ kHz.

In addition to the field parameters, various studies explored the effects of particle aggregation, size, and size distribution on the SLP, and some of these results are discussed in section 1.7. Providing adequate MNP supply to the tumor for homogeneous heat generation is also a primary concern in practical applications, as insufficient temperature increase in parts of the tumor can trigger the risk of multiplication of surviving tumor cells [9]. Therefore, understanding the primary effectual parameters in magnetic nanoparticle heat production is necessary for developing optimized hyperthermia treatment.

1.4 Magnetic structure and interactions

This section presents a brief review of the crystal structure and magnetic interactions in magnetite NPs. In the next section we explain the required modifications in calculating the interactions convenient for the numerical approach in this study.

1.4.1 Crystal structure of Fe_3O_4

Magnetite, with formula unit Fe_3O_4, made of Fe^{3+} (ferric) and Fe^{2+} (ferrous) cations and O^{2-} anions, is categorized in the $Fd\bar{3}m$ space group and has an inverse spinel crystal structure [35, 36]. A spinel has a face-centred cubic structure with tetrahedral and octahedral bases. Fig. 1.2 shows an arrangement of two of the tetrahedral bases (containing A sites – green) and two of the octahedral bases (containing B sites –

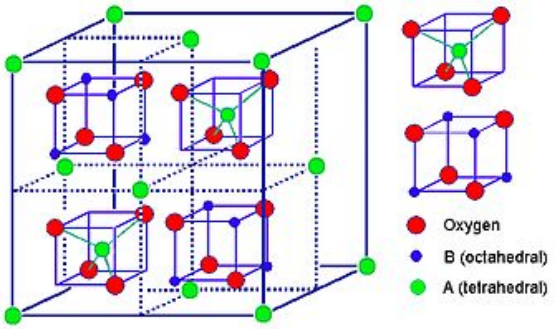

Figure 1.2: Crystal structure of magnetite as an inverse spinel $Fe^{3+}(Fe^{2+}Fe^{3+})O_4$ constructed from tetrahedral and octahedral bases. In addition to the oxygen ions in red balls, iron ions at octahedral and tetrahedral sites represented in blue and green balls, respectively. For simplicity four of the bases in a unit cell are shown. Figure reproduced from Ref. [37], under license CC BY-SA 4.0.

blue) in a spinel structure. If the A sites are occupied with valency two cations, and B sites with valency three cations, the structure is a normal spinel (in this case $Fe^{2+}(Fe^{3+})_2O_4$). But if, like magnetite, the A sites and half of the B sites are occupied with valence three cations and the other half of the B sites with valence two cations ($Fe^{3+}(Fe^{2+}Fe^{3+})O_4$), the structure is called inverse spinel.

The cubic unit cell of magnetite, with lattice parameter $a = 0.839$ nm, is composed of eight Fe_3O_4 formula units. Magnetite properties change with temperature. In the temperature range of 0 to $T_V = 120$ K, the Verwey transition temperature*, electrons are localized in a less symmetric crystal structure, resulting in a smaller conductivity. In the range between $T_V = 120$ K and $T_C = 858$ K (the Curie temperature), magnetite is a ferrite with an inverse spinel structure, in which electrons may hop between Fe^{2+} and Fe^{3+} ions, which is responsible for its large conductivity. Above the Curie temperature, magnetite is paramagnetic.

*The temperature at which the magnetite crystal structure changes from monoclinic to cubic inverse spinel is called the Verwey transition temperature, T_V.

1.4.2 Zeeman Energy

The energy of a magnetic moment $\boldsymbol{\mu}$ in an external magnetic field $\mathbf{B}$ is $-\boldsymbol{\mu}\cdot\mathbf{B}$. Parallel alignment of $\boldsymbol{\mu}$ with $\mathbf{B}$ is the arrangement with the lowest energy. At the same time, the field produces a torque on the magnetic moment of $\boldsymbol{\mu} \times \mathbf{B}$. As the magnetic moment is associated with angular momentum $\mathbf{L}$ through the gyromagnetic ratio γ via $\boldsymbol{\mu} = -\gamma\mathbf{L}$, and given the fact that the time rate of change of angular momentum is equal to the torque, the time evolution of a magnetic moment is governed by

$$\frac{d\boldsymbol{\mu}}{dt} = -\gamma\boldsymbol{\mu} \times \mathbf{B}, \tag{1.8}$$

with the result that $\boldsymbol{\mu}$ precesses around $\mathbf{B}$ [11]. The Landau-Lifshitz-Gilbert (LLG) equation is an extension of Eq. 1.8 to study the dynamics of $\boldsymbol{\mu}$ in the effective field due to magnetic interactions in addition to the external field in the presence of damping. Details on the LLG equation are found in the next chapter.

1.4.3 Exchange Interactions

The exchange interaction between atoms is a quantum mechanical effect due to the antisymmetric overlap of adjacent spin-dependent electron wave functions. In exploring the origin of the exchange interactions, consider a system such as a hydrogen-molecule consisting of two electrons with wave functions $\boldsymbol{\psi}_a$ and $\boldsymbol{\psi}_b$ in spatial coordinates $\mathbf{r}_1$ and $\mathbf{r}_2$. The wave function for the joint state is $\boldsymbol{\psi}_a(\mathbf{r}_1)\boldsymbol{\psi}_b(\mathbf{r}_2)$, which is not symmetric under exchange of two electrons $[\boldsymbol{\psi}_a(\mathbf{r}_1)\boldsymbol{\psi}_b(\mathbf{r}_2) \neq \boldsymbol{\psi}_b(\mathbf{r}_1)\boldsymbol{\psi}_a(\mathbf{r}_2)]$. To have well-behaved states under the particle exchange operations, the only allowed states are symmetrized or antisymmetrized product states [11]. The overall wave function for these electrons is antisymmetric, and by using the symmetric ($\boldsymbol{\chi}^{\text{Triplet}}$) and antisymmetric ($\boldsymbol{\chi}^{\text{Singlet}}$)

spin functions*[11], two combinations of spatial and spin contributions are possible that result in antisymmetric overall wavefunctions with respect to exchanging electrons,

$$\begin{aligned}\Psi_{\mathrm{S}} &= \frac{1}{\sqrt{2}}[\boldsymbol{\psi}_a(\mathbf{r}_1)\boldsymbol{\psi}_b(\mathbf{r}_2) + \boldsymbol{\psi}_a(\mathbf{r}_2)\boldsymbol{\psi}_b(\mathbf{r}_1)]\boldsymbol{\chi}^{\mathrm{Singlet}},\\ \Psi_{\mathrm{T}} &= \frac{1}{\sqrt{2}}[\boldsymbol{\psi}_a(\mathbf{r}_1)\boldsymbol{\psi}_b(\mathbf{r}_2) - \boldsymbol{\psi}_a(\mathbf{r}_2)\boldsymbol{\psi}_b(\mathbf{r}_1)]\boldsymbol{\chi}^{\mathrm{Triplet}}.\end{aligned} \tag{1.9}$$

The energies corresponding to the two possible states, using the Hamiltonian $\mathcal{H}$, are,

$$\begin{aligned}E_{\mathrm{S}} &= \int \Psi_{\mathrm{S}}^{*}\mathcal{H}\Psi_{\mathrm{S}}d\mathbf{r}_1 d\mathbf{r}_2,\\ E_{\mathrm{T}} &= \int \Psi_{\mathrm{T}}^{*}\mathcal{H}\Psi_{\mathrm{T}}d\mathbf{r}_1 d\mathbf{r}_2.\end{aligned} \tag{1.10}$$

Assuming normalized spin functions, the energy difference can be written as

$$E_{\mathrm{S}} - E_{\mathrm{T}} = 2\int \boldsymbol{\psi}_a^{*}(\mathbf{r}_1)\boldsymbol{\psi}_b^{*}(\mathbf{r}_2)\mathcal{H}\boldsymbol{\psi}_a(\mathbf{r}_2)\boldsymbol{\psi}_b(\mathbf{r}_1)d\mathbf{r}_1 d\mathbf{r}_2. \tag{1.11}$$

Using $\mathbf{S}_1{\cdot}\mathbf{S}_2$ values for singlet and triplet spin configurations, where $\mathbf{S}_1$ and $\mathbf{S}_2$ are spin functions of the two electrons, the Hamiltonian, based on Eq. 1.10, can effectively be rewritten as,

$$\mathcal{H} = \frac{1}{4}(E_{\mathrm{S}} + 3E_{\mathrm{T}}) - (E_{\mathrm{S}} - E_{\mathrm{T}})\mathbf{S}_1 \cdot \mathbf{S}_2. \tag{1.12}$$

That is, $\mathcal{H}$ as written above, will yield energy E_S when operating on the singlet state, and energy E_T when operating on a triplet state; the expectation value of the energy depends on whether the two-electron wavefunction is a singlet or triplet state, and this is captured by the effective Hamiltonian, which is written in terms of the dot product

*In coupling two spins $\mathbf{S}_1$ and $\mathbf{S}_2$, eigenstates of $\mathbf{S}_1{\cdot}\mathbf{S}_2$ can have symmetric (Triplet, $\mathbf{S}_1{\cdot}\mathbf{S}_2$ =1/4) or antisymmetric (Singlet, $\mathbf{S}_1{\cdot}\mathbf{S}_2 = -3/4$) configurations. The singlet eigenstate is $\boldsymbol{\chi}^{\mathrm{Singlet}} = (|\uparrow\downarrow\rangle - |\downarrow\uparrow\rangle)/\sqrt{2}$ with $\mathrm{m_s} = 0$, $\mathrm{S_{tot}}$=0 and the triplet eigenstate ($\mathrm{S_{tot}} = 1$) will be one of the configurations $\boldsymbol{\chi}^{\mathrm{Triplet}} = |\uparrow\uparrow\rangle$ with $\mathrm{m_s} = 1$, or $|\downarrow\downarrow\rangle$ with $\mathrm{m_s} = -1$ or $(|\uparrow\downarrow\rangle + |\downarrow\uparrow\rangle)/\sqrt{2}$ with $\mathrm{m_s} = 0$.

operator for the two spins. By neglecting the constant term in the Hamiltonian, and rewriting the spin-dependent term using the defined exchange constant J (or exchange integral) we have

$$\mathcal{H} = -2J\mathbf{S}_1 \cdot \mathbf{S}_2, \quad J = \frac{E_\mathrm{S} - E_\mathrm{T}}{2} \tag{1.13}$$

where $J > 0$ is equivalent to $E_\mathrm{S} > E_\mathrm{T}$, i.e. the triplet state with $S = 1$ (ferromagnetism) is favored, whereas $J < 0$ is equivalent to $E_\mathrm{S} < E_\mathrm{T}$, i.e. the singlet state with $S = 0$ (antiferromagnetism) is favored. Therefore, for a system of atoms having exchange interactions with their nearest neighbors, the Heisenberg model Hamiltonian is defined as,

$$\mathcal{H} = -\sum_{i,j} J_{ij}\mathbf{S}_i \cdot \mathbf{S}_j, \tag{1.14}$$

where J_{ij} is often taken equal to a constant J for all nearest neighbors and zero otherwise and the factor of 2 is omitted as the summation includes each pair of neighbors twice[11].

Experimental methods, like inelastic neutron scattering, are used to characterize spin wave excitations for ferrites at long wavelength*. At small k, it is normal to express the spin wave dispersion relation as [38],

$$\hbar\omega = \Delta_g + Dk^2 + ... \tag{1.15}$$

where Δ_g denotes the effective energy gap, which arises due to some forms of magnetic anisotropy which is often negligible, and D is the exchange stiffness constant. Having Eq. 1.14 in mind, for the long wavelength approximation on the acoustic branch, the

*As phonons are representative of quantized lattice vibrational excitations, quantized spin waves, also called magnons, represent the quantized spin-lattice disruptions or spin waves. The dispersion relation is a relation between energy, $\hbar\omega$, and momentum, $\hbar k$.

energy ϵ_k^a can be expressed as,

$$\epsilon_k^a \simeq Dk^2 = \frac{\sum_{\mathrm{i,j}} |\mathbf{S}_\mathrm{i} \cdot \mathbf{S}_\mathrm{j} J_\mathrm{ij} (\mathbf{k} \cdot \mathbf{r}_\mathrm{ij})^2|}{\sum_\mathrm{i} |\mathbf{S}_\mathrm{i}|}. \tag{1.16}$$

To calculate the exchange energy of magnetite with a face-centered cubic (FCC) crystal structure having octahedral (B sites) and tetrahedral (A sites) bases (see section 1.4.1), two different models have been used. One is called the two sub-lattice approach and considers all the iron ions on the octahedral basis with $S_\mathrm{B} = 9/4$ (Fe^{2+} and Fe^{3+}) and iron ions on the tetrahedral basis with $S_\mathrm{A} = 5/2$ (Fe^{3+}), and defines exchange constants J_AA, J_BB, and J_AB for mutual spin interactions[35, 36, 39, 40]. The other approach is called the three sub-lattice model and considers two types for octahedral site ions, B_1 for Fe^{3+} ions with $S_\mathrm{B1} = 5/2$ and B_2 for Fe^{2+} ions with $S_\mathrm{B2} = 2$, in addition to the A type. Srivastava et al. [38] compared two models and showed, by choosing the proper exchange constants ($J_\mathrm{AA} = 0$, $J_\mathrm{AB} = -28$ K, $J_\mathrm{BB} = +3$ K), both interpretations are identical and the exchange stiffness constant is,

$$D = \frac{2J_\mathrm{AA}S_\mathrm{A}^2 + 4J_\mathrm{BB}S_\mathrm{B}^2 - 11J_\mathrm{AB}S_\mathrm{A}S_\mathrm{B}}{8|S_\mathrm{A} - 2S_\mathrm{B}|}a^2, \tag{1.17}$$

where a is the length of the magnetite unit cell. The theoretically calculated value of $D = 102 \times 10^{-41}$ Jm^2 by Srivastava et al. [38] is comparable to the experimentally reported result from neutron scattering at room temperature $D = 142 \times 10^{-41} \mathrm{Jm}^2$ [41]. How D is related to the exchange constant A used in the micromagentic simulations at the core of this thesis is described below in section 1.5.

1.4.4 Anisotropy

Crystal structure, shape and surface effects of magnetic nanoparticles as well as the surrounding material can result in a preferred direction for their magnetic moments, called anisotropy. The anisotropy energy density K determines the energy barrier between energy minima. The field strength associated with this energy barrier is H_k (as before $H_k = 2K/\mu_0 M_\mathrm{s}$).

1.4.4.1 Magneto-crystalline anisotropy

The crystal field is defined as the electric field derived from neighboring atoms in the crystal [11]. The symmetry of the local environment controls the size and nature of crystal field effects. The competition between the crystal field in electronic orbital preference and Coulomb energy cost in pairing electrons determines the occupied electronic orbitals, and hence the total spin*. Perturbations like temperature, pressure or even light irradiation can disturb this energy competition and cause a spin transition between low-spin and high-spin configurations [11].

The preference of a spin to lie along a particular crystalline direction ($\hat{\mathbf{u}}$) because of the crystal field is quantified by $\mathcal{H}_\mathrm{anis}$ in the Hamiltonian, which for a uniaxial crystal depends on the angle the spin makes with the anisotropy axis $\hat{\mathbf{u}}$, namely $\hat{\mathbf{z}}$, and can be written as,

$$\mathcal{H}_\mathrm{anis} = -K_\mathrm{u}(\mathbf{S}\cdot\hat{\mathbf{u}})^2 = -K_\mathrm{u}S_z^2, \tag{1.18}$$

where K_u is the uniaxial magnetocrystalline anisotropy constant or energy density.

*A crystal field often promotes pairing electrons to fill the lower orbitals, and the resulting opposite electronic spins lower the atoms' total spin, whereas under the influence of Coulomb repulsion filling different orbitals is preferred, which results in higher total spin.

When $K_u > 0$ (easy axis), the system is more stable if spins align to $\hat{\mathbf{u}}$, and if $K_u < 0$ (hard axis), the energy is minimized when spins lie in a plane perpendicular to $\hat{\mathbf{u}}$. Also, for a cubic crystal with three equally preferred axes, i.e. $\hat{\mathbf{x}}$, $\hat{\mathbf{y}}$, $\hat{\mathbf{z}}$, the lowest order anisotropy term occurs at fourth order, given by,

$$\mathcal{H}_{\text{anis}} = -K_c(S_x^4 + S_y^4 + S_z^4) \tag{1.19}$$

where K_c represents the cubic anisotropy constant. Similarly, $K_c > 0$ causes spins to align along [100] and equivalent directions and for $K_c < 0$ the preferred anisotropy axes are along [111]. Experimental studies have reported cubic crystalline anisotropy for bulk magnetite with $K_c < 0$ but there is no uniaxial anisotropy due to the cubic crystal symmetry.

Theoretically, a uniform magnetization is achievable, perhaps surprisingly, only for single-domain ellipsoidal magnetic nanoparticles [26, 42]. Slight nonuniformity in a nanoparticle's magnetization can considerably influence the particle's magnetic properties like susceptibility, anisotropy, and hysteresis features. Surface and shape effects can play crucial roles in the nanoparticle's effective anisotropy [43, 44].

1.4.4.2 Surface anisotropy

Surface anisotropy originates from broken symmetry at the surface and can impart magnetization orientation perpendicular to the surface. Surface anisotropy can be orders of magnitude greater than bulk magnetocrystalline anisotropy, for example, order of $1 - 10$ mJ/m^2 versus equivalent $0.01 - 1$ mJ/m^2 in cubic ferromagnets [45]. Broken symmetry of boundaries, surface-core strains, and magnetostriction* can lead

*Magnetostriction is defined as a property of ferromagnetic materials that causes them to change their shape or dimension in response to a magnetic field.

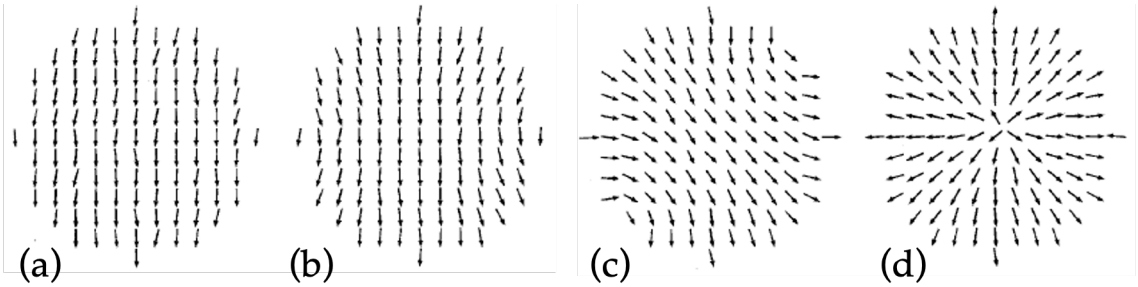

Figure 1.3: The central plane for a nanosphere with diameter $12a$, where a is the interatomic spacing, when the surface to the bulk material anisotropy energy density, K_S/K_V, equals a) 1, b) 10, c) 40, d) 60. Reprinted from Ref. [45], with the permission of AIP Publishing.

to large surface anisotropy. It is presumed that the surface influence will be most significant in ferromagnet NPs with low-Curie temperature when the surface anisotropy is comparable to the exchange. Also, for a higher surface-to-volume ratio, the surface anisotropy is more effective [45, 46]. Among studies evaluating the surface anisotropy, Labaye [45] used atomic Monte Carlo simulations to explore the surface anisotropy effect on a particle's magnetization alignment for different relative surface and bulk anisotropy strengths.

Fig. 1.3 shows the Labaye et al. simulation results for particles with size $12a$ where a is the interatomic spacing. The authors concluded that the surface anisotropy can play an important role in the alignment of spins inside the NP, transforming a uniform magnetization to a throttled spin structure, in which the core spins align parallel to each other and the outer most spins lie normal to the surface (Fig. 1.3c), and for sufficiently small particles (or sufficiently large surface anisotropy) into a radial spin structure (Fig. 1.3d).

1.4.4.3 Shape anisotropy

The magnetization discontinuity at the surface of a finite-sized ferromagnet leads to effects that can be modelled by a surface layer of magnetic charges or monopoles. This can be understood from the divergence equation $\nabla \cdot \mathbf{M} = -\nabla \cdot \mathbf{H}$, which follows from $\nabla \cdot \mathbf{B} = 0$ and $\mathbf{B} = \mu_0(\mathbf{M} + \mathbf{H})$; e.g., if $\mathbf{M} = M_x \hat{x}$ is a step function along x ($\mathbf{M}$ goes to zero abruptly at the boundary of the magnet), then $\nabla \cdot \mathbf{M}$ is a Dirac delta function, and hence $\mathbf{H}$ can be thought of as originating from a sheet of magnetic charge at the boundary. The field arising from these surface monopoles is called the demagnetization field and is labelled $\mathbf{H}_d$. It is a complicated function of the position within magnets of arbitrary shape. However, for a uniformly magnetized ellipsoid, it can be written as $\mathbf{H}_d = -\mathbf{N}\mathbf{M}$, where $\mathbf{N}$ is the demagnetizing tensor that depends on the axes lengths of the ellipsoid. The shape of the object implies preferred directions for the magnetization. In the case of a spheroid, the demagnetization energy $E = \mu_0 \mathbf{M} \cdot \mathbf{N} \cdot \mathbf{M}/2$ can be written in the form of a uniaxial anisotropy with energy density $K_{\mathrm{sh}} \propto \mu_0 M_{\mathrm{s}}^2/2$ [11, 26]. For cases where this anisotropy is strong in cubic crystals, the particle's effective anisotropy can be considered uniaxial [47]. The dimensionless ratio $\mu_0 M_{\mathrm{s}}^2/|K_{\mathrm{c}}|$ estimates the shape anisotropy contribution to the particle's total energy relative to its cubic magnetocrystalline anisotropy. For magnetite spheroids with a ratio as small as 1.2 between semi-axes lengths, effects of cubic anisotropy can be ignored as the uniaxial shape anisotropy is dominant [48].

The Brown-Morrish theorem [48, 49] suggests equivalence of an arbitrarily-shaped uniformly-magnetized particle with an ellipsoid of the same volume in terms of the magnetostatic energy. The shape anisotropy constant corresponding to a spheroidal

particle with semi-axes a and b is given by,

$$K_{\rm sh} = \frac{\mu_0 M_{\rm s}^2 (N_\perp - N_{||})}{2}, \tag{1.20}$$

where $N_\perp$ and $N_{||}$ are demagnetizing factors perpendicular and along the rotational symmetry axis of the spheroid. $K_{\rm sh} > 0$ (long thin rods) implies a uniaxial easy axis and $K_{\rm sh} <0$ (disk shape) implies a uniaxial hard axis with spins preferring to lie in a plane perpendicular to the rotational symmetry axis. In appendix A we derive the shape anisotropy for a rectangular prism by considering the demagnetization tensor and compare it with the results from numerical simulation of magnetostatic interactions.

1.4.5 Dipole Interactions

Unlike quantum-based exchange interactions, dipole interactions are rooted in classical magnetism. The magnetic energy between two magnetic dipoles $\boldsymbol{\mu}_1$ and $\boldsymbol{\mu}_2$ separated by $\mathbf{r}$ is given by[11],

$$E = \frac{\mu_0}{4\pi r^3}\left(\boldsymbol{\mu}_1 \cdot \boldsymbol{\mu}_2 - \frac{3}{r^2}(\boldsymbol{\mu}_1 \cdot \mathbf{r})(\boldsymbol{\mu}_2 \cdot \mathbf{r})\right). \tag{1.21}$$

In addition to the magnitude of the moments and the distance between them, the magnetic energy depends on their directions relative to each other (first term), just as in Heisenberg exchange, as well as their directions relative to the line joining them (second term). In crystals, this axis is related to the lattice vectors.

Compared to exchange and magnetic anisotropy, the dipole energy is typically orders of magnitude weaker but is long-ranged and can have profound effects on the state of magnetization, and hysteresis loops, for ferromagnetic and ferrimagnetic

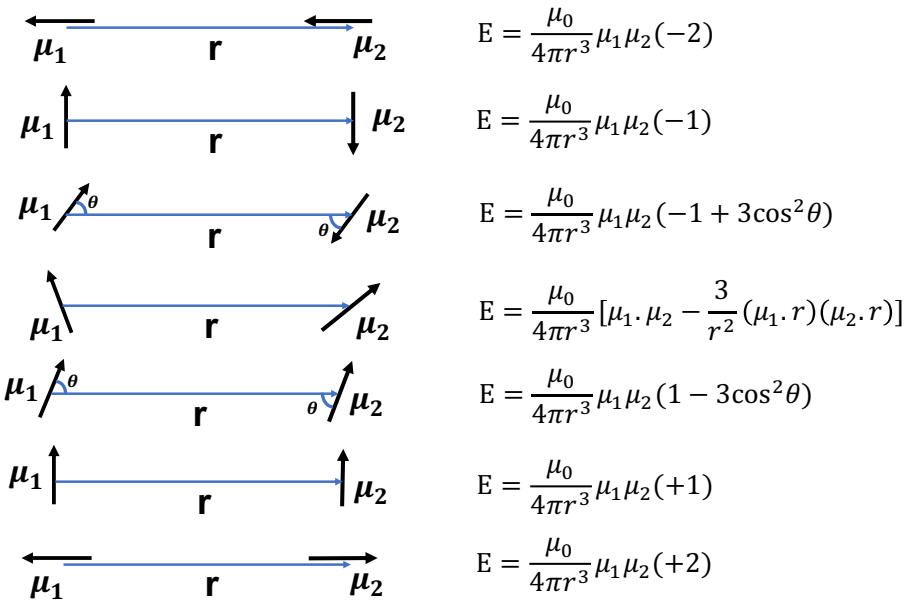

Figure 1.4: Dipole interaction from the lowest energy (most favorable at the top) to the highest energy (on the bottom).

materials. Owing to cancellation effects, dipole interactions are much less important in the case of antiferromagnets. Various alignments of a pair of magnetic dipoles from the least to the highest dipole energy are shown in Fig. 1.4.

In the first case of Fig. 1.4, dipole moments are aligned with **r** in a chain formation with the same polarity. This is the most stable orientation. The tendency to form chains affects NP clustering and heating efficiency, as discussed further in the subsequent chapters. In the case where the moments are perpendicular to **r**, antiparallel orientation is favourable. Appropriate coating of magnetic particles is usually applied to weaken their mutual dipole effects by keeping them further apart.

1.5 Micromagnetics

The atomic-level theory is the most accurate approach for describing ferromagnets, but its application is restricted to very small systems owing to large computational complexity. Micromagnetics is a way of modelling ferromagnets on sub-micron scales that replaces the atomic details in, say, a unit cell with a uniformly magnetized cell of the same volume. In this approximation, the length scale is large enough to treat the discrete atomic structure as continuous and is small enough to resolve inter-domain features. Micromagnetics can deal with the static equilibrium properties by minimizing the magnetic energy of the system and its dynamic behavior by solving the LLG equation that describes the time-dependent dynamics of the system (see section 2.2).

Dipoles within magnetic materials originate from atomic-level magnetic moments. Micromagnetics introduces magnetic units, or cells, where sub-cell atomic moments are correlated through exchange interactions, and the cell represents the collective behavior of the atomic moments with a single magnetic moment $\boldsymbol{\mu}_i$. Based on the exchange interactions, a correlation length called the exchange length (l_{ex}) is defined for magnetic moments. It is reasonable to expect homogeneous behavior of atomic spins within a cell so long as the cell is no larger than l_{ex}. At low T, l_{ex} arises from a competition between exchange and magnetostatic interactions and is approximated by [50],

$$l_{\text{ex}} = \sqrt{\frac{2A}{\mu_0 M_{\text{s}}^2}}, \tag{1.22}$$

where A is the exchange energy constant defined below (in units of J/m).

In describing the magnetic behavior of a material, the goal is to find the magnetization's* spatial distribution, both in equilibrium and as a function of time. In micromagnetics, at temperatures lower than the Curie temperature, the magnetization of all cells is considered to have fixed magnitude equal to M_{s}, and the spatial distribution of magnetization is determined by the variable magnetization direction $\mathbf{m}_i = \mathbf{M}_i/M_{\mathrm{s}}$ of every cell.

Some modifications in the exchange and dipole interaction calculations are needed in the transition from an atomic moment description to a magnetic cell representation. Rewriting Eq. 1.14 as a sum over pairs $\langle i,j\rangle$ of neighbouring magnetic cells instead of neighbouring spins gives (with no double counting in the sum),

$$E = -\sum_{\langle i,j\rangle} J_{\mathrm{eff}}\mathbf{m}_i \cdot \mathbf{m}_j, \quad J_{\mathrm{eff}} = aA, \tag{1.23}$$

where the exchange constant A is defined based on the cell dimension a and the exchange energy between two cells J_{eff}. Relating A to the spin wave stiffness D, we have [51],

$$A = \frac{DM_{\mathrm{s}}}{2\mu_B g} \tag{1.24}$$

where μ_B is the Bohr magneton and g is the electron g-factor which is $\simeq 2$. Using the value of D from Eq. 1.17 of 102×10^{-41} Jm^2 and $M_{\mathrm{s}} = 480$ kA/m gives a theoretical estimate for A of 1.32×10^{-11} J/m.

The dipole interaction is a suitable description for atomic-scale point dipoles but is not accurate for finite-size micromagnetic cells. Therefore, a more detailed description of magnetostatic interactions is needed. Micromagnetic cells are magnetized volumes

*Magnetization is the system's magnetic moment per unit of volume $\mathbf{M} = \sum_i \boldsymbol{\mu}_i/V_{\mathrm{Total}} = \sum_i \mathbf{M}_i V_i/V_{\mathrm{Total}}$, where $\mathbf{M}_i$ is the magnetization of micromagnetic cell i and V_i is its volume. $V_{\mathrm{Total}} = \sum_i V_i$.

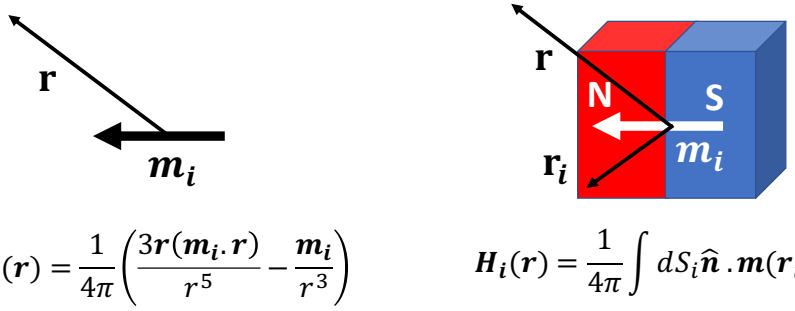

Figure 1.5: The magnetic field produced by a magnetic point dipole and a bar magnet at distance **r**.

that behave like bar magnets under the magnetic field created by other bar magnets. Comparing the magnetic field created by a point dipole and a bar magnet at a distance **r** shows that the bar magnet's shape and size should be taken into account, as shown in Fig. 1.5.

Following the concepts introduced in section 1.4.4.3, the magnetostatic field ($\mathbf{H}_d$) generated by a magnetized volume v' in the observation volume v can be calculated using a demagnetizing tensor $\mathbf{N}(\mathbf{r} - \mathbf{r}')$ that correlates the spatial coordinates within the two volumes [52]. When the observation volume coincides with the source volume, the field generated by the magnetization within the magnet tends to reduce the total magnetic field inside the medium and is called the self-demagnetizing field.

In general, we can calculate the field at a point $\mathbf{r}$ due to all points $\mathbf{r}'$ within a magnetized cell through,

$$\begin{aligned} \mathbf{H}_d(\mathbf{r}) &= \int \mathbf{N}(\mathbf{r} - \mathbf{r}')\mathbf{M}(\mathbf{r}')d\mathbf{r}', \quad \text{with} \\ \mathbf{N}(\mathbf{r} - \mathbf{r}') &= -\frac{1}{4\pi}\nabla\nabla'\frac{1}{|\mathbf{r} - \mathbf{r}'|}. \end{aligned} \tag{1.25}$$

Consequently, the magnetostatic energy between the two cells is given by,

$$\begin{aligned} E(\mathbf{r}) &= -\frac{\mu_0}{2}\int \mathbf{M}\cdot\mathbf{H}_d(\mathbf{r})d\mathbf{r} \\ &= -\frac{\mu_0}{2}\int\int \mathbf{M}(\mathbf{r})\mathbf{N}(\mathbf{r}-\mathbf{r}')\mathbf{M}(\mathbf{r}')d\mathbf{r}d\mathbf{r}'. \end{aligned} \tag{1.26}$$

Magnetostatic interactions are weaker than exchange interactions. However, they are long-range interactions, and hence become important on larger length scales. For example, magnetostatics are important for describing domain formation and also for calculating hysteresis loops for aggregates of NPs. Magnetostatics are also crucial for the dynamics of NP aggregation, but this is beyond the scope of purely micromagnetic simulations.

1.6 Magnetic properties of Fe_3O_4

The reported value for the bulk saturation magnetization of magnetite is approximately $M_s = 480$ kA/m, and its magnetocrystalline anisotropy is cubic with $K_c = -10^4$ J/m^3 [44, 53]. As described above in section 1.4.4.3, $K_{sh} \propto \mu_0 M_s^2$, and the energy contribution of shape anisotropy relative to that of magnetocrystalline anisotropy is proportional to $\mu_0 M_s^2/|K_c|$, which for magnetite is approximately 29. Such a large ratio implies an important role for shape anisotropy even for mildly aspherical NPs.

Among experimental studies exploring the crystalline anisotropy of magnetite, Řezníček et al. [54] investigated properties of defect-containing cubic magnetite. They did not report a significant change in magnetocrystalline anisotropy and spin reorientation temperature due to the defects. They attributed this to the lack of localized and strongly anisotropic ions in magnetite. In another experimental study, Shi et al. [55] explored the heating efficiency as a function of applied field angle on fixed

magnetite nanoparticles. Their results revealed an easy axis presence in magnetite NPs, i.e., for nonspherical magnetite NPs, shape anisotropy dominates over its bulk cubic anisotropy.

To characterize the exchange constant of magnetite, Moskowitz et al. [51] reported eleven experimentally-determined values from the literature of the exchange integral J_{AB}, assuming $J_{\mathrm{AA}} = J_{\mathrm{BB}} = 0$. They reported the average value of $A = 1.29 \times 10^{-11}$ J/m at room temperature with an estimated 35% uncertainty due to poorly characterized finite values for J_{AA} and J_{BB}.

1.7 Hyperthermia

1.7.1 Experimental studies

Various experimental studies have been reported using magnetic iron oxide nanoparticles (MIONs) in hyperthermia. Our research is inspired by a study reported by Dennis et al. [10] that used magnetite nanoparticles for treating cancerous breast tissue in mice. The MNPs used in these experiments consisted of a magnetite core approximately 50 nm in diameter coated with an approximately 26 nm thick dextran shell that improved biocompatibility and helped prevent NP aggregation.

Their analysis of results from transmission electron microscopy (TEM) and X-ray diffraction supports an assumption that NP cores are composed of parallelepiped-shaped crystals of magnetite with dimensions of 6.5 nm×19 nm×49 nm and with a crystallographic axis along the length of the parallelepiped. The saturation magnetization of the NPs was calculated from hysteresis loops to be $M_{\mathrm{s}} = 211.56 \pm 0.15$ kA/m, which is half of the value for bulk magnetite, attributing some of the reduction to the

Table 1.1: Experimental parameters used for different groups of mice in the study by Dennis et al. [10].

AMF amplitude	AMF application time	Total dose J/g tumor	Mean max tumor temperature(°C)
31.8 kA/m=400 Oe	900 s=15 min	635	37
43.8 kA/m=550 Oe	900 s=15 min	800	47
55.7 kA/m=700 Oe	600 s=10 min	969	52
43.8 kA/m=550 Oe	1200 s=20 min	N/A	39
0	0	N/A	N/A

diamagnetic properties of the dextran shell. In exploring the presence of interparticle interactions, magnetometry along with neutron scattering results proved the presence of magnetostatic interactions, which may positively or negatively affect how well the NPs heat up in response to the AC field.

In the Dennis et al. study, twelve female mice were divided into three groups, all bearing (MTG-B murine) human breast tumors with volume 180 ± 40 mm^3. All the cases received an equal dose of MNPs under AMF with different amplitude and field exposure duration at a fixed frequency of 150 kHz. Two more groups, one just receiving field without any MNPs and another with no treatment, were taken as control groups. Different parameters used in the study are shown in Table 1.1.

A visual summary of the treatment results representing the tumor volume as a function of time is shown in Fig. 1.6. As shown in both panels, for the third case listed in Tab. 1.1, which has the highest field amplitude, three out of four mice display a complete response to the treatment, i.e., no tumor regrowth was observed for the duration of the 60-day study.

In another study by Shi et al. [55] the magnetic properties of MIONs were explored by looking into their SLP dependence on the field amplitude and frequency as well

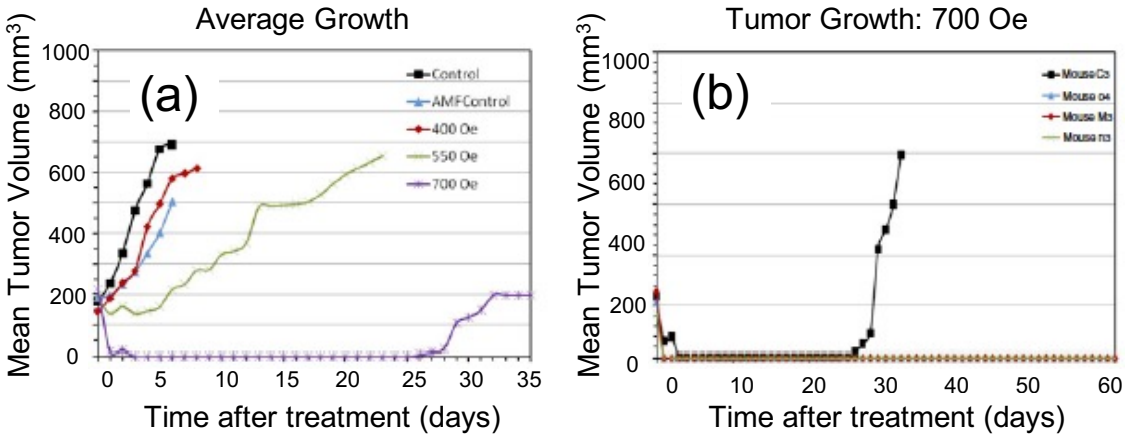

Figure 1.6: Therapeutic heating results in a pilot study (a) average growth curves for different groups in the study (b) growth curve for the tumor in each animal in the high field study case. (Figure taken from Ref. [10], © IOP Publishing. Reproduced with permission. All rights reserved.)

as applied field angle on oriented nanoparticles. In addition to $20-30$ nm magnetite NPs and 4 nm maghemite NPs, they used commercially available MRI contrast agent Resovist [56, 57], consisting of $5-10$ nm maghemite cores with a carboxydextran coating. To obtain oriented samples, MNPs were placed in a solvent under a DC field of 575 kA/m ($\simeq$ 7225 Oe) and then the solution was solidified. The frequency range was $1-100$ kHz and field amplitudes of 4 and 16 kA/m ($\simeq$ 50 and 200 Oe) were used. The SLP was measured when the AMF was applied: 1) parallel to the easy axes of oriented samples, 2) perpendicular to the easy axis (which they also refer to as being along the hard axis) as well as to randomly oriented particles in 3) solidified and 4) liquid solvents. Fig. 1.7 shows that for $H = 4$ kA/m, Resovist was the most effective mediator of heat generation compared to γ-Fe_2O_3 and Fe_3O_4. However, when the field was high enough to induce magnetization reversal in Fe_3O_4, it had the highest efficiency. The SLP difference for hard and easy axes of Fe_3O_4 indicates an effective uniaxial anisotropy in spite of its cubic crystalline anisotropy (see section 1.4.4.1).

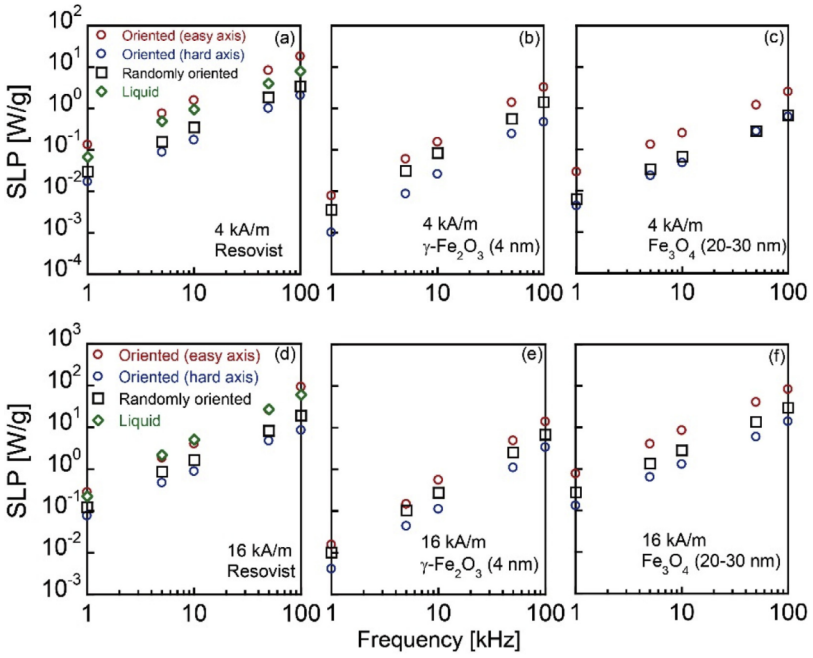

Figure 1.7: SLP changes with frequency for two field amplitudes, 4 (top row) and 16 kA/m (bottom row), for Resovist, 4 nm γ-Fe_2O_3 and $20 - 30$ nm Fe_3O_4 NPs (Reprinted from Ref. [55] with permission from Elsevier).

The authors also refer to the possibility of clinical SLP enhancement by orienting the particles by applying an orienting DC field along with an AMF.

Choosing the suitable magnetic iron oxide for hyperthermia is restricted by different factors such as good magnetic parameters, stability under oxidizing conditions and limited toxicity. The medical use of magnetite and maghemite have been approved by the US Food and Drug Administration and European Medicines Agency. However, there is current interest in other magnetic composites formed by substituting other magnetic ions in the general spinel ferrite formula MFe_2O_4, where M = Zn^{2+}, Mn^{2+}, Co^{2+}, Ni^{2+}, or Mg^{2+}, etc. The toxicological concerns related to the leakage of toxic ions put more restrictions on the use of high-anisotropy composites like $CoFe_2O_4$ [22].

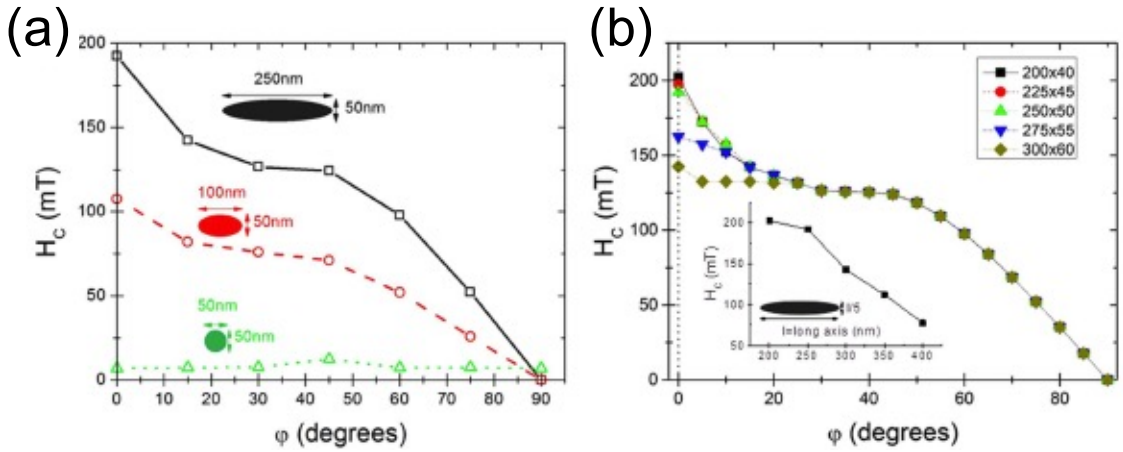

Figure 1.8: Dependence of the coercive field H_c on the angle between the field and the long axis of the spheroid for (a) different aspect ratios (b) different size nanoparticles with 5:1 aspect ratios. (Fig. from Ref. [16], open access article under the terms of Creative Commons CC BY license.)

1.7.2 Simulations

In addition to experiments, a number of simulation studies investigated the effective parameters used to model MNH that are relevant to the work presented in this thesis. Simeonidis et al. [16] performed a micromagnetic simulation study exploring the effect of shape anisotropy on the heating efficiency of magnetite NPs. They examined the coercive field (H_c) changes as a function of field orientation (φ) with spheroidal NPs for different aspect ratios (1, 2, 5) as shown in Fig. 1.8a. Hysteresis loops for spheroids with higher aspect ratio have bigger H_c and consequently a bigger MH loop area, especially when the field is parallel to their long axis. This is attributed to the induced uniaxial shape anisotropy of spheroids compared to spherical NPs, which get similar values of H_c at $\varphi = 0, 90°$ due to having only cubic anisotropy.

They also looked into how H_c changes with φ for spheroids of different sizes but with the same aspect ratio (5:1). As shown in Fig. 1.8b, they reported the same

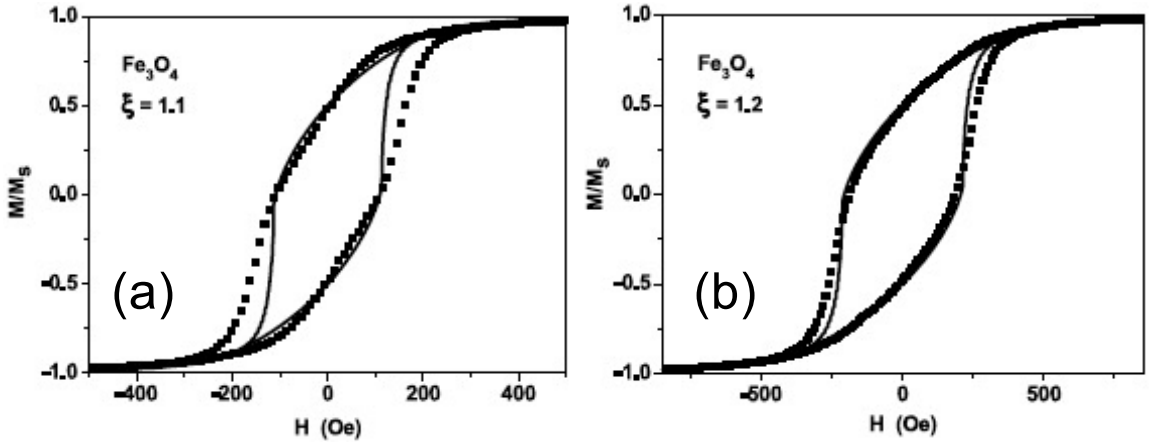

Figure 1.9: Hysteresis loops of an assembly of magnetite nanoparticles with different aspect ratios in comparison with the Stoner-Wohlfarth model. The results show that for ξ as small as 1.1, shape anisotropy dominates cubic anisotropy in the magnetic response. (Reprinted by permission from Springer Nature, from Ref. [48]).

H_c for $\varphi > 25°$ in all particles and for $\varphi < 25°$, a relatively smaller value of H_c for particles with dimensions larger than 250 nm$\times$50 nm. This decrease was attributed to a transition from coherent to incoherent reversal of magnetic moments for bigger ellipsoidal NPs.

In another study, Usov et al.[48] investigated the importance of shape anisotropy of nanoparticles compared to their cubic magnetocrystalline anisotropy. In that study, spheroidal particles with aspect ratio $\xi = b/a$ were assumed equivalent to arbitrarily-shaped NPs using the Brown-Morrish theorem [49]. They compared the hysteresis loop for a dilute, randomly oriented assembly of magnetite NPs equivalent to spheroids with aspect ratios $\xi = 1.1$ and 1.2 with a system of noninteracting spherical NPs having purely uniaxial anisotropy (the Stoner-Wohlfarth model). As shown in Fig. 1.9 the uniaxial shape anisotropy dominates over cubic magnetocrystalline anisotropy already for relatively small aspect ratios of $1.1 - 1.2$.

There are also studies quantifying the effect of MION size, field frequency and

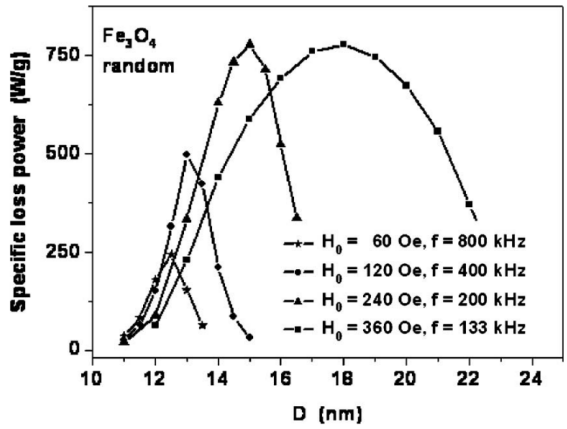

Figure 1.10: SLP of randomly oriented magnetite nanoparticles with aspect ratio b/a=1.5 as a function of transverse particle diameter for different field parameters. (Reprinted from Ref. [47], with the permission of AIP Publishing.)

amplitude, within ranges of biological safety, on SLP efficiency. With this objective, Usov [47] compared the SLP of magnetite nanoparticles in the size range of $11-22$ nm with different field properties. Randomly oriented elongated nanoparticles with aspect ratio 1.5 were considered and in all cases $fH_0 = 0.048$ Oe/ns. As shown in Fig. 1.10 the SLP reached ≈ 750 W/g for $H_0 \geq 240$ Oe. Unlike the linear regime, where the SLP is proportional to the particle size, here, the SLP peak becomes wider for higher field amplitudes, which implies the possibility of using particles within a relatively broad range of sizes for hyperthermia. It is also noteworthy that the author found no generally best AMF amplitude or frequency for all the magnetite nanoparticles studied. Instead, the optimal H_0 and f should be tailored based on the particle size and biological limitations.

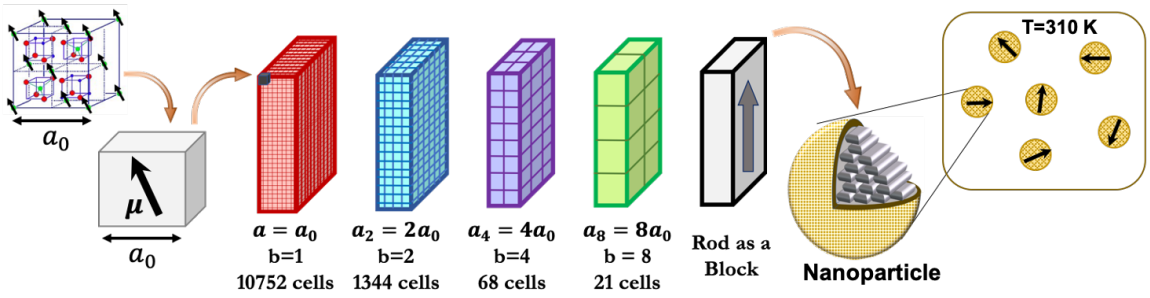

Figure 1.11: Simulation model of magnetite nanoparticles made of nanorods. Nanorods comprise 8×24×56 cells, each of volume of 0.839 nm^3.

1.8 Model of study

This thesis aims to understand, through simulation, factors that affect NP heating efficiency, and thus to help inform preclinical studies aiming to find more effective magnetic hyperthermia treatments. The idea of simulating spherical magnetite NPs composed of nanorods is taken from the experimental study by Dennis et al. [10]. We use micromagnetic modelling (not atomic scale) so that systems of a relevant size can be studied within a reasonable time frame. In this method, instead of simulating individual atomic spins, each unit cell is represented by a single magnetization. In this case, a rod is modelled using 10752 magnetite unit cells and simulations fulfilling biophysical restrictions (SR $\leq$ 0.25 Oe/ns) take several months.

To speed up computations, we seek to simulate a rod with bigger but fewer cells and still get the same physical properties. An approximate sketch of nanorods made of bigger cell is shown in Fig. 1.11, where $a_b = ba_0$ represents the proposed simulation cell sizes for $b > 1$ with the original micromagnetic unit cell length $a_0 = 0.839$ nm. The number of cells needed for simulating a nanorod is written beneath each case. For the "block" case, where a single non-cubic cell represents an entire nanorod, $b = 22$, a case we discuss below in the Chapter 3.

With a focus on the hysteresis loop, since the loop area represents the heat released into the system, the challenge is to scale the cells' interactions in order to get magnetization-field (MH) hysteresis loops that are approximately invariant with increasing cell size. A few schemes have been suggested for scaling magnetic interactions [58, 59] or even the damping factor [60] to account for the change of simulation cell size at finite temperature. After considering different methods, we modify, apply and validate a renormalization group (RG) approach due to Grinstein and Koch [61] to calculate hysteresis loops, obtaining approximate loop invariance with cell size. Using this scaling approach decreases the simulation run time and paves the path for simulating NPs made of nanorods, and finally assemblies of NPs.

1.9 Outline

The rest of this document is organized as follows. Chapter 2 reviews the mathematical basis of the problem – magnetization dynamics and coarse-graining – and the numerical method behind the simulations used in this study. It includes the basic concepts of the renormalization group approach for scaling the magnetic parameters as the backbone of this micromagnetic study. The third chapter contains our first publication, a letter reporting on our success in solving, applying, modifying and validating the approach of Grinstein and Koch RG within simulations of nanorods using OOMMF software. We justify our modification with the fact that it provides a more accurate description of the magnetization dependence on temperature for the Heisenberg model. As a result of this coarse-graining, simulation time decreases by a factor of up to 8^3. Moreover, we suggest scaling the damping constant α with the SR of changing field, that allows speeding up the calculation by up to 1000 times.

Our second paper appears as the fourth chapter, describing an extension and application of the above-said scaling technique to include magnetostatic interactions that were ignored in the initial model. We employ this coarse-graining approach for simulating multiple nanorods as NPs with different internal structures. We introduce a macrospin (MS) model, in which a nanorod or complex nanoparticle is represented by a single magnetization. The MS's effective anisotropy and saturation magnetization depend on the magnetic parameters of nanorods and the internal structure of NPs. While the computational speed-up is significant when using the MS model, we analyze under what conditions the MS model does a reasonable job in reproducing hysteresis loops obtained from the more detailed simulations, and when deviations occur. As the first test of the model for describing a cluster of NPs, we compare the global hysteresis loop of two chained NPs with two MSs. In the appendices of chapter 4, we investigate the combined effects of exchange and magnetostatic interactions, perhaps some of them counter-intuitive, on the magnetization dynamics of two nanorods at various distances and arrangements, as well as the correlation between the cell size and the suitable integration time step for simulations at finite temperature.

The fifth chapter reports on the continued comparison between simulations of multiple complex NPs (nanorod composites) and MSs in multiple arrangements, including chains, triangles, and an FCC cluster. Comparing hysteresis loops of clusters of NPs and MSs reveals some limitations of the MS approximation and emphasizes the necessity of simulating complex NPs, particularly at closer inter-NP distances. We look at the local hysteresis loops of individual MSs in clusters to better understand experimental studies that report on effective hyperthermia treatment in the absence of global heating. We explore the possibility, unsuccessfully, of improving the performance of the MS model by including an additional anisotropy axis in order to

mimic the internal structure of complex NPs. We also quantify the effect of magnetic parameter distributions on the loop area. Finally, we test the scaling approach based on relating the sweep rate of the AC field and damping constant, introduced in the first paper, for multiple NPs and MSs for two different micromagnetic software frameworks.

In Chapter 6, we summarize our results and suggest possibilities for future work.

In appendix A, we present calculations of the magnetostatically-induced shape anisotropy of a rectangular prism (nanorod).

Bibliography

[1] P. Das, M. Colombo, and D. Prosperi. Recent advances in magnetic fluid hyperthermia for cancer therapy. *Colloids Surf. B*, 174:42–55, 2019.

[2] R. H. Muller and C. M. Keck. Challenges and solutions for the delivery of biotech drugs–a review of drug nanocrystal technology and lipid nanoparticles. *J. Biotechnol.*, 113(1-3):151–170, 2004.

[3] S. Sharma, S. Singhal, A. P. S. Sandhu, S. Ghoshal, B. D. Gupta, and N. S. Yadav. Local thermo-radiotherapy in carcinoma cervix: improved local control versus increased incidence of distant metastasis. *J. Obstet. Gynaecol. Res*, 17 (1):5–12, 1991.

[4] J. Overgaard, D. G. Gonzalez, M. C. C. H. Hulshof, G. Arcangeli, O. Dahl, O. Mella, and S. M. Bentzen. Hyperthermia as an adjuvant to radiation therapy of recurrent or metastatic malignant melanoma. a multicentre randomized trial by the european society for hyperthermic oncology. *Int. J. Hyperth.*, 12(1):3–20, 1996.

[5] R. Colombo, A. Salonia, Z. Leib, M. Pavone-Macaluso, and D. Engelstein. Long-term outcomes of a randomized controlled trial comparing thermochemotherapy with mitomycin-C alone as adjuvant treatment for non-muscle-invasive bladder cancer (NMIBC). *BJU Int.*, 107(6):912–918, 2011.

[6] R. Hamazoe, M. Maeta, and N. Kaibara. Intraperitoneal thermochemotherapy for prevention of peritoneal recurrence of gastric cancer. final results of a randomized controlled study. *Cancer*, 73(8):2048–2052, 1994.

[7] D. Chang, M. Lim, J. A. Goos, R. Qiao, Y. Y. Ng, F. M. Mansfeld, M. Jackson, T. P. Davis, and M. Kavallaris. Biologically targeted magnetic hyperthermia: Potential and limitations. *Front. Pharmacol.*, 9, 2018.

[8] S. Laurent, D. Forge, M. Port, A. Roch, C. Robic, L. Vander Elst, and R. N. Muller. Magnetic iron oxide nanoparticles: synthesis, stabilization, vectorization, physicochemical characterizations, and biological applications. *Chem. Rev.*, 108 (6):2064–2110, 2008.

[9] R. Hergt and S. Dutz. Magnetic particle hyperthermia—biophysical limitations of a visionary tumour therapy. *J. Magn. Magn. Mater.*, 311(1):187–192, 2007.

[10] C. L. Dennis, A. J. Jackson, J. A. Borchers, P. J. Hoopes, R. Strawbridge, A. R. Foreman, J. Van Lierop, C. Grüttner, and R. Ivkov. Nearly complete regression of tumors via collective behavior of magnetic nanoparticles in hyperthermia. *Nanotechnology*, 20(39):395103, 2009.

[11] S. Blundell. *Magnetism in Condensed Matter*. Oxford University Press Inc., New York, 2009.

[12] C. L. Dennis and R. Ivkov. Physics of heat generation using magnetic nanoparticles for hyperthermia. *Int. J. Hyperth.*, 29(8):715–729, 2013.

[13] R. E. Rosensweig. Heating magnetic fluid with alternating magnetic field. *J. Magn. Magn. Mater.*, 252:370–374, 2002.

[14] D. P. Valdés, E. Lima Jr, R. D. Zysler, and E. De Biasi. Modeling the magnetic-hyperthermia response of linear chains of nanoparticles with low anisotropy: a key to improving specific power absorption. *Phys. Rev. Appl.*, 14(1):014023, 2020.

[15] D. Cabrera, A. Coene, J. Leliaert, E. J. Artés-Ibáñez, L. Dupré, N. D. Telling, and F. J. Teran. Dynamical magnetic response of iron oxide nanoparticles inside live cells. *ACS Nano*, 12(3):2741–2752, 2018.

[16] K. Simeonidis, M. P. Morales, M. Marciello, M. Angelakeris, P. de La Presa, A. Lazaro-Carrillo, A. Tabero, A. Villanueva, O. Chubykalo-Fesenko, and D. Serantes. In-situ particles reorientation during magnetic hyperthermia application: Shape matters twice. *Sci. Rep.*, 6:38382, 2016.

[17] M. Anand, J. Carrey, and V. Banerjee. Spin morphologies and heat dissipation in spherical assemblies of magnetic nanoparticles. *Phys. Rev. B*, 94(9):094425, 2016.

[18] M. Anand. Hysteresis in a linear chain of magnetic nanoparticles. *J. Appl. Phys.*, 128(2):023903, 2020.

[19] P. Torche, C. Munoz-Menendez, D. Serantes, D. Baldomir, K. L. Livesey, O. Chubykalo-Fesenko, S. Ruta, R. Chantrell, and O. Hovorka. Thermodynamics of interacting magnetic nanoparticles. *Phys. Rev. B*, 101(22):224429, 2020.

[20] D. Serantes, K. Simeonidis, M. Angelakeris, O. Chubykalo-Fesenko, M. Marciello, M. D. P. Morales, D. Baldomir, and C. Martinez-Boubeta. Multiplying magnetic hyperthermia response by nanoparticle assembling. *J. Phys. Chem. C*, 118(11): 5927–5934, 2014.

[21] B. Mehdaoui, R. P. Tan, A. Meffre, J. Carrey, S. Lachaize, B. Chaudret, and M. Respaud. Increase of magnetic hyperthermia efficiency due to dipolar interactions in low-anisotropy magnetic nanoparticles: Theoretical and experimental results. *Phys. Rev. B*, 87(17):174419, 2013.

[22] M. Colombo, S. Carregal-Romero, M. F. Casula, L. Gutiérrez, M. P. Morales, I. B. Böhm, J. T. Heverhagen, D. Prosperi, and W. J. Parak. Biological applications of magnetic nanoparticles. *Chem. Soc. Rev.*, 41(11):4306–4334, 2012.

[23] M. J. Donahue and D. G. Porter. *OOMMF User's Guide, Version 1.0, Interagency Report NISTIR 6376*. National Institute of Standards and Technology, Gaithersburg, MD, Sept 1999. URL `https://math.nist.gov/oommf/`.

[24] A. Vansteenkiste and B. Van de Wiele. Mumax: A new high-performance micromagnetic simulation tool. *J. Magn. Magn. Mater.*, 323(21):2585–2591, 2011.

[25] J. Leliaert, A. Vansteenkiste, A. Coene, L. Dupré, and B. Van Waeyenberge. Vinamax: a macrospin simulation tool for magnetic nanoparticles. *Med. Biol. Eng. Comput.*, 53(4):309–317, 2015.

[26] B. D. Cullity and C. D. Graham. *Introduction to magnetic materials*. John Wiley & Sons, 2011.

[27] Y. V. Kolen'ko, M. Bañobre-López, C. Rodríguez-Abreu, E. Carbó-Argibay, A. Sailsman, Y. Piñeiro-Redondo, M. F. Cerqueira, D. Y. Petrovykh, K. Kovnir, O. I. Lebedev, et al. Large-scale synthesis of colloidal Fe_3O_4 nanoparticles exhibiting high heating efficiency in magnetic hyperthermia. *J. Phys. Chem. C*, 118(16):8691–8701, 2014.

[28] C. J. Goss. Saturation magnetisation, coercivity and lattice parameter changes in the system Fe_3O_4–γFe_2O_3, and their relationship to structure. *Phys. Chem. Miner.*, 16(2):164–171, 1988.

[29] L. Nagy, W. Williams, L. Tauxe, and A. R. Muxworthy. From nano to micro: Evolution of magnetic domain structures in multidomain magnetite. *Geochemistry, Geophysics, Geosystems*, 20(6):2907–2918, 2019.

[30] R. B. Kamble, V. Varade, K. Ramesh, and V. Prasad. Domain size correlated magnetic properties and electrical impedance of size dependent nickel ferrite nanoparticles. *AIP Advances*, 5(1):017119, 2015.

[31] M. Plischke and B. Bergersen. *Equilibrium statistical physics*. World scientific, 1994.

[32] S. Dutz and R. Hergt. Magnetic nanoparticle heating and heat transfer on a microscale: basic principles, realities and physical limitations of hyperthermia

for tumour therapy. *Int. J. Hyperth.*, 29(8):790–800, 2013.

[33] W. F. Brown Jr. Thermal fluctuations of a single-domain particle. *Phys. Rev.*, 130(5):1677, 1963.

[34] W. J. Atkinson, I. A. Brezovich, and D. P. Chakraborty. Usable frequencies in hyperthermia with thermal seeds. *IEEE. Trans. Biomed. Eng.*, (1):70–75, 1984.

[35] P. G. Bercoff and H. R. Bertorello. Exchange constants and transfer integrals of spinel ferrites. *J. Magn. Magn. Mater.*, 169(3):314–322, 1997.

[36] M. L. Glasser and F. J. Milford. Spin wave spectra of magnetite. *Phys. Rev.*, 130(5):1783, 1963.

[37] Spinel, perovskite, and rutile structures, 2020, December. [Online; available from: https://chem.libretexts.org/@go/page/183344, accessed 15.03.2021].

[38] C. M. Srivastava and R. Aiyar. Spin wave stiffness constants in some ferrimagnetics. *J. Phys. C: Solid St. Phys.*, 20(8):1119, 1987.

[39] C. M. Srivastava, G. Srinivasan, and N. G. Nanadikar. Exchange constants in spinel ferrites. *Phys. Rev. B*, 19(1):499, 1979.

[40] M. Uhl and B. Siberchicot. A first-principles study of exchange integrals in magnetite. *J. Phys. Condens. Matter*, 7(22):4227, 1995.

[41] B. B. N. and W. H. Inelastic scattering of neutrons in solids and liquids. *Vienna:IAEA*, page 297, 1962.

[42] Y. A. Koksharov. Magnetism of nanoparticles: effects of size, shape, and interactions. *Magnetic nanoparticles*, 1, 2009.

[43] A. G. Kolhatkar, A. C. Jamison, D. Litvinov, R. C. Willson, and T. R. Lee. Tuning the magnetic properties of nanoparticles. *Int. J. Mol. Sci.*, 14(8):15977–16009, 2013.

[44] C. Munoz-Menendez, D. Serantes, J. M. Ruso, and D. Baldomir. Towards improved magnetic fluid hyperthermia: major-loops to diminish variations in local heating. *Phys. Chem. Chem. Phys.*, 19(22):14527–14532, 2017.

[45] Y. Labaye, O. Crisan, L. Berger, J.-M. Greneche, and J. M. D. Coey. Surface anisotropy in ferromagnetic nanoparticles. *J. Appl. Phys.*, 91(10):8715–8717, 2002.

[46] D. Thapa, V. R. Palkar, M. B. Kurup, and S. K. Malik. Properties of magnetite nanoparticles synthesized through a novel chemical route. *Mater. Lett.*, 58(21): 2692–2694, 2004.

[47] N. A. Usov. Low frequency hysteresis loops of superparamagnetic nanoparticles with uniaxial anisotropy. *J. Appl. Phys.*, 107(12):123909, 2010.

[48] N. A. Usov, S. A. Gudoshnikov, O. N. Serebryakova, M. L. Fdez-Gubieda, A. Muela, and J. M. Barandiarán. Properties of dense assemblies of magnetic nanoparticles promising for application in biomedicine. *J. Supercond. Nov. Magn.*, 26(4):1079–1083, 2013.

[49] A. H. Morrish. *Thermal, Relaxation, and Resonance Phenomena in Paramagnetic Materials*, chapter 3, pages 78–148. John Wiley & Sons, Ltd, 2013. ISBN 9780470546581.

[50] G. S. Abo, Y.-K. Hong, J. Park, J. Lee, W. Lee, and B.-C. Choi. Definition of magnetic exchange length. *IEEE Trans. Magn.*, 49(8):4937–4939, 2013.

[51] B. M. Moskowitz and S. L. Halgedahl. Theoretical temperature and grain-size dependence of domain state in x= 0.6 titanomagnetite. *J. Geophys. Res. Solid Earth*, 92(B10):10667–10682, 1987.

[52] C. Abert, L. Exl, G. Selke, A. Drews, and T. Schrefl. Numerical methods for the stray-field calculation: A comparison of recently developed algorithms. *J. Magn. Magn. Mater.*, 326:176–185, 2013.

[53] M. L. Plumer, J. van Lierop, B. W. Southern, and J. P. Whitehead. Micromagnetic simulations of interacting dipoles on an fcc lattice: application to nanoparticle assemblies. *J. Phys. Condens. Matter*, 22(29):296007, 2010.

[54] R. Řezníček, V. Chlan, H. Štěpánková, P. Novák, and M. Maryško. Magnetocrystalline anisotropy of magnetite. *J. Phys. Condens. Matter*, 24(5):055501, 2012.

[55] G. Shi, R. Takeda, S. B. Trisnanto, T. Yamada, S. Ota, and Y. Takemura. Enhanced specific loss power from Resovist® achieved by aligning magnetic easy axes of nanoparticles for hyperthermia. *J. Magn. Magn. Mater.*, 473:148–154, 2019.

[56] T. Yoshida, K. Enpuku, F. Ludwig, J. Dieckhoff, T. Wawrzik, A. Lak, and M. Schilling. Characterization of Resovist® nanoparticles for magnetic particle imaging. In *Magnetic Particle Imaging*, pages 3–7. Springer, 2012.

[57] P. Reimer and T. Balzer. Ferucarbotran (Resovist): a new clinically approved RES-specific contrast agent for contrast-enhanced MRI of the liver: properties, clinical development, and applications. *Eur. Radiol.*, 13(6):1266–1276, 2003.

[58] M. Kirschner, T. Schrefl, F. Dorfbauer, G. Hrkac, D. Suess, and J. Fidler. Cell size corrections for nonzero-temperature micromagnetics. *J. Appl. Phys.*, 97(10):

10E301, 2005.

[59] M. Kirschner, T. Schrefl, G. Hrkac, F. Dorfbauer, D. Suess, and J. Fidler. Relaxation times and cell size in nonzero-temperature micromagnetics. *Physica B Condens. Matter*, 372(1-2):277–281, 2006.

[60] X. Feng and P. B. Visscher. Coarse-graining Landau–Lifshitz damping. *J. Appl. Phys.*, 89(11):6988–6990, 2001.

[61] G. Grinstein and R. H. Koch. Coarse graining in micromagnetics. *Phys. Rev. Lett.*, 90(20):207201, 2003.

Chapter 2

Methods

The goal of this chapter is to provide introductory information about the mathematical problem that we are solving.

We begin with the Stoner-Wohlfarth model, which describes the magnetization dynamics in non-interacting, uniformly-magnetized particles that are fixed in space. This model, which includes uniaxial magnetic anisotropy and an external field, is a basis for understanding hysteresis loops for ferromagnetic and superparamagnetic nanoparticles. The energy of the system, which is a function of the relative orientations of field, anisotropy axis and magnetization, is the key quantity for describing hysteresis loops analytically, both at zero and finite T.

We then introduce the Landau-Lifshitz-Gilbert (LLG) equation that describes magnetization dynamics in magnetic materials, and is the basis for micromagnetics. After discussing numerical approaches, we solve the LLG equation, using both our own code and a software framework developed by others, for a few simple cases. By simulating the Heisenberg model, we confirm our choice for the exchange constant for magnetite.

Finally, we discuss the basis of the coarse-graining method that we employ in our simulations of the next three chapters.

2.1 Stoner-Wohlfarth model

A foundation for studying magnetic nanoparticles is the Stoner-Wohlfarth (SW) model, in which the hysteresis loop is calculated for an immobile non-interacting single-domain magnetic particle with a single uniaxial anisotropy by averaging over external magnetic field directions. Relevant vectors of the model are illustrated in Fig. 2.1a. A particle's energy is the sum of the anisotropy and Zeeman contributions. As shown in Fig. 2.1b, energy minima are separated by an energy barrier due to the crystalline anisotropy, and changing the field strength alters the magnetization's stable positions. At zero temperature, the magnetization vector flips to the global energy minimum only when the energy barrier disappears. However, at a finite temperature, the required energy to overcome the barrier can be supplied through thermal fluctuations in a statistical process.

A particle's energy depends on (see Fig. 2.1a) the angle between the magnetization and the anisotropy axis θ, the angle between the applied field and the anisotropy axis θ_0, and the angle between the magnetization and the applied field, which for planar geometry is $\phi = \theta_0 - \theta$, and can be expressed as,

$$E = K_{\mathrm{u}} V \sin^2\theta - \mu_0 M_{\mathrm{s}} V H \cos(\theta_0 - \theta), \tag{2.1}$$

where K_u is the uniaxial anisotropy energy density, V is the magnetized volume, M_{s} is the saturation magnetization and μ_0 is the vacuum permeability. For the present discussion, we can restrict ourselves to planar geometry because the energy barriers

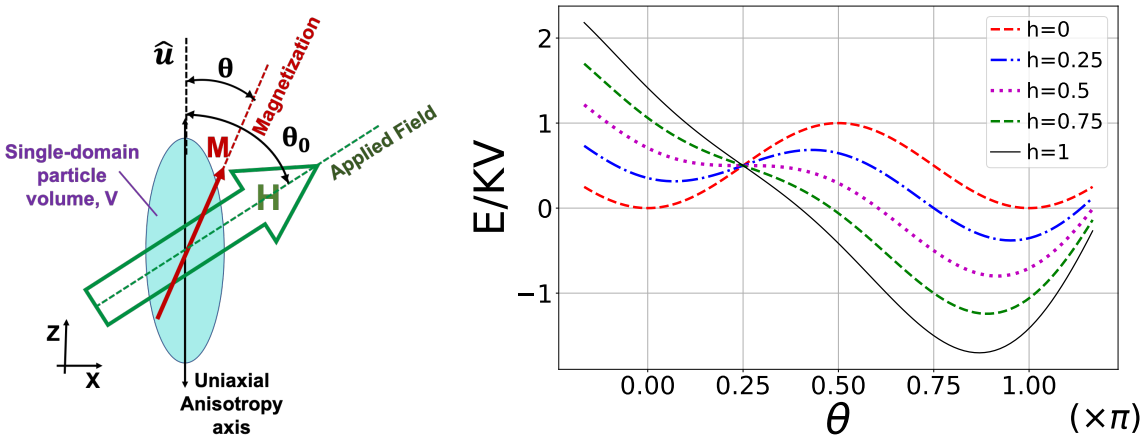

Figure 2.1: a) Stoner-Wohlfarth particle with an effective uniaxial anisotropy under application of an external field, b) the reduced energy ($E_{\rm tot}/K_{\rm u}V$) as a function of θ, when $\theta_0 = 3\pi/4$ and $h_c \simeq 0.5$ (see Eqs. 2.1 - 2.3). For $h < 0.5$, two energy minima are present, and they are separated by a maximum. At a threshold value of $h \approx 0.5$ the metastable minimum merges with the maximum, and so for $h \geq 0.5$, there is only a single energy minimum.

separating energy minima are lowest in the planar geometry, i.e., for nonplanar geometry barriers are higher, so crossing the barrier in nonplanar geometry is less likely; for planar geometry the maxima separating local minima are in fact saddle points. To find the equilibrium position of the magnetic moment $\boldsymbol{\mu}$, the lowest magnetic energy needs to be found. Normalizing the total energy by the anisotropy energy, $K_u V$, and defining the normalized field $h = H/H_k$ with the anisotropy field $H_k = 2K_u/(\mu_0 M_{\rm s})$, changes Eq. 2.1 to

$$\frac{E}{K_{\rm u}V} = \sin^2\theta - 2h\cos(\theta_0 - \theta). \tag{2.2}$$

Under variation of the field strength, the competition between Zeeman and anisotropy energies determines the magnetization vector's energetically stable direction. When the field is switched to point in the opposite direction, the stable direction becomes metastable (i.e. is now merely a local minimum). At a critical field strength of H_c (normalized field strength $h_c = H_c/H_k$), when the magnetization makes angle θ_c with

the anisotropy axis, the energy barrier disappears and $\boldsymbol{\mu}$ flips to its stable position. To find the critical point using roots of the first and second derivatives of the normalized energy in Eq.2.2 with respect to θ, we get [1],

$$\tan^3\theta_c = -\tan\theta_0, \quad h_c^2 = 1 - \frac{3}{4}\sin^2 2\theta_c, \tag{2.3}$$

conditions that give the reduced critical field as a function of the θ_0 (field angle). Fig. 2.1b shows the reduced energy profile as a function of θ for various field magnitudes when $\theta_0 = 3\pi/4$ and $h_c \sim 0.5$. The figure shows the stable directions of the magnetization at different field strengths. As can be seen, for $H < H_c$, or equivalently $h < h_c$, there are two energy minima separated by an energy barrier, and at $H = H_c$ the metastable minimum merges with the maximum to become a point of inflection and the energy barrier disappears: a further increase in the field will cause the magnetization, initially in the now-absent metastable minimum, to flip. For $H > H_c$, only one minimum remains.

2.1.1 Analytical solution for SW model at $T = 0$

Wood et al. [2] provided an analytic solution for the magnetization dynamics of a SW particle under the application of an applied field and determined the hysteresis loop at $T = 0$, i.e. they solved Eq. 2.2. Fig. 2.2 represents hysteresis loops for a SW particle corresponding to selected field directions and an average loop for randomly oriented particles.

As a brief summary of the Wood et al.'s solution, they normalized the energy by defining $\omega = E/(K_u V)$, and solved $\partial\omega/\partial\phi = 0$ and $\partial^2\omega/\partial\phi^2 > 0$ to find the magnetization state as a function of the applied field. When the field magnitude

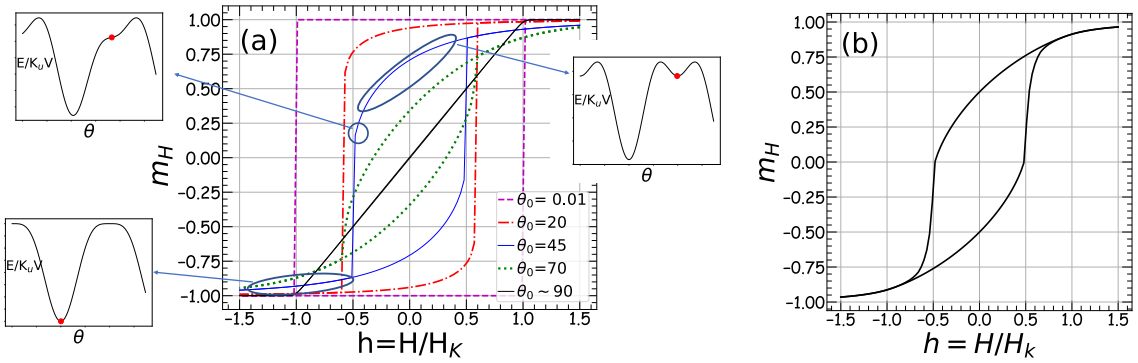

Figure 2.2: a) Hysteresis loop for selected θ_0 and magnetization energy profile according to the field strength. b) Average hysteresis loop for a collection of randomly oriented SW particles.

changes along a fixed axis, the magnetization vector is restricted to a plane containing **H** and anisotropy axis $\hat{\mathbf{u}}$ (for example, the xz plane in Fig. 2.1). The normalized field, h, and magnetization unit vector, $\mathbf{m} = \boldsymbol{\mu}/M_{\mathrm{s}}V$, along the anisotropy axis (say $\hat{z}$) and perpendicular to it ($\hat{x}$) are written as

$$\begin{aligned} h_z &= h\cos\theta_0, \quad & h_x &= h\sin\theta_0 \\ m_z &= m\cos\theta, \quad & m_x &= m\sin\theta. \end{aligned} \tag{2.4}$$

Using these components in $\partial\omega/\partial\phi = 0$ results in,

$$h\left(\frac{\sin\theta_0}{\sin\theta} - \frac{\cos\theta_0}{\cos\theta}\right) = 1 \longrightarrow \frac{h_x}{m_x} - \frac{h_z}{m_z} = 1, \tag{2.5}$$

which gives a straight line in the $h_x - h_z$ plane parallel to the given magnetization. An equivalent equation for the inflection point can be calculated by substituting the components given in Eq. 2.4 into $\partial^2\omega/\partial\phi^2 = 0$, which gives,

$$2\cos 2\theta + 2h\cos(\theta_0 - \theta) = 0 \longrightarrow \frac{h_x}{m_x^3} + \frac{h_z}{m_z^3} = 0. \tag{2.6}$$

Solving Eq. 2.5 and 2.6 simultaneously results in the equation,

$$h_x^{2/3} + h_z^{2/3} = 1, \tag{2.7}$$

which is called the switching asteroid, representing a contour where the metastable energy minimum and the maximum merge, and the energy barrier disappears. If h lies within the asteroid, four solutions are real and if h lies outside the asteroid two of the solutions are real and two are complex. The geometric solution of Eq. 2.7 together with the constraint of fixed magnetization length ($m_x^2 + m_z^2 = 1$) result in 4th-order equations for the magnetization. For instance, the equation for m_z is

$$m_z^4 + 2h_z m_z^3 - (1 - h^2)m_z^2 + 2h_z m_z - h_z^2 = 0 \tag{2.8}$$

with solutions

$$\begin{aligned} m_z &= \frac{f}{6} \pm \frac{1}{6}\sqrt{2f^2 - 18e + \frac{54h_z(1+h_x^2)}{f}} - \frac{h_z}{2} \\ f &= \pm\sqrt{9h_z^2 + 6d + 6e}, \quad d = 1 - h^2 \\ e &= d\cos\left(\cos^{-1}\left(54h_x^2h_z^2/d^3 - 1\right)/3\right). \end{aligned} \tag{2.9}$$

Choosing the same polarity $\pm$ sign in Eqs. 2.9 corresponds to the stable solutions or energy minima.

2.1.2 Approximate analytical solution for the SW model at finite T

At finite temperature, thermal excitations allow the magnetization to switch between energy minima. The rate of switching is chiefly controlled by the energy barrier

separating the two minima. Usov et al. [3] introduced expressions for the rate of escape from a local minimum to the global minimum that can be used to calculate hysteresis loops at finite T.

They considered a low frequency alternating (reduced) field $h(t) = h_0 \sin(2\pi f t)$. Starting off with Eq. 2.2 and finding the roots of $\partial\omega/\partial\phi = \partial\omega/\partial\theta = 0$ results in three solutions ($\theta^{\mathrm{I}}_{\mathrm{min}}$, $\theta^{\mathrm{II}}_{\mathrm{min}}$, θ_{saddle}) based on the value of $\partial^2\omega/\partial\theta^2$ when $|h|$ is smaller than the critical field h_c. As noted above, when $|h| = h_c$ the saddle point and one of the minima merge and only one solution for $|h| > h_c$ remains. In the limit of high potential barrier $\sigma = KV/k_{\mathrm{B}}T \gg 1$, Usov et al. [3] used the assumption that particles are located near the minima $\theta^{\mathrm{I}}_{\mathrm{min}}$, $\theta^{\mathrm{II}}_{\mathrm{min}}$ of the potential wells and suggested the following equation for the component of the magnetization along the magnetic field,

$$\frac{\boldsymbol{\mu}_{\mathrm{h}}}{M_{\mathrm{s}}V} = m_{\mathrm{h}}(t) = n_2(t)\cos\left(\theta_0 - \theta^{\mathrm{II}}_{\mathrm{min}}(h(t))\right) + n_1(t)\cos\left(\theta_0 - \theta^{\mathrm{I}}_{\mathrm{min}}(h(t))\right), \qquad (2.10)$$

where $n_1(t)$ and $n_2(t)$ are the probabilities of finding the magnetization vector in each potential well, and $\theta^{\mathrm{I}}_{\mathrm{min}}$, $\theta^{\mathrm{II}}_{\mathrm{min}}$ and θ_{saddle} are given by,

$$\begin{aligned}
\cos\theta^{\mathrm{I}}_{\mathrm{min}} &= -\sqrt{1 - \left(\frac{h_x\sqrt{(1-h_z)^2 - h_x^2}}{h_z(1-h_z) - \sqrt{(1-h_z)^2 - h_x^2}}\right)^2}, \\
\cos\theta^{\mathrm{II}}_{\mathrm{min}} &= \sqrt{1 - \left(\frac{h_x\sqrt{(1+h_z)^2 - h_x^2}}{h_z(1+h_z) + \sqrt{(1+h_z)^2 - h_x^2}}\right)^2}, \\
\cos\theta_{\mathrm{saddle}} &= \frac{h_z\sqrt{(1-h_x)^2 - h_z^2}}{h_x(1-h_x) - \sqrt{(1-h_x)^2 - h_z^2}}.
\end{aligned} \qquad (2.11)$$

The time evolution of $n_1(t)$ and $n_2(t)$ is governed by,

$$n_1(t) + n_2(t) = 1, \qquad \frac{\partial n_1}{\partial t} = \frac{n_2}{\tau_2} - \frac{n_1}{\tau_1}, \tag{2.12}$$

where τ_i is the dwell time – the average time taken for the system localized in the θ^i_{min} potential well to overcome the energy barrier and to switch to θ^j_{min}. While full details on the calculation of τ_i can be found in Ref. [3], it depends exponentially on the energy difference between the saddle point and energy minimum at θ^i_{min}, or rather on the ratio of this difference to $k_{\text{B}}T$. Adding other interactions like exchange and magnetostatics greatly complicates the analytic determination of the magnetization dynamics, especially when the system is made of multiple particles, in which case quantities must be calculated numerically.

2.2 Magnetization dynamics with LLG equation and numerical solution

Another approach for studying magnetization dynamics is based on the torque equation (Eq. 1.8), but where magnetic interactions are accounted for by appropriate effective field terms. The resulting set of differential equations is then solved numerically. In modelling materials, we consider (small) uniformly magnetized portions of a sample, or cells, each of volume V. In reference to Eq. 1.8, for any given cell, we write $\boldsymbol{\mu} = \mathbf{M}V$ and replace $\mathbf{B}$ with $\mu_0\mathbf{H}_{\text{eff}}$, and the result is the Landau-Lifshitz (LL) equation,

$$\frac{d\mathbf{M}}{dt} = -\gamma\mu_0\mathbf{M} \times \mathbf{H}_{\text{eff}}, \tag{2.13}$$

where γ is electron's gyromagnetic ratio defined as $\gamma = eg/2m_e$, with e, m_e and $g \simeq 2$ being the electron's (absolute value of) charge, mass and g-factor, respectively. $\mathbf{H}_{\text{eff}}$ represents the collective effect of different interactions as,

$$\mathbf{H}_{\text{eff}} = \mathbf{H}_{\text{Zeeman}} + \mathbf{H}_{\text{anisotropy}} + \mathbf{H}_{\text{exchange}} + \mathbf{H}_{\text{magnetostatic}}, \tag{2.14}$$

where the fields can be calculated using energy density through,

$$\mathbf{H} = -\frac{1}{\mu_0}\frac{\partial E}{\partial \mathbf{M}}. \tag{2.15}$$

Eq. 2.13 implies that the magnetization vector precesses around the effective field forever, neglecting the reality of the decay of the magnetic moment's precession over time and the resulting alignment to the effective field. This decay is attributed to various factors such as coupling of magnetic moments to the lattice, lattice disorder, defects, impurities, etc. Gilbert [4] suggested adding a damping term to the effective field to incorporate this phenomenon,

$$\mathbf{H}_{\text{eff}} \longrightarrow \mathbf{H}_{\text{eff}} - \eta\frac{d\mathbf{M}}{dt}, \tag{2.16}$$

where the damping coefficient $\eta = \alpha/(\mu_0\gamma M_{\text{s}})$ depends on a dimensionless phenomenological damping constant α, an intrinsic property of the material [4]. Rewriting the LL equation, but using the variable $\mathbf{m} = \mathbf{M}/M_{\text{s}}$, writing $\gamma_1 = \mu_0\gamma$ and applying the damping effect, results in the Landau-Lifshitz-Gilbert (LLG) equation,

$$\frac{d\mathbf{m}}{dt} = -\left(\frac{\gamma_1}{1+\alpha^2}\right)\mathbf{m} \times \mathbf{H}_{\text{eff}} - \left(\frac{\gamma_1\alpha}{1+\alpha^2}\right)\mathbf{m} \times (\mathbf{m} \times \mathbf{H}_{\text{eff}}). \tag{2.17}$$

To study systems at finite temperature, based on the fluctuation-dissipation theorem [5] a stochastic term can be added to include the effect of thermal fluctuations on system properties,

$$\mathbf{H}_{\text{thermal}} = \mathbf{\Gamma}\sqrt{\frac{2\alpha k_{\text{B}}T}{V\mu_0\gamma_1 M_{\text{s}}\Delta t}}, \tag{2.18}$$

where $\mathbf{\Gamma} = \mathbf{\Gamma}(t)$ is a random vector with Cartesian components drawn at each time step from a Gaussian distribution with zero mean and unit variance. Given the dependence of $\mathbf{H}_{\text{thermal}}$ on V (cell volume) and the time step Δt of the numerical solver, one needs to be careful in choosing an appropriate Δt, particularly for small V.

With the addition of $\mathbf{H}_{\text{thermal}}$, the resulting equation is called the stochastic LLG (sLLG) equation. We note that there are slightly different variations in how precisely the stochastic term enters the equation. The sLLG equation can be used to study the magnetization dynamics for low to high damping limits ($\alpha \sim 0.001 - 1$).

2.2.1 Numerical schemes

Numerical methods are usually used for studying systems too complicated to solve analytically, as in most nonlinear problems. In solving an ordinary differential equation as an initial value problem, we usually have the general form,

$$\begin{aligned} dy &= f(y(t))dt, \\ y(t+\Delta t) - y(t) &= \int_t^{t+\Delta t} f(y(t), t)dt, \end{aligned} \tag{2.19}$$

Various numerical schemes interpret the right-hand side integral differently. For calculating $f(y)$ at discrete points in time (t, $t+\Delta t$, $t+2\Delta t$, ...) the following notation

is commonly used,

$$\begin{aligned} t_n &= t, \qquad t_{n+1} = t + \Delta t \\ y_n &= y(t), \qquad y_{n+1} = y(t + \Delta t) \\ f(y_n) &= f(y(t), t). \end{aligned} \tag{2.20}$$

The simplest method, the Euler method, uses the value of f at the beginning of the time interval for calculating the integral in Eq. 2.19, resulting in time-stepping algorithm accurate to first order in Δt,

$$y_{n+1} = y_n + f(y_n)\Delta t. \tag{2.21}$$

Although not typically used to solve ordinary differential equations (ODEs), the Euler method is straight-forward to implement, and therefore useful when checking computer codes. It is more frequently used for solving stochastic ODEs, for which it is trickier to show that a given method correctly treats the stochastic terms.

Different methods suggest considering contributions of f values at various points in the time interval. The order of methods is defined based on the highest power of Δt that is considered in the approximation. An example of higher-order methods is the 4th-order Runge-Kutta (RK4), in which four points with different weights are

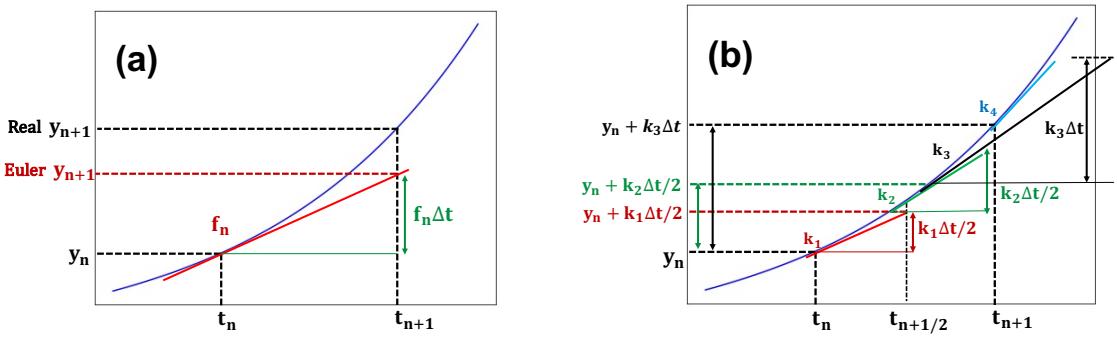

Figure 2.3: a) In the Euler method $f_n = f(y_n)$ is used over the entire time interval Δt. b) In the RK4 method, the values of f at the beginning and end points, as well as at two midpoints, are used to find a more accurate approximation for y_{n+1}.

considered in the integral calculations,

$$\begin{aligned} k_1 &= f(y_n), \\ k_2 &= f(y_n + k_1\Delta t/2), \\ k_3 &= f(y_n + k_2\Delta t/2), \\ k_4 &= f(y_n + k_3\Delta t), \\ y_{n+1} &= y_n + (k_1 + 2k_2 + 2k_3 + k_4), \Delta t/6 + \mathcal{O}(\Delta t^5). \end{aligned} \tag{2.22}$$

A graphical illustration of Euler and RK4 method are shown in Fig. 2.3.

2.2.2 Our code for a single SW particle

As an exercise, we wrote code in Python to simulate the dynamics of a single magnetic moment subject to a fixed uniaxial anisotropy in an opposing field at zero temperature by applying Euler and RK4 integrating methods to solve the LLG equation. Here we use $\gamma_1 = \mu_0\gamma = 2.211 \times 10^5$ rad.A/s. The LLG equation predicts the time evolution of the magnetization vector with a fixed magnitude equal to its maximum

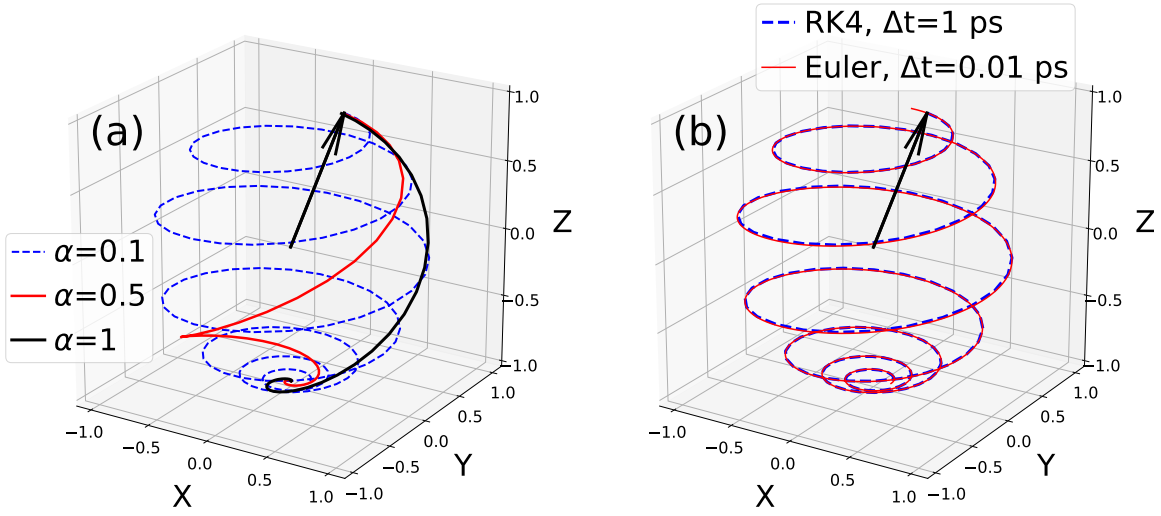

Figure 2.4: SW particle spin dynamics from our own numerical integration of the LLG Eq. a) A higher damping parameter results in faster alignment of the magnetization with the external field. Simulation parameters are $M_s = 500$ kA/m, $H = -1.5\hat{\mathbf{z}}$ T, $\Delta t = 10^{-12}$ s and the simulation time is 0.15 ns. b) The time step required for the Euler solver is shorter than for RK4., $\alpha = 0.1$, the simulation time is 0.15 ns.

value (M_s). We start our exploration by looking at the dynamics of the unit vector of a magnetic moment ($\mathbf{m}$) when the damping factor α changes from $0.1 - 1$ in Fig. 2.4a. α represents the degree of the spin excitation coupling with the crystal lattice and energy dissipation, and as expected, the higher damping result in a faster equilibrium. We compared the solver effects on the magnetization trajectories in Fig. 2.4b when the external field is in direction given by $-\hat{\mathbf{z}}$ and the anisotropy axis is parallel to the $\hat{\mathbf{z}}$. As RK4 uses a higher-order integration scheme, the same result is achievable using a longer time step.

Numerical simulation of multiple particles using interpreted languages like Python is computationally more expensive than compiler languages like C or C++. Therefore, the use of micromagnetic software like OOMMF * [6], written in C++, is very common. However, writing our own code is an important step in ensuring that we are using

*Object Oriented Micromagnetic Framework

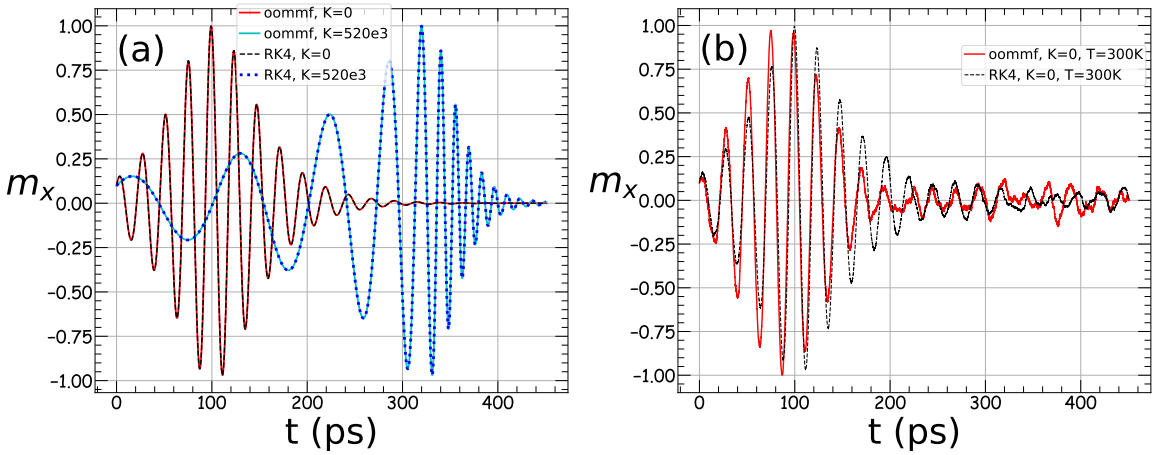

Figure 2.5: Comparing OOMMF results and those of our Python code for the time evolution of m_x for $H||\hat{z}$ at a) $T = 0$ when $K = 0$ and $K > 0$, b) $T = 300$ K, $K = 0$

software like OOMMF correctly, in that results from both should be the same.

2.2.3 OOMMF software for multiple moments

OOMMF is an open-source code developed at the National Institute of Standards and Technology (NIST). OOMMF is developed in C++, and customizing the simulations and employing user supplied functions is possible via the scripting language Tcl/Tk. OOMMF uses micromagnetics, in which a magnetization vector represents the collective behaviour of atomic spins in a cell of finite volume, and numerically solves the sLLG equation for the magnetization dynamics by taking into account different interactions such as externally applied field, cubic and uniaxial anisotropy, exchange interactions and magnetostatics. At $T = 0$, it is possible to employ different integrating solvers in OOMMF, but its stochastic thermal field is implemented in the Theta Evolve module based on the Euler scheme [7]. As a test of properly employing the software, we compared the simulation results in OOMMF with our Python code for a single SW particle.

Comparing the time evolution of the x component of a magnetization vector under the influence of an external field H_z with and without uniaxial anisotropy along the z axis shows that OOMMF's numerical result matches our Python code's, and as expected the anisotropy field alters the precession rate of the magnetization, as shown in Fig. 2.5a. To include the thermal noise into the calculations we add H_{thermal} from Eq. 2.18 to H_{eff} in Eq. 2.17. Detailed documentation about the inclusion of a stochastic thermal term in OOMMF is not provided, but the reasonable agreement between our code and OOMMF points to the similarity between implementations of the stochastic contribution to the dynamics.

In the next step, we use OOMMF to reproduce the analytically calculated normalized magnetization-field hysteresis loops for assemblies of SW particles at zero and finite temperature. As shown in Fig. 2.6a the averaged simulated hysteresis loops for 1000 noninteracting particles with randomly oriented uniaxial anisotropy under a static field at $T = 0$ matches their analytically calculated loop.

To reproduce the finite temperature results of Usov et al. [3, 8], we simulate a collection of 40 NPs under application of AC field with $f = 400$ kHz and $H_0 = 100$ Oe at $T = 300$ K as prescribed in Ref. [8] with the iron oxide magnetic parameters of $M_{\text{s}} = 350$ kA/m, $K_u = 10$ kJ/m^3 and $\alpha = 0.5$. As shown in Fig. 2.6b, the hysteresis loop obtained from OOMMF matches Usov's analytical result [8].

2.2.3.1 Heisenberg model: finding the exchange constant A using T_c

As another test of the software, we turn to the Heisenberg model, which describes a system of single-domain ferromagnets with exchange interactions. We focus on the temperature dependence of the system's magnetization and magnetic susceptibility. As expected, thermal fluctuations disturb the high degree of moment alignment

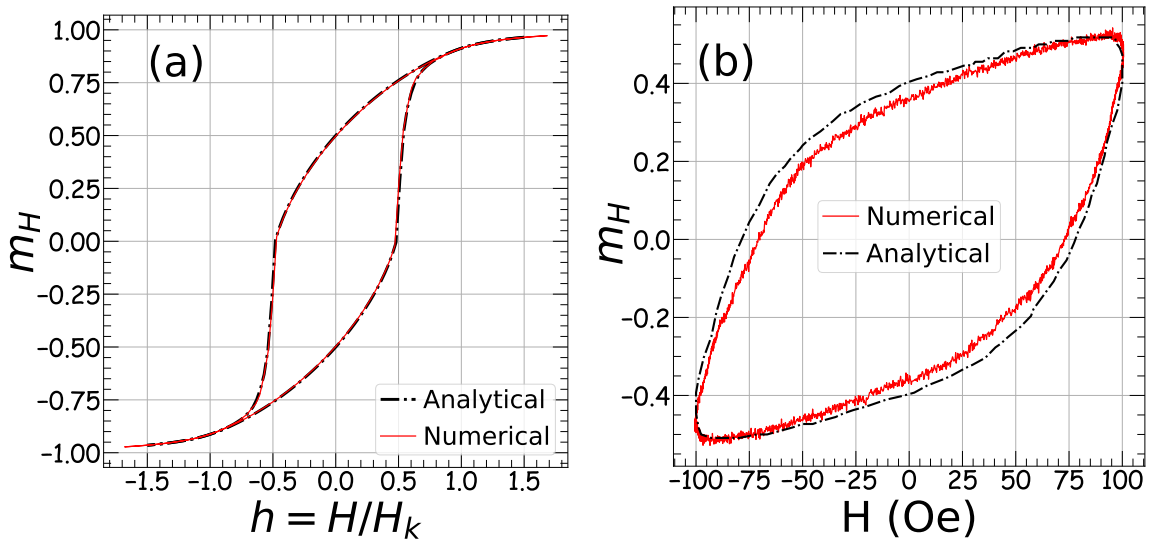

Figure 2.6: Comparing analytical solution and numerical results from OOMMF at a) $T = 0$, under a static field when $H_k = 2K/\mu_0 M_s$, b) $T = 300$ K, under an AC field with $f = 400$ kHz, $H_0 = 100$ Oe. Data for the approximate analytical solution in (b) are taken from Ref. [8].

present at lower temperatures. On heating, thermal fluctuations come to dominate the exchange interactions at a critical temperature T_c, resulting in a precipitous drop in magnetization. For $T > T_c$, the model is paramagnetic. In the thermodynamic limit, the magnetization goes to zero sharply at T_c and the susceptibility diverges at T_c. For a finite-size system, such as in our simulations, where the correlation length can not be infinite, rounding occurs: the magnetization tends to zero smoothly as T increases beyond T_c, and the susceptibility shows a finite peak near T_c.

The Heisenberg model can be used for finding proper exchange constants by matching critical temperatures between model and experiments for different magnetic materials. Here, we simulate a system of $15 \times 15 \times 15$ magnetite cells of size $a = 0.839$ nm and with $M_s = 480$ kA/m. Bulk magnetite has no uniaxial anisotropy and its Curie temperature is reported as $T_c \sim 858$ K [9]. To reduce the finite-size effects, periodic

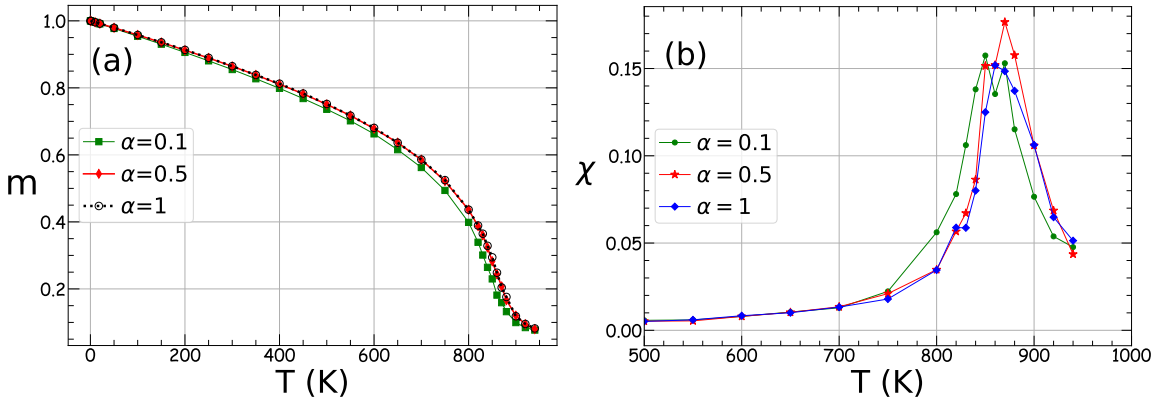

Figure 2.7: Temperature dependence of the a) normalized magnetization and b) susceptibility for a system of $15^3 = 3375$ magnetite cells interacting via exchange interactions (Heisenberg model) with periodic boundary conditions, for different damping strengths (α).

boundary conditions are employed. No field is applied. The known relationship between thermal and exchange energies at the transition temperature, from extensive Monte Carlo simulation results, is [10],

$$\frac{k_{\mathrm{B}}T_c}{6aA} = 0.24, \tag{2.23}$$

where a and A are the simulation cell size and the exchange constant, respectively, and $6aA$ represents the nearest neighbour exchange energy for a cubic lattice. Using Eq. 2.23, $A = 0.98 \times 10^{-11}$ J/m results in the experimental transition temperature, which is in agreement with experimentally calculated exchange constants from spin wave measurements of $A \simeq 1 \times 10^{-11}$ J/m for bulk magnetite [11–17]. The simulation results in Fig. 2.7a confirm that the exchange energy calculations in OOMMF use a different convention for the definition of the exchange interaction such that $A^{\mathrm{OOMMF}} = A/2$ (setting $A^{\mathrm{OOMMF}} = A$ results in $T_c \approx 2 \times 858$ K $= 1716$ K).

In addition to examining $m(T)$ at T_c, another magnetic property to study is the

response function or magnetic susceptibility $(\chi)^*$ that has a peak at T_c. Writing the magnetic moment of the entire system as a function of the normalized magnetic moment $\mathbf{m}$ and the system's volume (NV), χ can be written as,

$$\chi = \mu_0 M_{\mathrm{s}}^2 V N \frac{\langle \mathbf{m}^2 \rangle - \langle \mathbf{m} \rangle^2}{k_{\mathrm{B}} T}, \tag{2.24}$$

where N is the number of particles in the system, and V is each particle's volume. As shown in Fig. 2.7b, the susceptibility peaks at $T \simeq 858$ K, confirming our chosen value of A.

2.2.4 Coarse-graining

Micromagnetics replaces individual atomic spins inside a cell with a magnetization vector representing the spins' collective behaviour in the cell. It takes months of computer time to simulate with OOMMF a nanorod comprising $8 \times 24 \times 56 = 10752$ micromagnetic cells of the same size as the unit cell, $a_0 = 0.839$ nm, for a clinically-relevant sweep rate of SR ≤ 0.25 Oe/ns. Therefore, simulating nanorods using bigger but fewer cells is favourable to decrease the number of calculations and hence simulation time. Moreover, using bigger simulation cells allows for a longer integration time step, again resulting in faster calculations.

For simulations with cell size a_0, we use bulk values for M_{s} and K. For A, we use the value described above, since it reproduces the bulk value for T_c. If a larger cell size is chosen, and these parameters are left unchanged, the results for a hysteresis loop calculation will, in general, change for $T > 0$. This implies that to remove the cell size

*In the special case of a linear material, the magnetization $\mathbf{M}$ is linearly related to the magnetic field $\mathbf{M} = \chi \mathbf{H}$, where χ is the dimensionless quantity called magnetic susceptibility or response function. More generally it can be written as $\chi = \partial \mathbf{M} / \partial \mathbf{H}$ [18].

dependence of simulation results, magnetic parameters need to be scaled. To meet this need, different scaling approaches have been reported in the literature. For instance, Feng and Visscher [10] suggested scaling of the damping constant α, which accounts for magnetic energy loss, with cell size. In their work, they gave a prescription for how α should increase with cell size for a given T, based on the idea that a larger α accounts for the increase in the degrees of freedom available for energy dissipation when larger simulation cells are used. As another example, Kirschner et al. [19, 20] suggested an approximate scaling of M_s with cell size based on the difference of the atomic and average magnetization of blocks of spins in Monte Carlo simulations. They extended their approach to scale the exchange and uniaxial anisotropy constants, A and K respectively, to keep the exchange length, $l_\mathrm{ex} = \sqrt{2A/\mu_0 M_\mathrm{s}^2}$, and anisotropy field, $H_\mathrm{anis} = 2K/\mu_0 M_\mathrm{s}^2$, invariant with simulation cell size.

Among the different approaches for coarse-graining, we modify and use the one suggested by Grinstein and Koch [21], one which is based on renormalization group (RG) methods. After applying a phenomenological modification, we find that it provides successful cell size invariance for our system of study. Before explaining Grinstein and Koch's approach, we next review some of the relevant basic concepts and methods of the RG approach.

2.2.4.1 Renormalization Group

The discussion below is largely based on Refs. [22, 23].

Generally, phenomena that occur on different length scales do so with little mutual influence, and thus can be treated independently. For example, while intermolecular interactions in water determine basic material properties, we do not consider them

explicitly in understanding ocean waves. While practical theories need to define a limited range of length scales, there are some phenomena where features at many length scales make considerable contributions, and the RG theory has been introduced to deal with this type of problem. For example, a theoretical description of ferromagnets at T_c should include thermal fluctuations at all length scales, since the spin correlation length is infinite. In ferromagnets, spin alignment is attributed to the coupling between neighbouring spins and results in the system's energy being lowest when all the spins are aligned. The thermal motion of atoms and electrons induces spin flips that raise the energy and reduces the magnetization.

By assuming a lattice of spins with direct interactions only between nearest neighbours, the influence of the state of a single spin is propagated indirectly throughout the spin lattice via the effect that each neighbour has on its own nearest neighbours. In this context, the correlation length is defined loosely as the maximum distance that a spin flip's influence is felt on a spin lattice. For example, consider a marked spin that flips down from up; if you count the number of down spins in the vicinity of the marked spin before and after the flip, then on average there will only be a difference in this number for spins within a certain radius. This radius represents the correlation length. At high temperatures ($T > T_c$), spin orientations are largely random, and only short-range order is seen – in the form of tiny patches of mostly parallel spins. As the temperature falls, some of these patches expand so that at T_c the patches have infinite length. At T_c, a change in the spin state of an individual spin can alter the whole system's magnetization.

To solve or understand the thermodynamics of a model system, calculating the partition function leads to determining the magnetization and other macroscopic properties. To do so, we need to calculate the probability of every spin configuration, and

it is clear that more spins in the system mean more degrees of freedom, and more spin configurations should be taken into account. The RG strategy is to break down a problem consisting of multiple length scales into a sequence of smaller problems, each dealing with a single length scale. One of the techniques usually used for explaining the RG application is the spin-block technique initially introduced by Leo P. Kadanoff. For simplicity, consider the Ising model on a 2-dimensional square lattice, where spins can only be in one of two states, up or down. By considering 4 spins arranged in a 2 by 2 square, 16 different spin configurations can be achieved (2^4), and in the case of 3 spins along each dimension, $2^{3^2} = 512$ possible configurations should be taken into account and so on. The answer to the question about the minimum size of the lattice needed for determining the system's properties is that the system should be as large as the largest observed fluctuations, which means the correlation length at each temperature. For instance, at a temperature close to T_c, the correlation length might be as large as 100 lattice spacing (a_0), which implies the largest fluctuations would cover about 10000 lattice sites and calculating 2^{10000} configurations is not possible with even the fastest current computers. To overcome this problem, the spin-block technique suggests building up a second lattice with twice the lattice spacing ($2a_0$) in which the block's spin state of up or down is determined based on the majority rule of the four spins on the original lattice. Hence the number of degrees of freedom is decreased, e.g., an original lattice of four by four spins with 2^{16} possible configurations is replaced with two by two spins with 2^4 possible configurations. Therefore, fluctuations between a_0 to $2a_0$ length are integrated out and just those with orders from $2a_0$ to the correlation length need to be considered. The spin-block technique suggests repeating this procedure for the second lattice and replacing four of the block-spins with one spin on a third lattice with lattice spacing twice the second lattice (or $4a_0$) and so on until the lattice spacing reaches the correlation length, and only correlation

length order fluctuations remain to be considered.

The coupling strength determines the probability of any two adjacent spins being parallel, so to keep the sum of the configuration probabilities constant when blocking the spins, the effective coupling strength needs to change. (In this model, we neglect the atoms and electrons and just assume spins on lattice sites.) However, changing the coupling strength by a certain factor is equivalent to changing the temperature by the inverse of the same factor. We can think of the effective coupling strength as being equivalent to an inverse temperature, i.e. at very high temperatures ($T \gg T_c$), the coupling strength is effectively zero, so the spins are randomly oriented and the magnetization is zero, and the correlation length is zero. In other words, the change of the spin coupling is equivalent to the temperature change in the original lattice. Reducing the number of degrees of freedom through the blocking of spins is also reflected in a change in the magnetization M. Hence, M needs to be rescaled as well.

2.2.4.2 Momentum shell Renormalization Group

For systems with degrees of freedom that can be written in terms of Fourier modes of a given field (such as spin systems), momentum-space RG can be applied. The RG coarse-graining in real space achieved by eliminating the small length scale fluctuations is equivalent to integrating out the high momentum modes ($\Lambda/b < k < \Lambda$ for $b > 1$, $\Lambda = 2\pi/a_0$,) since the shortest length scales are related to the largest wavenumbers, and is called the momentum shell approach [24]. Kadanoff suggested taking advantage of the property that the system's appearance at different length scales is similar in order to eliminate the correlated degrees of freedom at length scales significantly smaller than the correlation length. Probing the system at different length scales is analogous to various resolutions in looking at the system's digital picture when the

pixel size is a_0 [25]. The momentum-space RG transformation is carried out in three steps. In the first step, called coarse-graining, degrees of freedom corresponding to the large wavenumbers ($\Lambda/b < k < \Lambda$ for $b > 1$, $\Lambda = 2\pi/a_0$) are integrated out. In the second step, the wave vector (k) is rescaled to restore the original range of degrees of freedom, and in the third step, the spin variables are renormalized to restore the spatial dependency of the fluctuations. To show a simple example of implementing the momentum space RG transformation, we need a partition function based on the spin waves in momentum space. Consider an Ising-like Hamiltonian, written in terms of the scalar spin function $\phi(\mathbf{x})$, that includes exchange interactions between neighbouring spins. The partition function is given by,

$$\mathcal{Z} = \int \mathcal{D}\phi(\mathbf{x}) \exp\left[-\int \left(r\phi^2(\mathbf{x}) - D\phi(\mathbf{x})\nabla^2\phi(\mathbf{x}) + u\phi(\mathbf{x})^4 + ...\right) d\mathbf{x}\right], \qquad (2.25)$$

where $\int \mathcal{D}\phi(\mathbf{x})$ represents the functional integral over the smooth function $\phi(\mathbf{x})$ for a d-dimensional system, $\mathbf{x} = (x_1, x_2, ...x_d)$. Coefficients r, D and u are defined in terms of the exchange constant $\tilde{J} = J/k_BT$, lattice spacing a_0, and the number of nearest neighbors $z = 2 \times d$, as,

$$r = \tilde{J}z(1 - \tilde{J}z)/2, \qquad D = -\tilde{J}a_0^2(1 - 2\tilde{J}z)/2, \qquad u = (\tilde{J}z)^4/12. \qquad (2.26)$$

Using the mean-field estimate of the transition temperature $k_{\mathrm{B}}T_c = Jz$ results in the temperature dependence of these parameters being given by,

$$r = \frac{T_c}{2T^2}(T - T_c), \qquad D = \frac{a_0^2 T_c}{2zT^2}(2T_c - T), \qquad u = \left(\frac{T_c}{T}\right)^4/12. \qquad (2.27)$$

To start, we only consider the quadratic terms in Eq. 2.25, which is called Gaussian theory. Taking the Fourier transform of $\phi(\mathbf{x})$ with integration over a d-dimensional

hypersphere of radius $\Lambda = 2\pi/a_0$ as,

$$\phi(\mathbf{x}) = \int_0^{\Lambda} \frac{d\mathbf{k}}{(2\pi)^d} \phi(\mathbf{k}) e^{i\mathbf{k}\cdot\mathbf{x}}, \tag{2.28}$$

results in the partition function of the form,

$$\mathcal{Z} = \int \mathcal{D}\phi(\mathbf{k}) \exp\left[-\int_0^{\Lambda} \frac{d\mathbf{k}}{(2\pi)^2} (r + Dk^2) |\phi(\mathbf{k})|^2 \right]. \tag{2.29}$$

Now we can start the RG transformation. In the first step, the spin function is separated into contributions from small and large wavenumbers, the latter of which are going to be integrated out, as,

$$\phi(\mathbf{k}) = \begin{cases} \phi_<(\mathbf{k}), & 0 < k < \Lambda/b \\ \phi_>(\mathbf{k}), & \Lambda/b < k < \Lambda, \end{cases} \tag{2.30}$$

and the partition function reads,

$$\begin{aligned} \mathcal{Z} = & \int \mathcal{D}\phi_<(\mathbf{k}) \int \mathcal{D}\phi_>(\mathbf{k}) \exp\left[-\int_0^{\Lambda/b} \frac{d\mathbf{k}}{(2\pi)^2} (r + Dk^2) |\phi_<(\mathbf{k})|^2 \right] \\ & \times \exp\left[-\int_{\Lambda/b}^{\Lambda} \frac{d\mathbf{k}}{(2\pi)^2} (r + Dk^2) |\phi_>(\mathbf{k})|^2 \right] \\ = & \mathcal{Z}_> \int \mathcal{D}\phi_<(\mathbf{k}) \exp\left[-\int_0^{\Lambda/b} \frac{d\mathbf{k}}{(2\pi)^2} (r + Dk^2) |\phi_<(\mathbf{k})|^2 \right]. \end{aligned} \tag{2.31}$$

$\mathcal{Z}_>$ corresponds to the degrees of freedom that are integrated out and can be calculated separately. The second factor (the functional integral), which is related to the $\phi_<(\mathbf{k})$ modes, is the same as Eq. 2.29 except the upper integral cutoff. The next step is to reset limits of the integral by rescaling the integral parameters. This is done by defining $\mathbf{k}' = b\mathbf{k}$ which is analogous to $\mathbf{x}' = \mathbf{x}/b$ in the real space. Note that the

integral is d-dimensional, and hence $d\mathbf{k}' = b^d d\mathbf{k}$. The partition function becomes,

$$\mathcal{Z} = \mathcal{Z}_> \int \mathcal{D}\phi_<(\mathbf{k}') \exp\left[-\int_0^\Lambda \frac{d\mathbf{k}'}{(2\pi)^2} b^{-d}(r + b^{-2}Dk'^2)|\phi_<(\mathbf{k}')|^2\right]. \tag{2.32}$$

Comparing the spin correlation functions before scaling,

$$\langle\phi(\mathbf{q})\phi(\mathbf{q}')\rangle = \frac{\delta(\mathbf{q}+\mathbf{q}')}{r + Dq^2}, \tag{2.33}$$

and after scaling,

$$\langle\phi(b\mathbf{q})\phi(b\mathbf{q}')\rangle = \frac{\delta(b\mathbf{q}+b\mathbf{q}')}{r + Db^2q^2} = \frac{b^{-d}\delta(\mathbf{q}+\mathbf{q}')}{r + Db^2q^2}, \tag{2.34}$$

justifies the third step of the transformation, which is normalization of the spin function. In the vicinity of T_c, $r \to 0$ and the spin-wave function should be scaled as,

$$\phi_<(\mathbf{k}') = b^{(d+2)/2}\phi'(\mathbf{k}'). \tag{2.35}$$

Therefore, the partition function can now be expressed as,

$$\mathcal{Z} = \mathcal{Z}_> \int \mathcal{D}\phi'(\mathbf{k}') \exp\left[-\int_0^\Lambda \frac{d\mathbf{k}'}{(2\pi)^2}(b^2 r + Dk'^2)|\phi'(\mathbf{k}')|^2\right]. \tag{2.36}$$

Comparing the original partition function in Eq. 2.29 with Eq. 2.36 shows that $r' = b^2 r$ is the scaled version of r in the transformed system, at least in the Gaussian approximation.

We started with the first approximation for simplicity, but in practice higher-order terms are commonly added as perturbations, which tends to yield more complex results. For instance, by keeping the quartic term in Eq. 2.25, the partition function

becomes,

$$\mathcal{Z} = \int \mathcal{D}\phi(\mathbf{k}) e^{-(\mathcal{H}_0 + U)}, \tag{2.37}$$

where

$$\begin{aligned} \mathcal{H}_0 &= \int_0^\Lambda \frac{d\mathbf{k}}{(2\pi)^d}(r + Dk^2)|\phi^2(\mathbf{k})|, \\ U &= u \int_0^\Lambda \frac{d\mathbf{k_1}}{(2\pi)^d} ... \int_0^\Lambda \frac{d\mathbf{k_4}}{(2\pi)^d} \phi(\mathbf{k_1}) ... \phi(\mathbf{k_4}) (2\pi)^d \delta(\mathbf{k_1} + ... + \mathbf{k_4}). \end{aligned} \tag{2.38}$$

Carrying out the three steps of the RG transformation results in recursion relations for the coefficients,

$$\begin{aligned} r' &= b^2 r + 6b^2 u \int_{\Lambda/b}^\Lambda \frac{d\mathbf{k}}{(2\pi)^2} \frac{1}{r + Dk^2} = b^2 r + 6b^2 u \left(\frac{S_d \Lambda^d}{(2\pi)^d (r + D\Lambda^2)} \right) \ln(b), \\ D' &= D, \\ u' &= b^{4-d} u, \end{aligned} \tag{2.39}$$

where S_d is the surface area of a unit d-dimensional sphere. In trying to naively use these recursion relations, one immediately encounters an inconsistency: Applying them twice with, say, $b = 2$ does not yield the same result as applying them once with $b = 4$. Thus, instead of using these relations with a finite value of b, one instead solves differential equations obtained by introducing an infinitesimal renormalization parameter δl that relates to b via $b = e^{\delta l}$. With this change of variable, one writes,

$$\begin{aligned} b^2 &= e^{2\delta l} = 1 + 2\delta l + ..., \\ b^{4-d} &= e^{(4-d)\delta l} = 1 + (4-d)\delta l + ..., \end{aligned} \tag{2.40}$$

which upon substitution into Eq. 2.39 and some rearrangement yields the following

differential equations for $u(l)$ and $r(l)$,

$$\begin{aligned} u' &= b^{4-d}u = [1 + (4-d)\delta l + ...]u, \\ \lim_{\delta l \to 0}\left(\frac{u'-u}{\delta l}\right) &= \frac{du}{dl} = (4-d)u, \\ \frac{dr}{dl} &= 2r + \frac{12uS_d\Lambda^d}{(2\pi)^d(r+D\Lambda^2)}. \end{aligned} \tag{2.41}$$

These equations can be interpreted as describing the temperature change due to coarse-graining as in Eq. 2.27, or as describing the change in the exchange strength at different stages of the coarse-graining based on Eq. 2.26.

2.2.4.3 Grinstein and Koch's RG approach

Grinstein and Koch implemented the momentum shell RG approach for magnetic systems with exchange and anisotropy [21]. They reported equations governing the dependence of system properties and energetic parameters on the scaling parameter for systems of dimension $d = \epsilon + 2$. They reported success in using their proposed scaling for the exchange interactions, applied field and magnetization for a 2D system. As in momentum shell RG theory, they eliminated the spin function Fourier modes that exceed a wave vector cut-off (i.e. $\Lambda/b < |k| < \Lambda$, where $b > 1$ and represents the degree of coarse-graining) and introduced a reduced temperature, normalized with Λ and an exchange coupling $\tilde{A}$,

$$T^* = \frac{k_B T}{\tilde{A}\Lambda^{2-d}} \tag{2.42}$$

where $\tilde{A} = A$ in a 3-dimensional system. They further defined the reduced applied field and magnetocrystalline anisotropy as,

$$h = \frac{\mu_0 M_s H}{\tilde{A}\Lambda^2}, \quad g = \frac{K}{\tilde{A}\Lambda^2}. \tag{2.43}$$

Grinstein and Koch obtained the following differential equations that describe how the reduced parameters depend on the degree of coarse-graining as quantified by l, where $l = \ln(b)$,

$$\begin{aligned} \frac{dT^*(l)}{dl} &= [-\epsilon + F(T^*(l), h(l), g(l))]T^*(l), \\ \frac{dh(l)}{dl} &= 2h(l), \\ \frac{dg(l)}{dl} &= [2 - 2F(T^*(l), h(l), g(l))]g(l), \end{aligned} \tag{2.44}$$

where,

$$F(T^*, h, g) = \frac{T^*}{2\pi(1 + h + g)}. \tag{2.45}$$

The magnetization in the coarse-gained system, $M(T^*(l), h(l))$ can be related to the magnetization for the original system $M(T_0^*, h_0)$, $[T_0^* = T^*(l = 0)$, and $h_0 = h(l = 0)]$ in terms of a scaling factor ζ,

$$M(T_0^*, h_0) = \zeta(l) M(T^*(l), h(l)), \tag{2.46}$$

where,

$$\zeta(l) = e^{-\int_0^l F(T^*(l'), h(l'), g(l'))dl'}. \tag{2.47}$$

We solved the above equations numerically for our system of study ($\epsilon = 1$ for $d = 3$), for which h and g happen to be small. In this case, we obtain the following analytical expressions that can be used for scaling the exchange constant, anisotropy energy

density, field and magnetization as functions of the coarse-graining scale b,

$$\begin{aligned} A(b) &= \zeta(b) \times A_0 \\ K(b) &= \zeta(b)^3 \times K_0 \\ H(b) &= \zeta(b) \times H_0 \\ M_0 &= \zeta(b) \times M(b) \end{aligned} \tag{2.48}$$

where A_0, K_0, H_0, M_0 are the magnetic quantities for the original system ($b = 1$, $l = 0$), $\zeta(b) = t/b + 1 - t$ and $t = T/T_c$.

What the relations in Eq. 2.48 tell us can be understood from the following. Let us first assume that we carry out a simulation of our system at some temperature T with micromagnetic cell size equal to a_0, exchange constant A_0, anisotropy strength K_0 and external field H_0, and the resulting magnetization is M_0. Then, we carry out another simulation with a cell size of ba_0, with exchange constant $A(b)$, anisotropy strength $K(b)$ and external field $H(b)$, with the latter three quantities determined according to Eq. 2.48. The resulting magnetization of this simulation is $M(b)$. The last relation in Eq. 2.48 predicts how $M(b)$ and M_0 are related. Put in another way, Eq. 2.48 tells us how simulation results for $b > 1$, which are computationally less expensive because there are fewer cells in the simulation, can be used to determine properties, say $M(T, H)$, for the original system: $M(a_0, A_0, K_0; T, H_0) = \zeta(b) M[ba_0, A(b), K(b); T, H(b)]$. One important goal of this thesis is to test whether the predictions of Eq. 2.48 are valid for simulating dynamic hysteresis loops, which, in addition to being relevant to magnetic hyperthermia, is one of the main tools for characterizing magnetic materials in general.

Bibliography

[1] B. D. Cullity and C. D. Graham. *Introduction to magnetic materials*. John Wiley & Sons, 2011.

[2] R. Wood. Exact solution for a Stoner–Wohlfarth particle in an applied field and a new approximation for the energy barrier. *IEEE Trans. Magn.*, 45(1):100–103, 2009.

[3] N. A. Usov and Y. B. Grebenshchikov. Hysteresis loops of an assembly of superparamagnetic nanoparticles with uniaxial anisotropy. *J. Appl. Phys.*, 106(2): 023917, 2009.

[4] T. L. Gilbert. A phenomenological theory of damping in ferromagnetic materials. *IEEE Trans. Magn.*, 40(6):3443–3449, 2004.

[5] W. F. Brown Jr. Thermal fluctuations of a single-domain particle. *Phys. Rev.*, 130(5):1677, 1963.

[6] M. J. Donahue and D. G. Porter. *OOMMF User's Guide, Version 1.0, Interagency Report NISTIR 6376*. National Institute of Standards and Technology, Gaithersburg, MD, Sept 1999. URL `https://math.nist.gov/oommf/`.

[7] O. Lemcke. *ThetaEvolve for OOMMF release 1.2a3*, February 2004. `http://www.nanoscience.de/group_r/stm-spstm/projects/temperature/download.shtml`. See also `https://math.nist.gov/oommf/contrib/oxsext/oxsext.html`.

[8] N. A. Usov, O. N. Serebryakova, and V. P. Tarasov. Interaction effects in assembly of magnetic nanoparticles. *Nanoscale Res. Lett.*, 12(1):1–8, 2017.

[9] P. G. Bercoff and H. R. Bertorello. Exchange constants and transfer integrals of spinel ferrites. *J. Magn. Magn. Mater.*, 169(3):314–322, 1997.

[10] X. Feng and P. B. Visscher. Coarse-graining Landau–Lifshitz damping. *J. Appl. Phys.*, 89(11):6988–6990, 2001.

[11] F. Heider and W. Williams. Note on temperature dependence of exchange constant in magnetite. *Geophys. Res. Lett.*, 15(2):184–187, 1988.

[12] J. S. Kouvel. Specific heat of a magnetite crystal at liquid helium temperatures. *Phys. Rev.*, 102(6):1489, 1956.

[13] B. M. Moskowitz and S. L. Halgedahl. Theoretical temperature and grain-size dependence of domain state in x= 0.6 titanomagnetite. *J. Geophys. Res. Solid Earth*, 92(B10):10667–10682, 1987.

[14] M. L. Glasser and F. J. Milford. Spin wave spectra of magnetite. *Phys. Rev.*, 130(5):1783, 1963.

[15] C. M. Srivastava, G. Srinivasan, and N. G. Nanadikar. Exchange constants in spinel ferrites. *Phys. Rev. B*, 19(1):499, 1979.

[16] C. M. Srivastava and R. Aiyar. Spin wave stiffness constants in some ferrimagnetics. *J. Phys. C: Solid St. Phys.*, 20(8):1119, 1987.

[17] M. Uhl and B. Siberchicot. A first-principles study of exchange integrals in magnetite. *J. Phys. Condens. Matter*, 7(22):4227, 1995.

[18] S. Blundell. *Magnetism in Condensed Matter*. Oxford University Press Inc., New York, 2009.

[19] M. Kirschner, T. Schrefl, F. Dorfbauer, G. Hrkac, D. Suess, and J. Fidler. Cell size corrections for nonzero-temperature micromagnetics. *J. Appl. Phys.*, 97(10): 10E301, 2005.

[20] M. Kirschner, T. Schrefl, G. Hrkac, F. Dorfbauer, D. Suess, and J. Fidler. Relaxation times and cell size in nonzero-temperature micromagnetics. *Physica B Condens. Matter*, 372(1-2):277–281, 2006.

[21] G. Grinstein and R. H. Koch. Coarse graining in micromagnetics. *Phys. Rev. Lett.*, 90(20):207201, 2003.

[22] K. G. Wilson. Problems in physics with many scales of length. *Sci. Am.*, 241(2): 158–179, 1979.

[23] K. G. Wilson and J. Kogut. The renormalization group and the epsilon expansion. *Phys. Rep.*, 12(2):75–199, 1974.

[24] D. D. Vvedensky. Introduction to the renormalization group, course notes, chapter 3. *Imperial College, London*, 2020. Private communication.

[25] M. Kardar. *Statistical physics of fields*. Cambridge University Press, 2007.

Chapter 3

Coarse-graining in micromagnetic simulations of dynamic hysteresis loops

The contents of this chapter have been published with the following citation: R. Behbahani, M.L. Plumer, and I. Saika-Voivod, *Coarse-graining in micromagnetic simulations of dynamic hysteresis loops*, Journal of Physics: Condensed Matter **32**, 35LT01 (2020). DOI:10.1088/1361-648X/ab8c8d.

Abstract

We use micromagnetic simulations based on the stochastic Landau-Lifshitz-Gilbert equation to calculate dynamic magnetic hysteresis loops at finite temperature that are invariant with simulation cell size. As a test case, we simulate a magnetite nanorod, the building block of magnetic nanoparticles that have been employed in preclinical

studies of hyperthermia. With the goal to effectively simulate loops for large iron-oxide-based systems at relatively slow sweep rates on the order of 1 Oe/ns or less, we modify and employ a previously derived renormalization group approach for coarse-graining (Grinstein and Koch, Phys. Rev. Lett. **20**, 207201, 2003). The scaling algorithm is shown to produce nearly identical loops over several decades in the model cell volume. We also demonstrate sweep-rate scaling involving the Gilbert damping parameter that allows orders of magnitude speed-up of the loop calculations.

Keywords: Landau-Lifshitz-Gilbert equation, micromagnetics, coarse-graining, magnetic hyperthermia, nanorods

3.1 Introduction

The fundamental premise of micromagnetics is that the physics of interest can be modeled by a macrospin representing a collection of atomic spins within a small finite volume, or cell. The approximation that all spins within a cell point in the same direction is valid at temperature $T = 0$, so long as cells remain smaller than the exchange length [1]. A limiting factor for micromagnetic computer simulations is the number of cells used to model the system; using larger cells is computationally advantageous.

At finite T, a few schemes have been proposed to account for how parameters used for modelling the magnetic properties of the material must vary with cell size in order to keep system properties invariant with cell size. For example, Kirschner et al. [2, 3] suggested an approximate scaling of saturation magnetization M_{s} based on the average magnetization of blocks of spins in atomistic Monte Carlo simulations, and subsequently scaling the exchange and uniaxial anisotropy constants A and K

to preserve the exchange length and anisotropy field. Feng and Visscher [4] proposed that the damping parameter α, which models the dynamics of magnetic energy loss [5], should scale with cell size, arguing that using larger cells is analogous to having more degrees of freedom for energy absorption; see also [6] for efforts related to α. The renormalization group (RG) approach of Grinstein and Koch [7], based on mapping a Fourier space analysis of the non-linear sigma model to ferromagnets in order to scale A, K, field H and magnetization M, has garnered significant attention. However, to the best of our knowledge, no scaling theory has been applied to the calculation of magnetization-field (MH) hysteresis loops [8], which are the foundation of experimental characterization of magnetic systems.

In this Letter, we modify and employ the approach proposed by Grinstein and Koch [7] to the test case of calculating MH loops for magnetite nanorods at sweep rates relevant to magnetic hyperthermia, allowing us to make estimates of specific loss power that would otherwise be computationally impractical.

3.2 The model

The magnetite nanorods we simulate are the building-blocks of the nanoparticles that were shown by Dennis et al. to successfully treat cancerous tumours in mice via hyperthermia [10]. It is reasonable to choose the smallest micromagnetic cell to be the cubic unit cell, which is of length $a_0 = 0.839$ nm and contains 24 magnetic Fe ions. We set the exchange stiffness constant to $A_0 = 0.98 \times 10^{-11}$ J/m, which for cell length a_0 yields an effective exchange constant between neighbouring cells of $J_{\text{eff}} = a_0 A_0 = 8.222 \times 10^{-21}$ J, which in turn yields a bulk critical temperature of $T_c = 1.44 J_{\text{eff}}/k_B = 858$ K for the bulk 3D-Heisenberg-model version of our system.

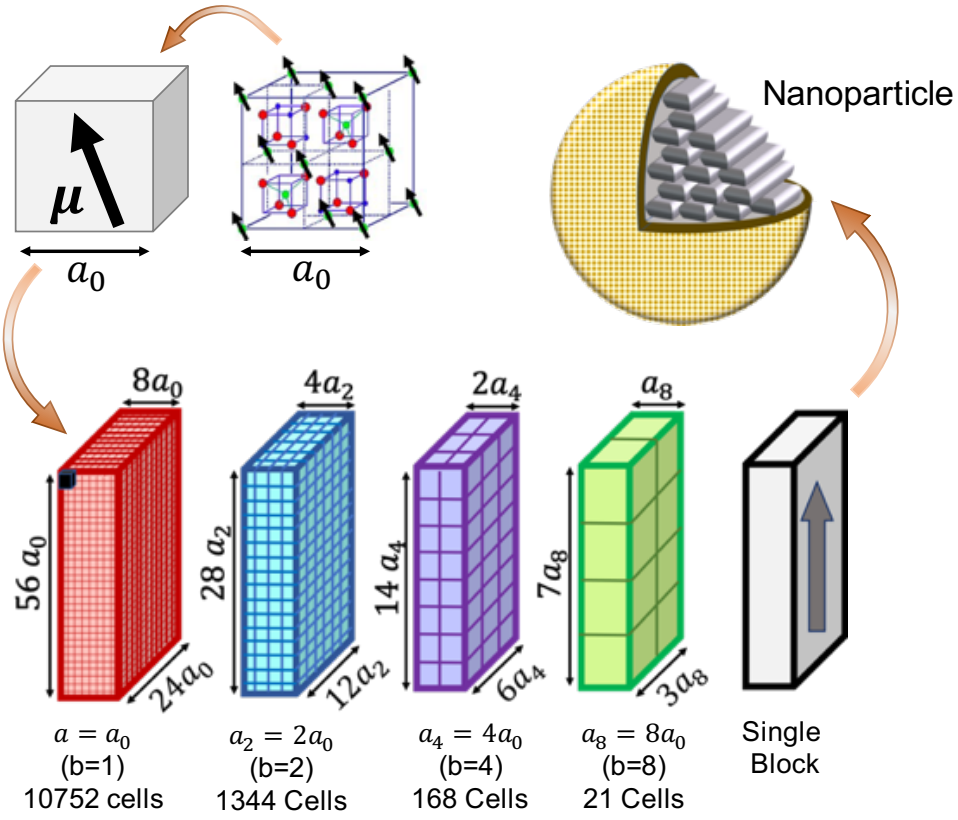

Figure 3.1: Coarse-grained modelling of a magnetite nanorod. The smallest micromagnetic cell models the atomic spins within a cubic unit cell of length $a_0 = 0.839$ nm with a single magnetic moment. Our goal is to model the system using a smaller number of larger cells (of length $a_b = b\,a_0$ for $b > 1$) with appropriately scaled parameters. The number of cells drawn and their sizes are only approximate. Illustrative spins for half of the tetrahedral Fe^{3+} sites (FCC sites) are drawn over a spinel unit cell taken from Ref. [9].

This value of A_0 is close to what can be theoretically determined by considering the atomic-level exchange interactions across the faces of neighbouring unit cells [11], and is in reasonable agreement with experimental values [12–18]. The nanorod dimensions are approximately 6.7 nm × 20 nm × 47 nm ($8a_0 \times 24a_0 \times 56a_0$), with its length along the z-axis. We set $M_s = 480$ kA/m [12, 19, 20], the bulk value for magnetite. We do not consider magnetostatic interactions explicitly, but rather implicitly through an effective uniaxial anisotropy. For the purposes of this study, we choose a strength

of $K_0 = 10$ kJ/m^3, which is consistent with other studies of iron oxide nanoparticles [21, 22], and for which a more precise estimate can be obtained by considering the nanorod's demagnetization tensor [20, 23–27], maghemite content [10], and the effect of neighbouring nanorods within a nanoparticle. We omit cubic crystalline anisotropy as it has negligible effects on the hysteresis loops of magnetite nanoparticles with even modest aspect ratios, as discussed in Refs. [20, 27] (we have also verified that adding cubic anisotropy of strength 10 kJ/m^3 has no impact on the loops presented here). Anisotropy is set along the z-axis with a 5° dispersion to mimic lattice disorder [22]. For convenience we set $\alpha = 0.1$, a choice consistent with previous studies [22, 28] and with magnetite thin films [29].

While hysteretic heating is at the heart of magnetic nanoparticle hyperthermia, preventing eddy current heating of healthy tissue limits the frequency f and amplitude $H_{\max}$ of the external field such that the sweep rate $\mathrm{SR} = 4H_{\max}f$ is less than a target value of 0.25 Oe/ns [19, 30]. For our simulation, we set $H_{\max} = 500$ Oe, which for the target SR implies a target value of $f = 125$ kHz, a value large enough to restrict unwanted Brownian relaxation [19].

To model the dynamics of the magnetization of a cell $\mathbf{M}$ of fixed magnitude M_{s}, we solve the Landau-Lifshitz-Gilbert (LLG) equation [5, 23, 31],

$$\frac{d\mathbf{M}}{dt} = -\gamma_1 \mathbf{M} \times \mathbf{H}_{\mathrm{eff}} - \frac{\alpha\gamma_1}{\mathrm{M}_s}\mathbf{M} \times (\mathbf{M} \times \mathbf{H}_{\mathrm{eff}}) \tag{3.1}$$

where t is time, $\gamma_1 = \mu_0\gamma_e/(1+\alpha^2)$, $\gamma_e = 1.76 \times 10^{11}$ rad/(s.T) is the gyromagnetic ratio for an electron, μ_0 is the vacuum permeability, and $\mathbf{H}_{\mathrm{eff}}$ is due to the combination of an external field, uniaxial anisotropy, exchange interactions and a thermal field. We perform our simulations using OOMMF (Object Oriented Micromagnetic Framework) software [32]. In particular, we include the Theta Evolve module [33]

used for simulations at finite T via a stochastic thermal field [31].

We simulate the rod using cubic cells of length ba_0, with b taking on values 1, 2, 4 and 8. See Fig. 3.1. For $b = 1$, 10752 cells make up the rod. For $b = 2$, there are $10752/2^3 = 1344$ cells. The volume of the rod is fixed for all simulations at $10752a_0^3 \approx (22a_0)^3$. Additionally, we simulate the rod as a single cell – a single rectangular prism, or block. While there is some ambiguity in assigning a single length scale to represent a rectangular prism, we choose $b = 22$ from the geometrical mean, i.e., the side length of the cube of the same volume as the rod.

3.3 Coarse-graining

The goal of coarse-graining is to determine $A(b)$ and $K(b)$, i.e., how the exchange and anisotropy parameters should change with b to keep system properties invariant with b. The $b = 22$ case is a practical limit where all the atomic spins are represented by a single macrospin, where exchange interactions are no longer required in the simulations, and which provides for an interesting test of a coarse-graining procedure in predicting $K(b)$. In calculating hysteresis loops for a system with cell length ba_0, we apply an external field along the z axis of $H(b) = H_{\max} \sin(2\pi f t)$, and report the z-component of the average (over cells) magnetization unit vector $m_H = \bar{M}_z/M_s$, averaged over 88 to 100 independent simulations for $b > 1$. For $b = 1$ we use 250 simulations.

In Fig. 3.2a we plot hysteresis loops at $T = 310$ K using different cell sizes (varying b) while keeping the exchange and anisotropy parameters fixed at A_0 and K_0. A value of SR = 2.5 Oe/ns is chosen to make the simulations computationally feasible at $b = 1$. Both the coercivity H_c and the remanence increase with increasing b. The increasing

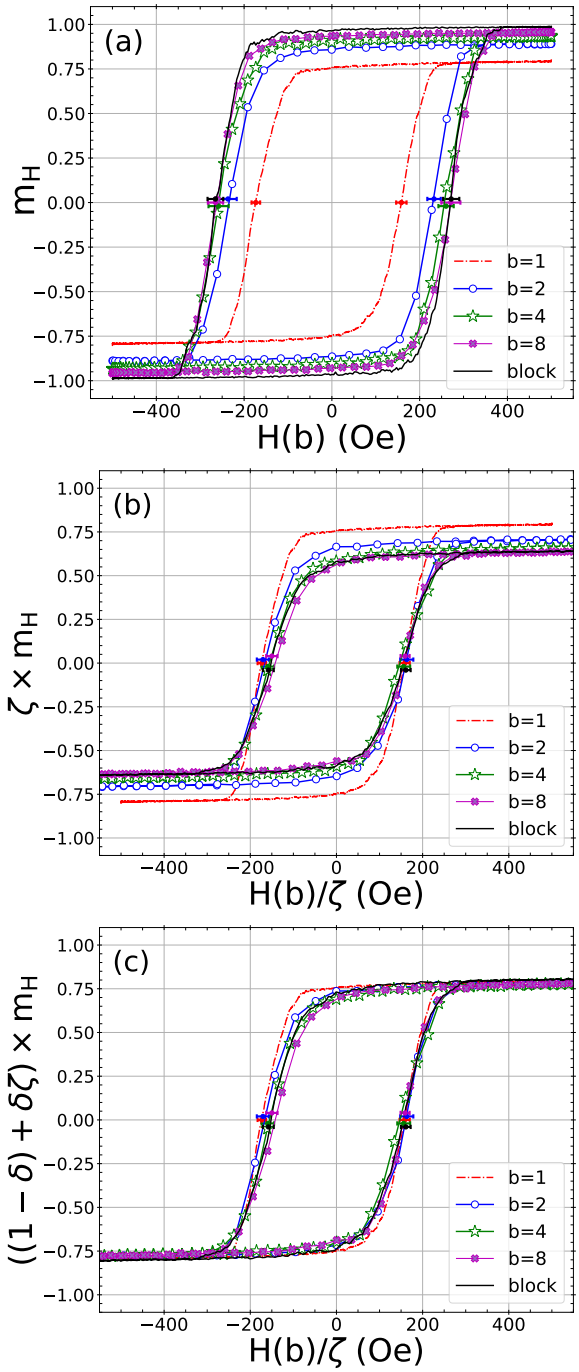

Figure 3.2: Application of RG coarse graining to nanorod MH loops at $T = 310$ K and SR = 2.5 Oe/ns. (a) Changing cell length ($a = ba_0$) without changing magnetic parameters. (b) A and K are scaled according to Eqs. 3.8 and 3.9, respectively, and m_H and H are scaled according to Eqs. 3.11 and 3.10, respectively. (c) As in panel (b), except m_H is scaled according to Eq. 3.13 with $\delta = 0.511$. $\Delta t = 1$ fs for all simulations. Horizontal error bars shown for H_c represent one standard error and are vertically displaced to avoid overlap. Uncertainty in H_c is approximately 7 to 13%.

loop area is consistent with the stronger exchange coupling ($J_{\text{eff}} = ba_0A_0$) between magnetization vectors of adjacent cells. For $b \geq 4$, it appears that the exchange is strong enough for the system to be nearly uniformly magnetized, and so H_c remains largely unchanged for $b \geq 4$ since K is constant. This means that for $b = 1$, at this T and for our rod size, exchange is not strong enough to be able to treat the nanorod as a single macrospin in a trivial way. Clearly, varying cell size changes the loops and a coarse-graining procedure is required.

In their coarse-graining procedure, Grinstein and Koch introduced a reduced temperature T^*, which for a three dimensional system is given by,

$$T^* = \frac{k_B T \Lambda}{A}. \tag{3.2}$$

where $\Lambda = 2\pi/ba_0$ is a high wave-number cut-off that reflects the level of coarse-graining. Similarly, the reduced parameters for field and anisotropy constants are defined as,

$$h = \frac{\mu_0 M_s H}{A\Lambda^2}\frac{1000}{4\pi}, \qquad g = \frac{K}{A\Lambda^2}, \tag{3.3}$$

with H given in Oe. Introducing the parameter $l = \ln(b)$, they gave the following set of equations for calculating the reduced parameters as functions of cell size,

$$\begin{aligned}
\frac{dT^*(l)}{dl} &= \left[-1 + F\left(T^*(l), h(l), g(l)\right)\right] T^*(l) \\
\frac{dh(l)}{dl} &= 2h(l) \\
\frac{dg(l)}{dl} &= \left[2 - 2F\left(T^*(l), h(l), g(l)\right)\right] g(l)
\end{aligned} \tag{3.4}$$

where

$$F(T^*, h, g) = \frac{T^*}{2\pi(1 + h + g)}. \tag{3.5}$$

Additionally, the magnetization of the coarse-grained system is scaled via,

$$M(T^*, h) = \zeta(l) \times M(T^*(l), h(l)) \tag{3.6}$$

where

$$\zeta(l) = e^{-\int_0^l F(T^*(l'), h(l'), g(l'))dl'}. \tag{3.7}$$

For our system parameters and range of H, both $g \ll 1$ and $h \ll 1$, and so $F \simeq T/2\pi$, which makes the numerical solution of Eq. 3.4 practically indistinguishable from the approximate analytic solution, which we find to be,

$$A(b) = \zeta(b) \times A_0 \tag{3.8}$$

$$K(b) = \zeta(b)^3 \times K_0 \tag{3.9}$$

$$H(b) = \zeta(b) \times H_0 \tag{3.10}$$

$$M_0 = \zeta(b) \times M(b) \tag{3.11}$$

where $t = T/T_c$ and $\zeta(b) = t/b + 1 - t$. At $T = 310$ K, $t = 0.3613$, $\zeta(2) = 0.8193$, $\zeta(4) = 0.7290$, $\zeta(8) = 0.6839$, and $\zeta(22) = 0.6551$.

Eqs. 3.8 and 3.9 provide a prescription for changing material parameters with b, while Eqs. 3.10 and 3.11 provide the prescription for scaling H and M after a loop calculation. However, we find that the prescription does not yield loops that are invariant with b, on account of Eq. 3.11; the correction of the coarse-grained values of M back to those corresponding to the unscaled system is too large (the corrected remanance is too small), as we show in Fig. 3.2b. In Fig. 3.2c, we apply a correction to Eq. 3.11 and obtain good agreement between the reference ($b = 1$) and coarse-grained ($b > 1$) loops.

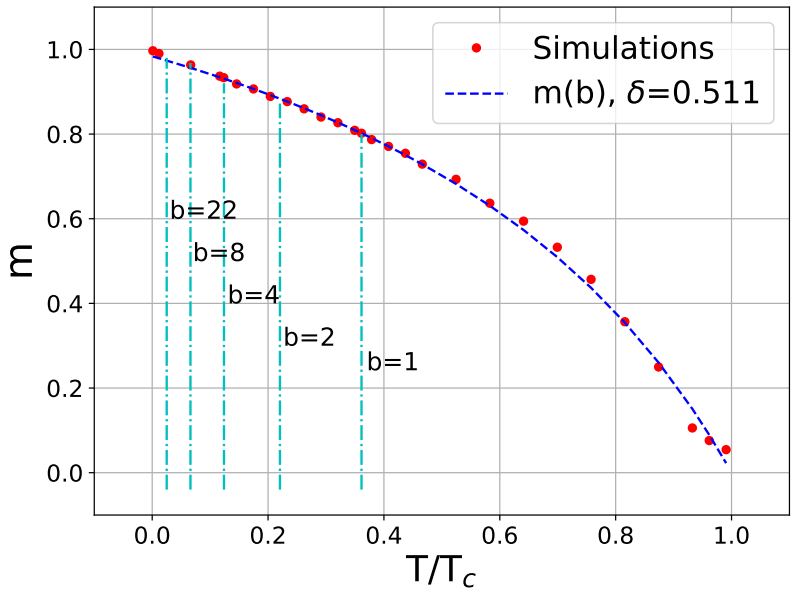

Figure 3.3: Determining a scaling function for $M(b)$ from the T dependence of the nanorod magnetization. δ is used as a fitting parameter to match nanorod data, yielding a value of 0.511. Vertical dot-dash lines indicate reduced temperatures corresponding to different values of b.

To motivate our correction to the rescaling of the magnetization, we begin by noting that the same value of T^* in Eq. 3.2 can be achieved by either having a rescaled temperature $T(b)$ or having a rescaled $A(b)$. Combining this idea with Eq. 3.8 yields,

$$T(b) = \frac{T_0}{b\zeta(b, T_0)}, \tag{3.12}$$

which together with Eq. 3.11 [after solving for $M(b)$] predicts an overly simple dependence of M on T, parametrically through b: a line passing through M_0 and T_0 at $b = 1$ and through $M = 0$ and $T = T_c$ as $b \to 0$.

To obtain a model that better matches the data, we introduce a phenomenolgical correction to Eq. 3.11, one in which M_0 is a weighted average of $M(b)$ and the RG expression for M_0,

$$M_0 = \delta\zeta(b, T_0)M(b) + (1 - \delta)M(b). \tag{3.13}$$

We use δ as a free parameter to fit the $M(T)$ data for the nanorod. This yields a value of $\delta = 0.511$, which we use in rescaling m_H in Fig. 3.2c. The fit reasonably recovers $M(T)$ in the T range corresponding to values of b between 1 and 22, as shown in Fig. 3.3.

The collapse of the data in Fig. 3.2c is remarkable, with the biggest discrepancy arising between $b = 1$, corresponding to the most fine-grained simulation, and $b = 2$, the first step in coarse-graining. The difference lies most noticeably in the shoulder region where the phase transition starts and magnetization begins to change. The process likely occurs on a length scale smaller than a_b and hence the microscopic details likely matter most. Loss of some detail is expected with coarse-graining and consistent with previous studies involving atomic-level magnetization switching in a grain [34]. The magnetization in the shoulder areas appears to diminish with increasing b. The behavior of $b = 22$ runs counter to this trend, but at this level of coarse-graining, there is only a single cell. It is significant, however, that scaling seems to hold even in this limit. (We note that in this limit, even though there are no exchange interactions in the simulations, the value of the effective anisotropy still depends on exchange through the dependence of T_c on A_0.) The loop areas for $b = 1$, 2 , 4, 8 and 22 are 495, 488, 443, 432 and 472 Oe, respectively. The smallest loop area (for $b = 8$) is 13% smaller than the area for $b = 1$.

We note that the unrenormalized exchange length for our simulated material is $l_{\mathrm{ex},0} = \sqrt{\frac{2A_0}{\mu_0 M_s^2}} = 8.23$ nm, which is longer than $a_8 = 6.712$ nm, and so only our $b = 22$ single block simulations scale the cell size beyond $l_{\mathrm{ex},0}$. Under renormalization, however, the exchange length becomes $l_{\mathrm{ex,b}} = \sqrt{\frac{2\zeta(b)A_0}{\mu_0 M_s^2}}$, which decreases with increasing b, and takes on values 7.45, 7.02, 6.80 and 6.66 nm for $b = 2, 4, 8$, and 22, respectively. Thus for $b = 8$, the cell length and the exchange length are approximately

the same. It is expected that coarse-graining should be valid for $a_b < l_{\rm ex}$ [1], i.e., for $b \lesssim 8$. However, the nanorods are in the single-domain regime and this is perhaps why $b = 22$ yields reasonable results, notwithstanding the trend that loop area decreases with increasing b.

3.4 SR/α scaling

We now turn our attention to speeding up simulations by considering the relationship between SR and α. A larger value of α signifies a faster loss of energy and a shorter relaxation time for alignment of the magnetic moments to the field, and results in a smaller hysteresis loop. Likewise, a slower SR is equivalent to a longer measurement time and consequently a smaller hysteresis loop. To build on these ideas, we recall Sharrock's equation for H_c as a function of T [35],

$$H_c = H_K \left[1 - \sqrt{\frac{k_B T}{KV} \ln\left(\frac{f_0 \tau}{\ln 2}\right)} \right]. \tag{3.14}$$

Sharrock derived this equation by calculating the time required for half of the magnetization vectors in the system, which are initially anti-aligned with the field, to overcome an energy barrier that grows with KV and align with a field of strength H_c. In this context, τ is the relaxation time. In the context of hysteresis loops, H_c is the field required to flip half of the magentization vectors in an observation time τ, which is related to SR via $\tau \propto 1/\text{SR}$. f_0 is the so-called attempt frequency, for which Brown [31, 36–39] derived an expression in the high-barrier limit. At small α, $f_0 \propto \alpha$, and so the product $f_0\tau \propto \alpha/\text{SR}$, implying that so long as SR/α = constant, H_c should remain the same.

In Fig. 3.4 we show loops calculated for SR/$\alpha = 2.5$ ($H_{\rm max} = 500$ Oe, and $f =$

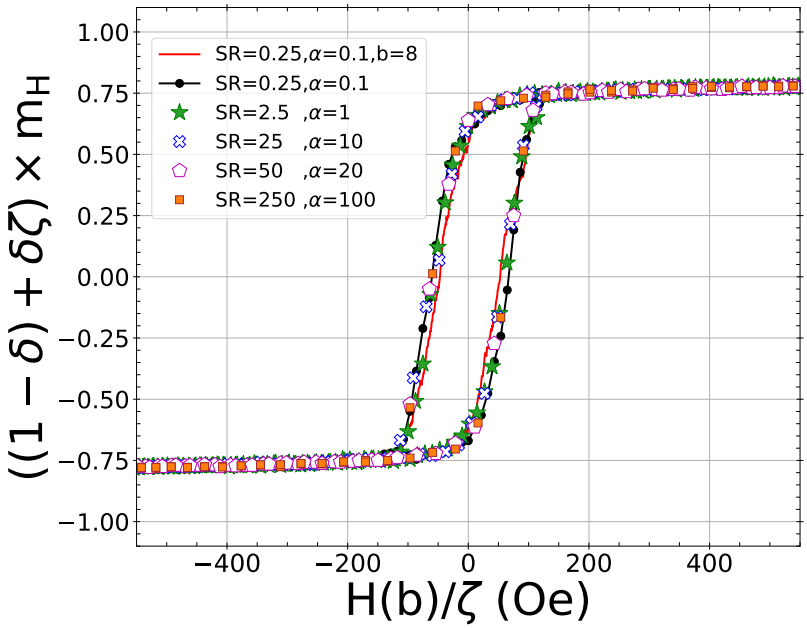

Figure 3.4: Invariance of MH loops. We combine RG scaling of magnetic quantities, larger time step with block size, and SR/α scaling to predict the behaviour of prohibitively long fine-grain ($b = 1$) simulations. $b = 4$ unless otherwise noted.

125 kHz), the ratio obtained using a clinically relevant SR = 0.25 Oe/ns and the estimate of $\alpha = 0.1$. Data for $b = 4$ and 8 and for various SR-α pairs show good agreement. At 0.25 Oe/ns, simulations using $b = 1$ are prohibitively long, taking several months on available computing resources. The results shown here combine the RG approach to reduce the number of cells, the ability to use a larger time step Δt for larger cells in solving the LLG equation [6], and the SR/α scaling to employ a faster SR, all to dramatically reduce simulation time – by a factor of 4^3 to 8^3 for reducing the number of cells, a factor of at least 5 for the time step, and a factor of up to 1000 when using the fastest SR. The average area of the five loops for $b = 4$ in Fig. 3.4 is $S = 171.3 \pm 2.8$ Oe, translating to a specific loss power of $f\mu_0 \frac{1000}{4\pi} M_s S/\rho = 207$ W/g $\pm 10\%$ (using $\rho = 5.17$ g/cm^3), which is consistent with clinical expectations [40]. The loop area for $b = 8$ is 13% lower at 149.4 Oe.

3.5 Conclusions

In summary, we show that our modification to the RG approach of Grinstein and Koch [7] yields a scaling of exchange and anisotropy parameters and finite temperature nanorod hysteresis loops that are, to approximately $10\%-15\%$, invariant with cell size. We note that the coarse-graining of magnetostatic interactions is beyond the framework of Ref. [7]. We are currently investigating magnetostatic scaling, and intend to report on it in future work.

Scaling results hold even to the point where the nanorod is represented by a single magnetization vector that experiences anisotropy only. Whether this limit holds for systems with weaker exchange remains to be studied. This reduction to an effective Stoner-Wohlfarth (SW) model [41] should facilitate comparison with experiments on nanorods, since an analytic solution to the SW model at finite T and SR exists [28]. It should also simplify computational studies of nanoparticles (nanorod composites) and collections of nanoparticles used in a wide variety of applications and hence facilitate comparison with experimental MH loops and quantification of system properties through simulations.

In addition to the computational speedup resulting from the use of fewer micromagnetic cells, the invariance of loops when SR/α is fixed provides another avenue for computational speedup by allowing one to use a larger SR than the target value. We caution, however, that the theoretical motivation for this invariance stems from considering the Sharrock equation for only small α. While both SR and α set time scales, we have not provided any reasoning for why the invariance should hold as well as it does for larger α.

The data that support the findings of this study are available from the corresponding author upon reasonable request.

Acknowledgments

We thank Johan van Lierop, Rachel Nickel and Mikko Karttunen for enlightening discussions, and Martin D. Leblanc for guidance in using OOMMF. R.B. and I.S.-V. thank Mikko Karttunen and Styliani Consta for hosting our stay at Western University. We acknowledge the financial support from the Natural Sciences and Engineering Research Council (Canada). Computational resources were provided by ACENET and Compute Canada.

Bibliography

[1] G. S. Abo, Y.-K. Hong, J. Park, J. Lee, W. Lee, and B.-C. Choi. Definition of magnetic exchange length. *IEEE Trans. Magn.*, 49(8):4937–4939, 2013.

[2] M. Kirschner, T. Schrefl, G. Hrkac, F. Dorfbauer, D. Suess, and J. Fidler. Relaxation times and cell size in nonzero-temperature micromagnetics. *Physica B Condens. Matter*, 372(1-2):277–281, 2006.

[3] M. Kirschner, T. Schrefl, F. Dorfbauer, G. Hrkac, D. Suess, and J. Fidler. Cell size corrections for nonzero-temperature micromagnetics. *J. Appl. Phys.*, 97(10): 10E301, 2005.

[4] X. Feng and P. B. Visscher. Coarse-graining Landau–Lifshitz damping. *J. Appl. Phys.*, 89(11):6988–6990, 2001.

[5] T. L. Gilbert. A phenomenological theory of damping in ferromagnetic materials. *IEEE Trans. Magn.*, 40(6):3443–3449, 2004.

[6] X. Wang, K. Gao, and M. Seigler. Magnetization dynamics coarse graining through Landau-Lifshitz-Gilbert equation renormalization. *IEEE Trans. Magn.*, 47(10):2676–2679, 2011.

[7] G. Grinstein and R. H. Koch. Coarse graining in micromagnetics. *Phys. Rev. Lett.*, 90(20):207201, 2003.

[8] S. C. Westmoreland, R. F. L. Evans, G. Hrkac, T. Schrefl, G. T. Zimanyi, M. Winklhofer, N. Sakuma, M. Yano, A. Kato, T. Shoji, A. Manabe, M. Ito, and R. W. Chantrell. Reprint of multiscale model approaches to the design of advanced permanent magnets. *Scripta Materialia*, 154:266–272, 2018.

[9] *Introduction to Inorganic Chemistry*, chapter 8.6,. Wikibooks, 2019. URL `https://en.wikibooks.org/wiki/Introduction_to_Inorganic_Chemistry`. see Creative Commons licence http://creativecommons.org/licenses/by-nc-sa/3.0/us/.

[10] C. L. Dennis, A. J. Jackson, J. A. Borchers, P. J. Hoopes, R. Strawbridge, A. R.

Foreman, J. Van Lierop, C. Grüttner, and R. Ivkov. Nearly complete regression of tumors via collective behavior of magnetic nanoparticles in hyperthermia. *Nanotechnology*, 20(39):395103, 2009.

[11] R. H. Victora, S. D. Willoughby, J. M. MacLaren, and J. Xue. Effects of grain boundaries on magnetic properties of recording media. *IEEE Trans. Magn.*, 39 (2):710–715, 2003.

[12] F. Heider and W. Williams. Note on temperature dependence of exchange constant in magnetite. *Geophys. Res. Lett.*, 15(2):184–187, 1988.

[13] J. S. Kouvel. Specific heat of a magnetite crystal at liquid helium temperatures. *Phys. Rev.*, 102(6):1489, 1956.

[14] B. M. Moskowitz and S. L. Halgedahl. Theoretical temperature and grain-size dependence of domain state in x= 0.6 titanomagnetite. *J. Geophys. Res. Solid Earth*, 92(B10):10667–10682, 1987.

[15] M. L. Glasser and F. J. Milford. Spin wave spectra of magnetite. *Phys. Rev.*, 130(5):1783, 1963.

[16] C. M. Srivastava, G. Srinivasan, and N. G. Nanadikar. Exchange constants in spinel ferrites. *Phys. Rev. B*, 19(1):499, 1979.

[17] C. M. Srivastava and R. Aiyar. Spin wave stiffness constants in some ferrimagnetics. *J. Phys. C: Solid St. Phys.*, 20(8):1119, 1987.

[18] M. Uhl and B. Siberchicot. A first-principles study of exchange integrals in magnetite. *J. Phys. Condens. Matter*, 7(22):4227, 1995.

[19] S. Dutz and R. Hergt. Magnetic nanoparticle heating and heat transfer on a microscale: basic principles, realities and physical limitations of hyperthermia for tumour therapy. *Int. J. Hyperth.*, 29(8):790–800, 2013.

[20] N. A. Usov, S. A. Gudoshnikov, O. N. Serebryakova, M. L. Fdez-Gubieda, A. Muela, and J. M. Barandiarán. Properties of dense assemblies of magnetic nanoparticles promising for application in biomedicine. *J. Supercond. Nov. Magn.*, 26(4):1079–1083, 2013.

[21] N. A. Usov, O. N. Serebryakova, and V. P. Tarasov. Interaction effects in assembly of magnetic nanoparticles. *Nanoscale Res. Lett.*, 12(1):1–8, 2017.

[22] M. L. Plumer, J. van Lierop, B. W. Southern, and J. P. Whitehead. Micromagnetic simulations of interacting dipoles on an fcc lattice: application to nanoparticle assemblies. *J. Phys. Condens. Matter*, 22(29):296007, 2010.

[23] B. D. Cullity and C. D. Graham. *Introduction to magnetic materials*. John Wiley

& Sons, 2011.

[24] A. J. Newell, W. Williams, and D. J. Dunlop. A generalization of the demagnetizing tensor for nonuniform magnetization. *J. Geophys. Res. Solid Earth*, 98 (B6):9551–9555, 1993.

[25] A. Aharoni. Demagnetizing factors for rectangular ferromagnetic prisms. *J. Appl. Phys.*, 83(6):3432–3434, 1998.

[26] H. Fukushima, Y. Nakatani, and N. Hayashi. Volume average demagnetizing tensor of rectangular prisms. *IEEE Trans. Magn.*, 34(1):193–198, 1998.

[27] N. A. Usov and J. M. Barandiarán. Magnetic nanoparticles with combined anisotropy. *J. Appl. Phys.*, 112(5):053915, 2012.

[28] N. A. Usov. Low frequency hysteresis loops of superparamagnetic nanoparticles with uniaxial anisotropy. *J. Appl. Phys.*, 107(12):123909, 2010.

[29] S. Serrano-Guisan, H.-C. Wu, C. Boothman, M. Abid, B. S. Chun, I. V. Shvets, and H. W. Schumacher. Thickness dependence of the effective damping in epitaxial Fe_3O_4/MgO thin films. *J. Appl. Phys.*, 109(1):013907, 2011.

[30] R. Hergt and S. Dutz. Magnetic particle hyperthermia—biophysical limitations of a visionary tumour therapy. *J. Magn. Magn. Mater.*, 311(1):187–192, 2007.

[31] W. F. Brown Jr. Thermal fluctuations of a single-domain particle. *Phys. Rev.*, 130(5):1677, 1963.

[32] M. J. Donahue and D. G. Porter. *OOMMF User's Guide, Version 1.0, Interagency Report NISTIR 6376*. National Institute of Standards and Technology, Gaithersburg, MD, Sept 1999. URL `https://math.nist.gov/oommf/`.

[33] O. Lemcke. *ThetaEvolve for OOMMF release 1.2a3*, February 2004. `http://www.nanoscience.de/group_r/stm-spstm/projects/temperature/download.shtml`. See also `https://math.nist.gov/oommf/contrib/oxsext/oxsext.html`.

[34] J. I. Mercer, M. L. Plumer, J. P. Whitehead, and J. Van Ek. Atomic level micromagnetic model of recording media switching at elevated temperatures. *Appl. Phys. Lett.*, 98(19):192508, 2011.

[35] M. Sharrock and J. McKinney. Kinetic effects in coercivity measurements. *IEEE Trans. Magn.*, 17(6):3020–3022, 1981.

[36] J. L. García-Palacios and F. J. Lázaro. Langevin-dynamics study of the dynamical properties of small magnetic particles. *Phys. Rev. B*, 58(22):14937, 1998.

[37] L. Breth, D. Suess, C. Vogler, B. Bergmair, M. Fuger, R. Heer, and H. Brueckl. Thermal switching field distribution of a single domain particle for field-dependent attempt frequency. *J. Appl. Phys.*, 112(2):023903, 2012.

[38] T. Taniguchi and H. Imamura. Thermal switching rate of a ferromagnetic material with uniaxial anisotropy. *Phys. Rev. B*, 85(18):184403, 2012.

[39] J. Leliaert, A. Vansteenkiste, A. Coene, L. Dupré, and B. Van Waeyenberge. Vinamax: a macrospin simulation tool for magnetic nanoparticles. *Med. Biol. Eng. Comput.*, 53(4):309–317, 2015.

[40] P. Das, M. Colombo, and D. Prosperi. Recent advances in magnetic fluid hyperthermia for cancer therapy. *Colloids Surf. B*, 174:42–55, 2019.

[41] E. C. Stoner and E. P. Wohlfarth. A mechanism of magnetic hysteresis in heterogeneous alloys. *Philos. Trans. Royal Soc. A*, 240(826):599–642, 1948.

Chapter 4

Multiscale modelling of magnetostatic effects on magnetic nanoparticles with application to hyperthermia

The contents of this chapter have been published with the following citation: R. Behbahani, M.L. Plumer, and I. Saika-Voivod, *Multiscale modelling of magnetostatic effects on magnetic nanoparticles with application to hyperthermia*, Journal of Physics: Condensed Matter **33**, 215801 (2021). DOI:10.1088/1361-648X/abe649.

Abstract

We extend a renormalization group-based (RG) coarse-graining method for micromagnetic simulations to include properly scaled magnetostatic interactions. We apply the

method in simulations of dynamic hysteresis loops at clinically relevant sweep rates and at 310 K of iron oxide nanoparticles (NPs) of the kind that have been used in preclinical studies of magnetic hyperthermia. The coarse-graining method, along with a time scaling involving sweep rate and Gilbert damping parameter, allow us to span length scales from the unit cell to NPs approximately 50 nm in diameter with reasonable simulation times. For both NPs and the nanorods composing them, we report effective uniaxial anisotropy strengths and saturation magnetizations, which differ from those of the bulk materials magnetite and maghemite of which they are made, on account of the combined non-trivial effects of temperature, inter-rod exchange, magnetostatic interactions and the degree of orientational order within the nanorod composites. The effective parameters allow treating the NPs as single macrospins, and we find for the test case of calculating loops for two aligned NPs that using the dipole approximation is sufficient for distances beyond 1.5 times the NP diameter. We also present a study on relating integration time step to micromagnetic cell size, finding that the optimal time step size scales approximately linearly with cell volume.

Keywords: magnetostatics, Landau-Lifshitz-Gilbert equation, micromagnetics, coarse-graining, magnetic hyperthermia

4.1 Introduction

The use of micromagnetics based on the Landau-Lifshitz-Gilbert (LLG) equations for the simulation of dynamic hysteretic magnetization-magnetic field (MH) loops at room temperature and at kHz frequencies relevant for magnetic hyperthermia applications offers a challenging area of the study for coarse graining. For numerical studies based on micromagnetics, hysteretic heating is typically associated with the specific loss

power (SLP) and is assumed to be proportional to the area of a calculated MH loop. In a recent work [1] (hereafter referred to as I), we employed and modified a renormalization group (RG) approach introduced by Grinstein and Koch [2] for our model system of magnetite (Fe_3O_4) nanorods that form the building blocks of nanoparticles used in preclinical magnetic hyperthermia trials on mice [3]. Our study focused on MH loops and demonstrated that for the case of individual nanorods, where exchange interactions, uniaxial anisotropy, and a sinusoidal external field are included in the model of uniformly magnetized cells, the RG approach works well over an entire range of fixed-volume rods composed of from 10752 cells ($b = 1$) to one cell ($b = 22$), where the smallest cell size of the scaling parameter $b = 1$ corresponds to the dimensions of the magnetite unit cell. Our work also illustrates that significant additional computational speed-up can be achieved over the dynamic range of interest by maintaining a constant value for SR/α, where SR is the designated sweep rate (in units of Oe/s) of the MH loop simulation and α is the LLG damping constant. This work, which employed the Object Oriented MicroMagnetic Framework (OOMMF) micromagnetics software [4], omitted explicit magnetostatic interactions but these were accounted for through an effective uniaxial anisotropy.

Here, our previous work is extended with several objectives. The first is to develop a coarse-graining algorithm for dynamic MH loops for a single nanorod that has explicit magnetostatic interactions included (in addition to the scaling of the magnetization, exchange, anisotropy and applied field used previously), which were mentioned only briefly in the RG analysis of Grinstein and Koch [2]. This study allows for the estimation of an effective single-ion anisotropy that mimics the effects of the self-demag field. The second goal is to examine MH loops corresponding to magnetic nanoparticles (NPs) that are constructed from the nanorods, where inter-rod exchange and inter-rod magnetostatic interactions are important. This part of the study examines

the case of just two adjacent nanorods in various geometries (appendix 4.B), as well as composites of 10 stacked nanorods, inspired by the experimental study of Dennis et al. [3]. Different stackings represent varying degrees of orientational order of nanorods within a NP. Loops corresponding to a variety of applied field orientations are examined. The third goal is to find the effective magnetization and anisotropy that allows the modelling of a NP as a single macrospin, both in the case of a single NP in a field and for two interacting NPs. This macrospin approximation may be useful for further study of NP assemblies. In addition, the impact of cell size on the assigned time step in the OOMMF LLG solver is studied, where a larger time step can be used with larger cell sizes resulting in an additional increase in computational efficiency.

Magnetic hyperthermia as a novel and developing cancer treatment method continues to attract considerable attention at the applied as well as fundamental level [5–10]. A wide range of preclinical studies have been reported using magnetic hyperthermia as a primary or secondary cancer treatment along with conventional chemotherapy or radiotherapy [3, 11–13]. Moreover, recent analytical and numerical studies [8, 14–19] reflect the growing need for understanding the heating mechanisms of magnetic hyperthermia to provide a more accurate guide for experiments.

In magnetic hyperthermia, injected magnetic nanoparticles exhibit hysteresis under applied magnetic field and heat up and damage cancerous tumor cells. As nanoparticles are mobile inside the tumor upon injection, exploring the effects of interactions between magnetic particles, as well as possible heating mechanisms such as Brownian rotation or hysteresis heating (Néel relaxation), is crucial for understanding particle clustering and heating efficiency. To this end, many studies have investigated the impact of long range dipolar interactions on hyperthermia with interesting and related results [8, 16, 18, 20–23]. For example, Anand et al. [16] examined the effect

of dipole interaction strength on the heating efficiency of micron-sized particles and showed that there is an optimal NP volume fraction for maximizing SLP. Haase and Nowak [21] reported a negative effect of dipolar interactions on SLP at high particle concentrations. By contrast, Landi [20] used a mean field theory and found that the dipole interactions increase the energy barrier between stable configurations of the magnetization. He deduced that dipolar interactions improve SLP as long as certain conditions of the energy barrier of the system are met. Such studies motivate a bottom-up approach to determining and modeling effective interparticle interactions, and underline the importance of including magnetostatic interactions in our scaling approach.

This paper is organized as follow. Our model is described in section 4.2. Section 4.3 summarizes the coarse-graining scheme we use and in section 4.4 we test the scaling method for multiple nanorods. In section 4.5, three nanorod composites of varying internal orientational order are introduced and their effective macrospin parameters are determined. In section 4.6 we study the hysteresis loops of 2 NPs as a function of separation, and test the macrospin models in this context. Finally, we present our conclusions in section 4.7. As choosing the proper time step for simulating a system of study is another challenging detail in such numerical studies [24, 25], we address it for our system in appendix 4.A. In appendix 4.B, we present results on the interplay between inter-rod exchange, magnetostatics and relative placement of two nanorods.

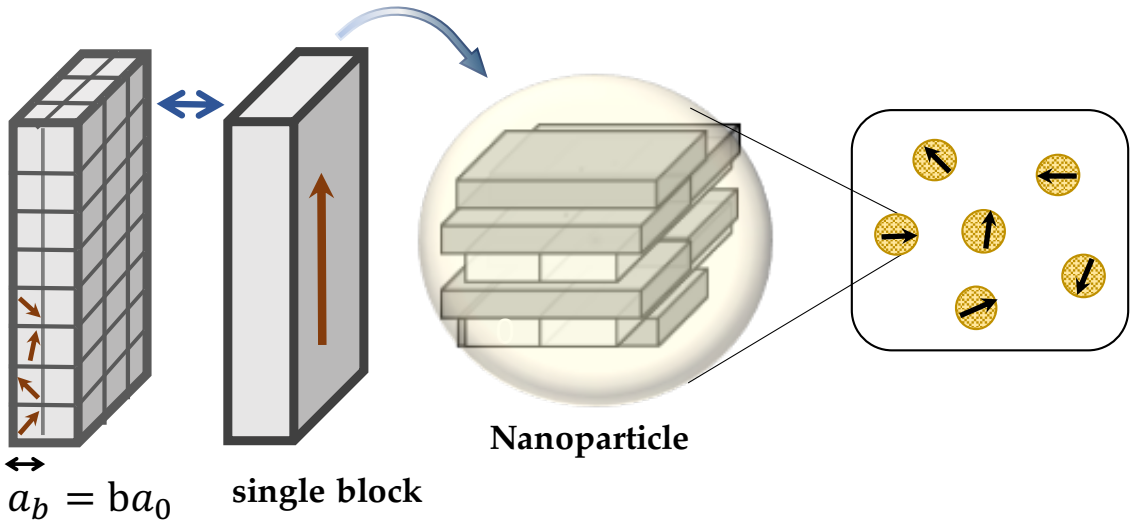

Figure 4.1: Coarse-graining model of a magnetite nanorod. The smallest micromagnetic cell corresponds to the cubic unit cell of length $a_0 = 0.839$ nm with ferrimagnetic atomic spins represented by single magnetic moment. Larger cells are characterized by a length $a_b = b\,a_0$ for $b > 1$. The number of cells is reduced from $56\times24\times8 = 10752$ to $N_b = 10752/b^3 = 1344$, 168 and 21 for $b = 2$, 4 and 8 respectively. A single block corresponds to $b = 22$. Nanoparticles are made of nanorods.

4.2 The model

We wish to simulate iron oxide nanorods made of magnetite or maghemite (γ-Fe_2O_3), while including magnetostatic interactions. These two iron oxides have similar magnetic parameters, with the exception of crystalline anisotropy, which is cubic in magnetite and uniaxial for maghemite. Our research is inspired by experimental results reported by Dennis et al. [3], in which nanorods are the building blocks of nanoparticles (see Fig. 2 therein). We study here assemblies of up to ten nanorods as single nanoparticles to explore their collective heating behaviour by calculating hysteresis loops. The size of simulated nanorods and resulting NPs reflect those studied in Ref. [3].

For simulating nanorods with nominal dimension 6.7 nm × 20 nm × 47 nm (Fig. 4.1), we use the OOMMF [4] software package, and the smallest simulation

cell we use has the dimensions of the unit cell of ferrimagnetic magnetite, represented by a single magnetization vector. OOMMF implements magnetostatics by calculating the demagnetization field at each cell using the expressions found in Refs. [26] and [27], and employs fast Fourier transforms for computational efficiency. We employ the Theta Evolve module [28] required for simulations at finite T. The LLG equation is commonly used to describe the dynamics of magnetic moments [29–31] by describing the precession and damping of a cell's magnetic moment in an effective field. The value of damping constant α, representative of energy dissipation, for magnetite films has been reported in a range from 0.03 to 0.2 depending on the thickness [32]. Setting $\alpha = 0.1$ for our system size is consistent with other reported micromagnetic studies [33, 34]. The effective field combines Zeeman, exchange, magnetocrystalline anisotropy and magnetostatic terms. Additionally, Brown [31] provided a formalism to add thermal effects into the calculations via a random effective field. It is known that thermal fluctuations are more pronounced for smaller simulation volumes prone to superparamagnetism and simulation results strongly depend on cell size [2, 24, 35]. We explore the cell size and time step correlation in 4.7 for simulations at finite T.

As in I, we use the bulk magnetite parameters with a saturation magnetization $M_s = 480$ kA/m [36–38] and exchange stiffness constant $A_0 = 0.98 \times 10^{-11}$ J/m [38–44] which leads to the critical temperature of $T_c = 858$ K for its cubic unit cell size $a_0 = 0.839$ nm. Magnetite (Fe_3O_4) possesses cubic crystalline anisotropy [5, 33, 37, 45, 46], and as it has only a weak tendency to produce hysteresis, we omit it in magnetite simulations. However, nanorods may contain significant amounts of maghemite with uniaxial crystalline anisotropy with energy density of $K_0 = 10$ kJ/m^3 [5, 33, 47], used in maghemite simulations in the present study. Otherwise, we use the same parameters for maghemite as for magnetite.

To restrict the uncontrolled heat generated by eddy currents in the surrounding tissue, the product of amplitude and frequency of the AC magnetic field should be less than a threshold that limits the sweep rate of the applied AC field to SR $= 4H_{\max}f <$ 0.25 Oe/ns [36, 48], with frequency f of a sinusoidal field of amplitude $H_{\max}$. (It is noteworthy that safe higher thresholds have been reported for particular types of cancerous tissue [15, 49].) As in I, all of the dynamic hysteresis loops reported in the present study are performed at $T = 310$ K, and we use SR = 25 Oe/ns and $\alpha = 10$. This combination of SR and α is equivalent to the hyperthermia-relevant SR = 0.25 Oe/ns and $\alpha = 0.1$ for magnetite NPs. This method of increasing α to simulate an effectively slower SR provides significant computational speed-up [1].

The nanorod that we simulate has dimensions $8a_0 \times 24a_0 \times 56a_0$ (with volume $V_{\text{rod}} = 6350.0$ nm^3), with its longest edge along the z axis. The rod is made up of N_b cubic cells with side length $a_b = ba_0$ ($b = 1, 2, 4, 8$) while the volume of the rod is fixed for all simulations. A rod is composed of 10752 cells when the smallest cell (b=1) is used, and employing larger cells reduces the number of cells dramatically, as $N_b = 10752/b^3$, to 1344, 168 and 21 for $b = 2$, 4 and 8, respectively. Ultimately, RG scaling enables the description of a rod as a block, corresponding to $b = 22$ ($\sqrt[3]{8 \times 24 \times 56}$), with a single magnetization vector with essentially the same hysteresis loop as obtained with the smallest cell size, even with magnetostatic interactions included. The impact of coarse-graining on loops is then examined for collections of nanorods that form nanoparticles as a foundation for simulating groups of NPs; see Fig. 4.1.

In calculating hysteresis loops for any cell size, we apply an external magnetic field (usually) along the z axis of $H(b) = H_{\max} \sin(2\pi f t)$. When uniaxial anisotropy is present, anisotropy directions for different cells within a nanorod are given by small

random angles from the long axis of the rod (usually the z-axis) drawn from a normal distribution with a standard deviation of 5°, i.e., anisotropy is along the long axis but with a small dispersion to imitate lattice disorder [18, 33]. $M(b)$ is the component of the magnetization along the field axis, which we calculate by averaging over 90 to 100 independent simulations (averaging at each value of the field). We report either $M(b)$ or its normalized form $m_H = M(b)/M_{\rm s}$. At the beginning of a loop calculation, magnetic moments are randomized and $M(b)$ is approximately zero. For the first quarter period, $H(b)$ goes from 0 to $H_{\rm max}$, and we report results for the subsequent period.

The error bars for the coercive field H_c are calculated as one standard error above and below its mean value, obtained by considering the standard deviation of the mean of H_c over the simulation ensemble used for each loop calculation, rather than considering the mean value of m_H and its standard deviation.

4.3 Coarse-graining and demagnetization

A few different approaches to scaling magnetic parameters such as K and A with simulation cell size have been proposed in the literature [2, 50–52]. As presented in I, we follow a modified version of the RG approach of Grinstein and Koch [2], which results in a set of equations for the magnetization, exchange stiffness, applied field,

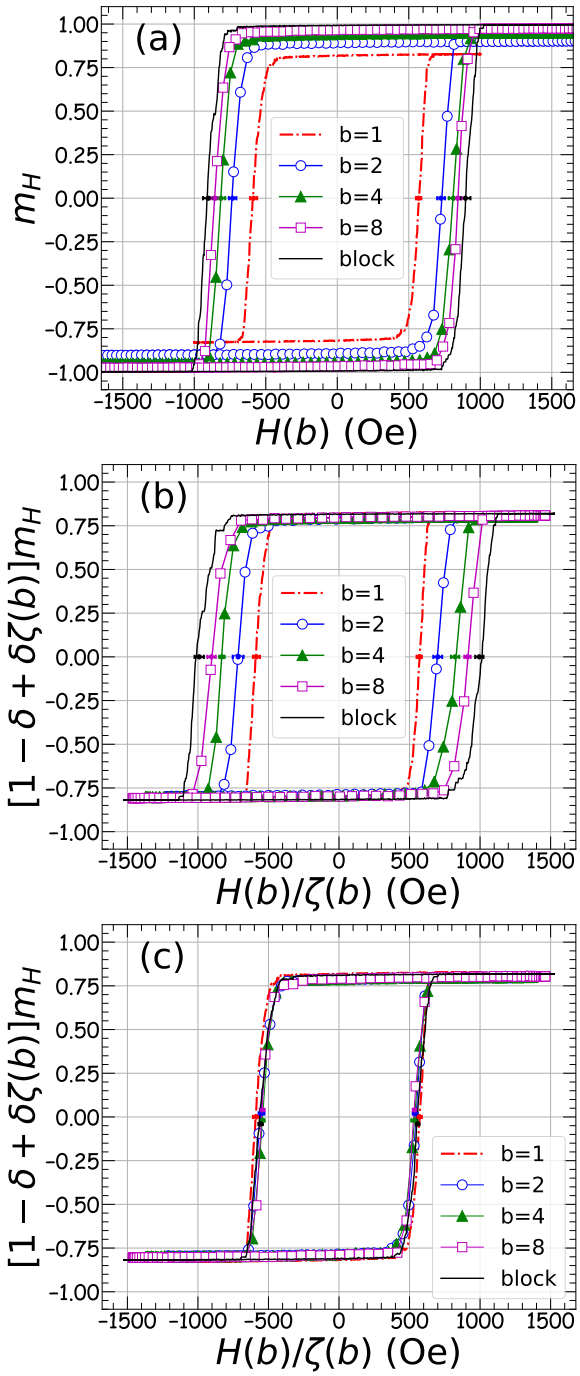

Figure 4.2: (a) Rod hysteresis loops when none of the magnetic parameters are scaled. (b) Scaling based on our modified Grinstein-Koch RG method [1, 2] ($\delta \simeq 0.511$) as in Eqs (1) - (5), but with no scaling of magnetostatic interactions. (c) Magnetostatic energy is scaled with the factor $D_{\rm scl} = \zeta(b)^3$.

and anisotropy constant,

$$M_0 = \delta\zeta(b)M(b) + (1-\delta)M(b) \tag{4.1}$$

$$A(b) = \zeta(b) \times A_0 \tag{4.2}$$

$$H(b) = \zeta(b) \times H_0 \tag{4.3}$$

$$K(b) = \zeta(b)^3 \times K_0 \tag{4.4}$$

where,

$$\zeta(b) = t/b + 1 - t, \qquad t = T/T_c, \tag{4.5}$$

A_0, K_0, H_0 and M_0 are the quantities for simulations using cell size a_0, T_c is the critical temperature, and the quantities $A(b)$, $K(b)$, $H(b)$ and $M(b)$ are those for a simulation where the cell size is $a_b = ba_0$ (with $b > 0$). For example, in carrying out a simulation with $b = 2$, the cell length is increased to $2a_0$, the anisotropy parameter set as input to the program is $\zeta(2)^3 K_0$, the exchange constant is set to $\zeta(2)A_0$, the magnitude of the field entered into the program is $H(2)$ and the program returns $M(2)$. One then calculates M_0 from Eq. 4.1 in order to compare to the results of a simulation carried out with cell length a_0, anisotropy K_0, exchange A_0 and field H_0. The phenomenological parameter $\delta = 0.511$ was determined in I from the T dependence of M for our nanorods. In the present work, we propose and test a scaling for magnetostatic interactions not previously considered.

As a first step in determining a scaling for magnetostatic interactions, we calculate a reference hysteresis loop for $b = 1$ for a maghemite nanorod by running simulations using A_0 and K_0 for the exchange and uniaxial anisotropy parameters, respectively, and include magnetostatic interactions. Results are given by the red curve in all panels of Fig. 4.2. We then carry out loop simulations with cell sizes ba_0, for $b = 2$,

4, and 8. For $b = 22$, the dimensions of the single cell are those of the nanorod itself. For these simulations, we use unrenormalized exchange and anisotropy parameters $A(b) = A_0$, $K(b) = K_0$, and again include magnetostatic interactions. The loops resulting from these non-scaled simulations are plotted in Fig. 4.2a, showing a very significant increase in loop size as cell size increases.

We repeat the loop calculations for $b > 1$ using values of $A(b)$ and $K(b)$ from Eqs. 4.2 and 4.4, respectively, and with M and H scaled via Eqs. 4.1 and 4.3, so that we plot $m_H = M_0/M_\mathrm{s} = (\delta\zeta(b)+1-\delta)M(b)/M_\mathrm{s}$ as a function of $H_0 = H(b)/\zeta(b)$, and again we include full magnetostatic interactions. The resulting hysteresis loops are different for different b, with coercivity increasing with cell size, as shown in Fig. 4.2b.

From the above results, it is clear that magnetostatic interactions need to be scaled as cell size changes. Looking at the energy terms in the Hamiltonian (see 4.7) and noting that the exchange energy ($aA\sum m_i.m_j$) is proportional to the cell length and A is scaled with $\zeta(b)$, whereas the magnetocrystalline anisotropy energy ($K_u v \sin^2(m_i.u)$) is proportional to the cell volume and K_u is scaled with $\zeta^3(b)$, we propose a $\zeta^3(b)$ scaling for the demagnetization energy, which is also proportional to the cell volume. The magnetostatic energy is $\mu_0 v M_\mathrm{s}^2 m \cdot N \cdot m/2$, where the demagnetization tensor N is determined by the geometry of the system. We repeat the loop calculations for $b > 1$, again using RG scaling for A, K, M and H, but now multiply magnetostatic energies and torques by $\zeta(b)^3$. As can be seen in Fig. 4.2c the collapse of the data is reasonably good. The loop areas for $b = 1$, 2, 4, 8 and block simulations are 1881, 1706, 1691, 1703, 1800 Oe, respectively. The smallest loop area (for $b = 4$) is 10% smaller than the area for $b = 1$. We note that comparing the above hysteresis loops with a system without magnetostatic interactions (Fig. 2c in I) supports a result from Mehdaoui et al. [8], namely, that including magnetostatic interactions increases the

squareness of the loops.

To accomplish the scaling of magnetostatic interactions when using OOMMF, we take the approach of scaling M_s, while ensuring that all other terms in the effective field remain unchanged. The magnetostatic energy is proportional to M_s^2. Therefore, multiplying M_s by $\zeta(b)^{3/2}$ results in the desired scaling of magnetostatic interactions with $\zeta(b)^3$. At the same time, scaling M_s changes the non-magnetostatic contributions to the effective field entering the LLG calculations, namely the exchange, anisotropy and thermal contributions. We must therefore introduce additional scaling to preserve $\mathbf{H}_\mathrm{eff} = \mathbf{H}_\mathrm{exch} + \mathbf{H}_\mathrm{anis} + \mathbf{H}_\mathrm{ext} + \mathbf{H}_\mathrm{thermal}$ invariant to changes in M_s. Thus, when changing program input M_s to $M_\mathrm{s}\zeta(b)^{3/2}$, we must additionally change A to $A\zeta(b)^3$, K to $K\zeta(b)^{3/2}$ and T to $T\zeta(b)^{3/2}$ in order to keep field strengths $H_\mathrm{exch} = 2A/\mu_0 a M_\mathrm{s}^2$, $H_\mathrm{anis} = 2K/\mu_0 M_\mathrm{s}$, and $H_\mathrm{thermal} = [2\alpha k_B T/(\gamma\mu_0 M_\mathrm{s} V \Delta t)]^{1/2}$ unaltered. The end result is that in order to carry out a simulation at $b > 1$ and temperature T_0, we first calculate $\zeta = \zeta(T_0, b)$, and the set program inputs to $M_\mathrm{s} = M_{s0}\zeta^{3/2}$, $A = A_0\zeta^4$, $K = K_0\zeta^{9/2}$, and $T = T_0\zeta^{3/2}$. The external field $H(b)$ is unchanged. This recipe combines the RG scaling of A and K with appropriate scaling of magnetostatics, and yields $M(b)$.

The next step is to model the collective effect of the magnetocrystalline anisotropy, exchange and magnetostatic interactions of a rod with a single magnetization (macrospin) subject to uniaxial anisotropy. This step is justified by the rather good agreement in the MH loops between the fine grain simulation ($b = 1$), and the single block case ($b = 22$), for which a single magnetization represents the entire rod and no explicit exchange interactions are present. This macrospin description is known as the

Stoner-Wohlfarth (SW) model, and the Hamiltonian is,

$$\begin{aligned} \mathcal{H} &= \mathcal{H}_{\text{anisotropy}} + \mathcal{H}_{\text{Zeeman}}, \\ \mathcal{H}_{\text{anisotropy}} &= -K_{\text{eff}} v(\mathbf{m}\cdot\mathbf{u})^2, \\ \mathcal{H}_{\text{Zeeman}} &= -\mu_0 M_s^{\text{eff}} v(\mathbf{m}\cdot\mathbf{H}), \end{aligned} \tag{4.6}$$

where the uniaxial anisotropy has energy density K_{eff} with its axis along $\mathbf{u}$, and the single magnetization vector has direction $\mathbf{m}$ and magnitude M_s^{eff}. K_{eff} and M_s^{eff} arise from the combined effects of self-demagnetization, magnetocrystalline anisotropy, exchange, and temperature. For the macrospin model of the nanorod $v = V_{\text{rod}}$. μ_0 is the permeability of free space and $\mathbf{H}$ is the externally applied field. This SW macrospin model may be useful for simulating a group of nanorods in solution, for example, and it is understood that interactions between rods include magnetostatic interactions, perhaps in the dipole approximation. This macrospin description differs from the $b = 22$ block model in that, first, the self-magnetostatic interaction is accounted for by the effective uniaxial anisotropy, and second, there is no need to worry about the procedures to implement RG and magnetostatic scaling.

To find the appropriate parameters to model the nanorod as a SW-macrospin at 310 K, we calculate the hysteresis loop of the nanorods modelled using $b = 4$, averaging over field directions. Given the symmetry of the rod, we integrate directions over a spherical octant, and, following the numerical algorithm presented in Ref. [53], we employ a seven-point integration scheme, with directions shown in the inset of Fig. 4.3a. We also calculate the directionally averaged loop for a SW particle at 310 K by simulating 1000 particles with random orientations (uniformly over a sphere), and then scaling the parameters of the SW particle to match H_c and remanent magnetization M_r of the rod. For a magetite rod ($K = 0$), we find that $K_{\text{eff}} = 15.7$ kJ/m^3 and

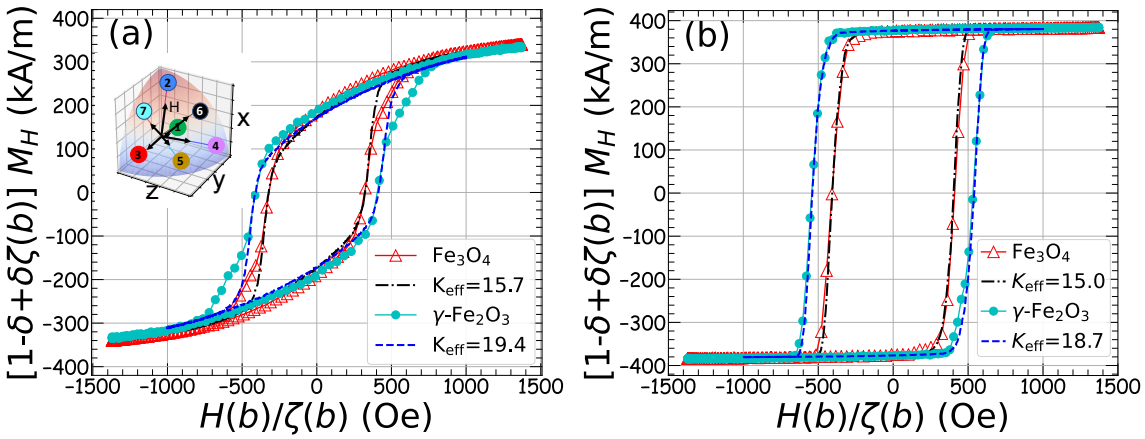

Figure 4.3: Comparison of macrospin models (dashed and dot-dashed lines) with magnetite and maghemite nanorods (solid lines with symbols) for (a) rotationally averaged external field (inset shows field directions used in the numerical integration used to obtain the average), and (b) external field along the z axis. Macrospin models in (a) and (b) have $M_{\rm s}^{\rm eff} = 350$ and 384 kA/m, respectively.

$M_s^{\rm eff} = 0.73 M_{\rm s} = 350$ kA/m. Results are plotted in Fig. 4.3a. It is important to note that if one wished to plot m_H, one should normalize M_H by $M_{\rm s}$, rather than by $M_s^{\rm eff}$, in order to compare with nanorod loops. For a maghemite rod ($K_0 = 10$ kJ/m^3), we find $K_{\rm eff} = 19.4$ kJ/m^3 and $M_s^{\rm eff} = 0.73 M_{\rm s} = 350$ kA/m.

From the loops shown in Fig. 4.3a, it is clear that the rod does not precisely follow the SW model. This is because the magnetostatic interactions within the rod only approximately map to a single anisotropy axis. In Fig. 4.3b, we plot the MH loops for the $b = 4$ approximation for the rod and the SW counterpart when the field is along the z axis, i.e., along the anisotropy axis. In this case, we find a smaller value of $K_{\rm eff} = 15.0$ kJ/m^3 for magnetite, with $M_{\rm s}^{\rm eff} = 0.8 M_{\rm s} = 384$ kA/m. This value of $K_{\rm eff}$ is smaller than the analytical result at $T = 0$, $K_{\rm eff}^{T=0} = 20.5$ kJ/m^3, which we obtain by following Refs. [26, 27, 29, 54].* For maghemite, we obtain $K_{\rm eff} = 18.7$ kJ/m^3 with $M_{\rm s}^{\rm eff} = 0.80 M_{\rm s} = 384$ kA/m. All effective parameters are summarized in Table 4.1.

*For this thesis, we provide details of the calculation in appendix A.

Table 4.1: The effective anisotropy and saturation magnetization of macrospins equivalent to simulated nanorods and nanoparticles. K_{eff} and $M_{\text{s}}^{\text{eff}}$ are summarized for results shown in Fig. 4.3 for nanorods, and Figs. 4.5 (rotationally averaged) and 4.6 (field along z) for NPs. The bulk saturation magnetization is $M_{\text{s}} = 480$ kA/m. The nanorods have dimensions 6.7 nm $\times$ 20 nm $\times$ 47 nm, and consequently the NPs have an approximate diameter of 47 nm.

material	object	K_{eff} (kJ/m^3)	H	$M_{\text{s}}^{\text{eff}}$ (kA/m)
Fe_3O_4	nanorod	15.73	rot. avg.	350
Fe_3O_4	nanorod	15.0	$\|\|z$	384
γ-Fe_2O_3	nanorod	19.4	rot. avg.	350
γ-Fe_2O_3	nanorod	18.7	$\|\|z$	384
Fe_3O_4	$6z4y$ NP	4.80	rot. avg.	382
Fe_3O_4	$6z4y$ NP	3.64	$\|\|z$	382
γ-Fe_2O_3	$6z4y$ NP	5.70	rot. avg.	382
γ-Fe_2O_3	$6z4y$ NP	4.90	$\|\|z$	382
γ-Fe_2O_3	$8z2y$ NP	8.78	rot. avg.	382
γ-Fe_2O_3	$8z2y$ NP	6.32	$\|\|z$	382
γ-Fe_2O_3	$10z$ NP	10.79	rot. avg.	382
γ-Fe_2O_3	$10z$ NP	7.63	$\|\|z$	382

4.4 Coarse-graining for multiple nanorods

As our goal is to simulate magnetic nanoparticles made of nanorods, we test the proposed scaling method for a collection of eight maghemite nanorods in two stacks of four as shown in the inset of Fig. 4.4. Simulations include magnetostatics, intrarod [$A(b)$] and inter-rod ($A_{\text{r-r}}$) exchange interactions at half strength [$A_{\text{r-r}} = 0.5A(b)$], magnetocrystalline uniaxial anisotropy along the rod's long axis and a sinusoidal field applied along the z axis.

Simulated MH loops for the eight-rod bundle show good agreement for $b = 2$, 4 and 8, whereas the loop is significantly different for a bundle of eight blocks ($b = 22$) as shown in Fig. 4.4a. Clearly, modelling the nanorod as a block with a single magnetization does not allow portions of a nanorod to flip independently of the rest of the rod, and hence the shoulder regions of the loop in particular are susceptible to

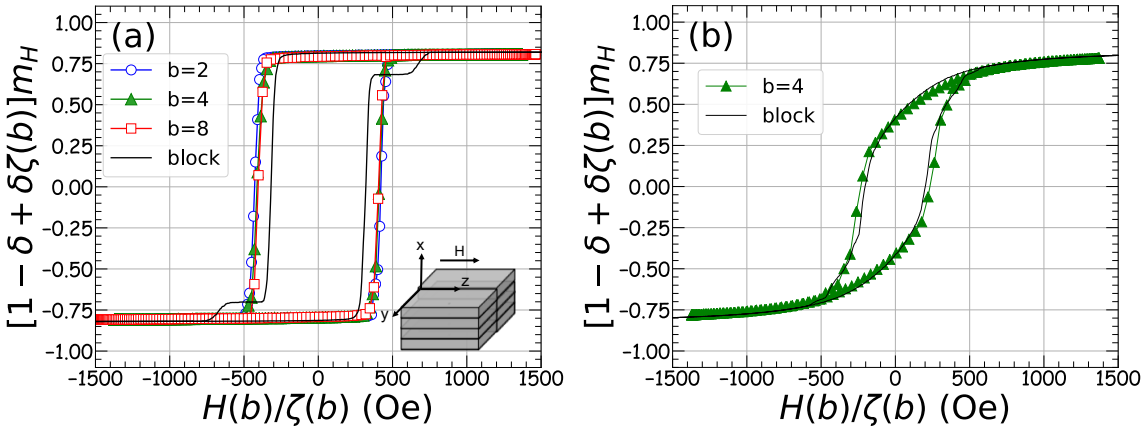

Figure 4.4: Scaling applied to a bundle of 8 nanorods with inter-rod exchange $A_{\mathrm{r-r}} = 0.5A(b)$. (a) Loops corresponding to simulation cells of length $a_b = ba_0$ for $b = 2$, 4, 8 and 22 (block) for a field applied along the z axis. (b) Loops with a rotationally averaged field for nanorods modelled with $b = 4$ and 22 (block).

unphysical behaviour. Thus, magnetostatic interactions limit the present prescription for coarse-graining in the case of bundled nanorods.

We expand our exploration by comparing the average MH hysteresis loop of this group of nanorods when the applied field is rotationally averaged. Interestingly, averaging over field directions masks the discrepancy between $b = 4$ and the block approximation, as shown in Fig. 4.4b. We conclude that $b = 4$ is a reasonable level of coarse-graining for the investigation of multiple-rod configurations in the remainder of the present work.

In appendix 4.B, we investigate the interplay between magnetostatic interactions, inter-rod exchange, and geometric arrangement for a system of two nanorods. We find that the dynamics may be complex, such that, for example, increasing $A_{\mathrm{r-r}}$ does not necessarily increase loop area.

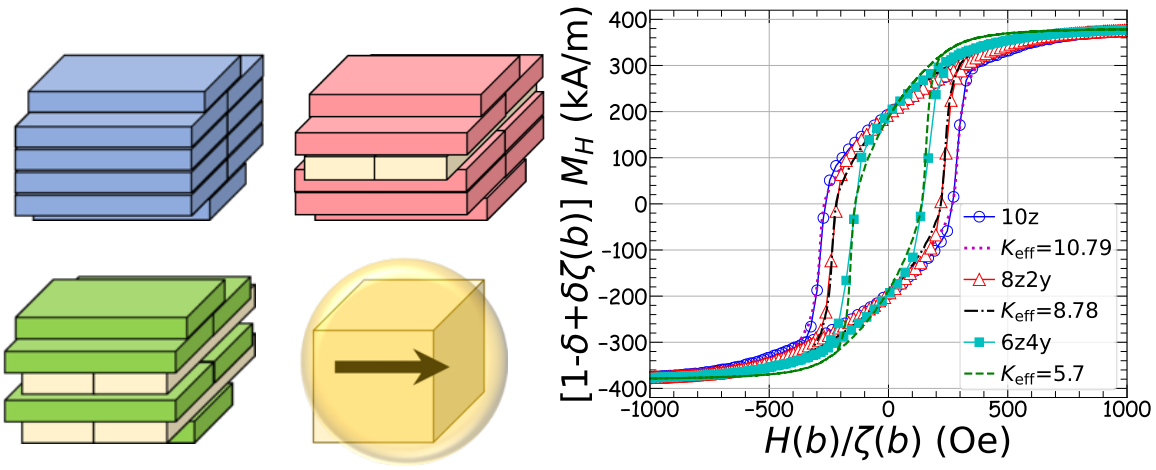

Figure 4.5: Three different NPs, $10z$, $8z2y$ and $6z4y$, each assembled from 10 maghemite nanorods. The right graph shows the NP hysteresis loops for rotationally averaged field (solid curves with symbols), and loops for their equivalent macrospins with the same M_r and H_c (dashed curves). Macrospins equivalents to each NP have $K_{\text{eff}} = 5.70$, 8.78 and 10.79 kJ/m^3 for $6z4y$, $8z2y$ and $10z$ NPs, respectively, and $M_{\text{s}}^{\text{eff}} = 382$ kA/m.

4.5 Nanoparticles

Our basic model of nanoparticles composed of nanorods is inspired from the experimental study by Dennis et al. [3]. There are, however, no data on how nanorods are packed within a nanoparticle, and two extreme possible assemblies are a totally ordered stack of nanorods and a random cluster of nanorods [6]. Among various possible arrangements, we choose three assemblies containing 10 maghemite ($K_0 = 10$ kJ/m^3) nanorods, one with all the nanorods along the z axis (which we label $10z$), another one with 8 along the z axis and 2 along the y axis ($8z2y$) and a third arrangement with 6 nanorods along z and 4 along y ($6z4y$), as shown in Fig. 4.5a. With these three choices, we mimic some degree of disorder by varying the degree of rod alignment. To compare the heating efficiency of these constructions with the experimental results, we calculate the rotationally averaged hysteresis loop, coarse-graining the rods at the

$b = 4$ level (including magnetostatic scaling) and assuming $A_{\mathrm{r-r}} = 0.5A(b)$. As expected, assemblies with more parallel nanorod arrangement exhibit wider hysteresis loops, as shown in Fig. 4.5b, which leads to higher heating efficiency.

The next step in simplifying the simulation of NPs is to find the magnetic parameters of a SW macrospin that gives the most similar MH hysteresis loops (the same M_r and H_c) to nanoparticles of the same volume. This level of modelling enables the description of a complex nanoparticle made of nanorods with a single macrospin and replacing all the magnetostatic and exchange interactions inside the NP with an effective uniaxial anisotropy of the macrospin. The resulting fits, made by adjusting K_{eff} and $M_{\mathrm{s}}^{\mathrm{eff}}$, are shown in Fig. 4.5b, and the effective uniaxial anisotropy for the three maghemite nanoparticle models $10z$, $8z2y$ and $6z4y$ are 10.79, 8.78 and 5.7 kJ/m^3, respectively, with effective saturation magnetization equal to $M_{\mathrm{s}}^{\mathrm{eff}} = 0.795M_{\mathrm{s}} = 382$ kA/m for all three models. Effective parameters for maghemite and magnetite nanoparticles are given in Tab. 4.1.

As with the case of individual rods, it is expected that a single anisotropy axis is not completely sufficient to model the magnetic response. Fig. 4.6a shows the response of the $6z4y$ magnetite nanoparticle model to both rotationally averaged fields and for fields along x, y and z directions, along with corresponding responses of the SW macrospin model that best matches the rotationally averaged response of the nanoparticle ($K_{\mathrm{eff}} = 4.8$ kJ/m^3). The nanoparticle loops for the x and y directions are non-linear at moderate field magnitudes and have non-zero loop areas, while the macrospin model shows linear response until saturation and zero loop area. Also shown is the loop for the macrospin model with a reduce effective anisotropy ($K_{\mathrm{eff}} = 3.64$ kJ/m^3) that best matches the nanoparticle's repsonse to a field in the z direction. Fig. 4.6b shows that lower values of K_{eff} are need to reproduce the response

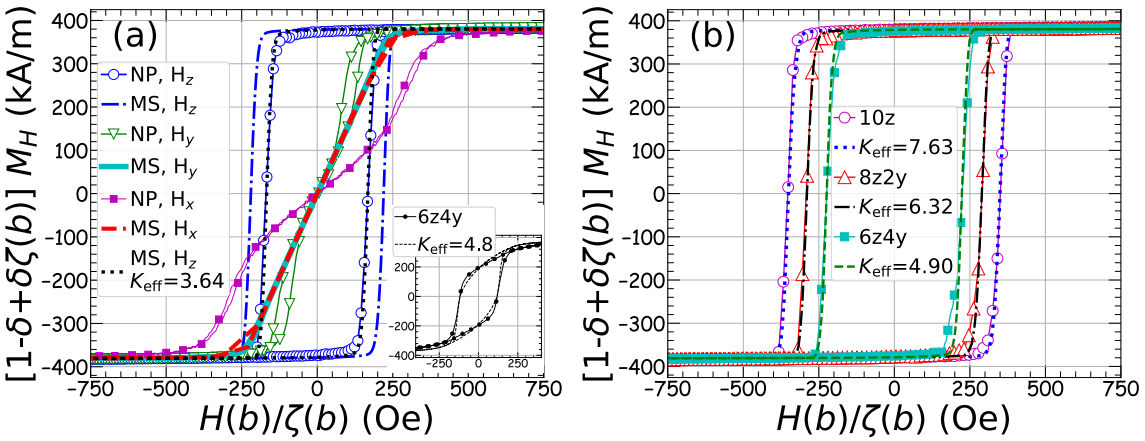

Figure 4.6: Impact of changing field direction on loops for NPs composed of rods (solid lines with symbols), and equivalent macrospin (MS) particles (broken lines). a) Magnetite for three field directions. A MS particle with $K_{\text{eff}} = 4.8$ kJ/m^3 and $M_{\text{s}}^{\text{eff}} = 382$ kA/m has the same M_r and H_c as a $6z4y$ magnetite NP ($K_0 = 0$) under rotationally averaged field (inset), whereas it exhibits different MH hysteresis loops when field is applied along the x, y or z axes. For the field applied along the z axis, a MS with $K_{\text{eff}} = 3.64$ kJ/m^3 (black dotted line) yields approximately the same hysteresis loop to the NP (open circles). b) Maghemite for the field along z. K_{eff} decreases relative to the rotationally averaged case (see Fig. 4.5b), and has values 4.90 kJ/m^3, 6.32 kJ/m^3 and 7.63 kJ/m^3 for the $6z4y$, $8z2y$ and $10z$ maghemite NPs, respectively.

of maghemite nanoparticles to fields along z. The equivalent effective anisotropy under H_z decreases to 4.90, 6.32, and 7.63 kJ/m^3 for $6z4y$, $8z2y$, $10z$ maghemite nanoparticles, respectively. Effective parameters are summarized in Tab. 4.1. The up to approximately 35% difference in K_{eff} values comparing rotationally average and z responses can either be regarded as a model error when using the macropsin model for future purposes, or one may preferentially choose one scenario over the other depending on context. For example, in a medium in which the nanoparticles are free to rotate and therefore can align anisotropy axes along the field, the lower K_{eff} values obtained from the z response should be used, while for randomly oriented particles unable to rotate, the rotationally averaged may be more relevant.

4.6 Interacting nanoparticles

As a prelude to later explorations of the collective heating behavior of NP chains, as in Ref. [55], we simulate two magnetite $6z4y$ NPs ($K_0 = 0$) and study how their hysteresis loop changes as the nanoparticle center-to-center distance r varies from one to three NP diameters (d = 47.0 nm). For these simulations, the rod centres and the majority of the rod long axes of both NPs lie on (or parallel to) the z axis, the external field is also along z, and we use $b = 4$ for coarse-graining (including magnetostatic scaling). This arrangement mimics chain formation when NPs are free to move and rotate. As shown in Fig. 4.7a, the hysteresis loop area is larger in the case of two interacting chained NPs compared to isolated NPs. This is in agreement with reported results [8, 18, 22]. We note that the normalization of the loop is such that the total heat released would require multiplication by the number of particles in the system. As r increases, the effect of magnetostatic interactions between NPs is reduced and their loop area shrinks[17]. By $r \approx 3d$, the loop is approximately the same as for noninteracting NPs.

To quantify the r dependence of the loop area and H_c, we plot the difference in areas ΔS between loops for the 2-NP systems and individual NPs (ΔS = Area(2NPs) - Area(1NP)), as well as the difference in the coercivities ΔH_c, as functions of r in Fig. 4.7b. As may be expected, for $r > 1.5d$, ΔS and ΔH_c decrease with a $1/r^3$ dependence, just as the energy between two dipoles does. This motivates using the dipole approximation to calculate the heating efficiency of NPs when they are further apart than $1.5d$.

To this end, we carry out two additional sets of simulations. First, we use the effective macrospin parameters for the $6z4y$ magnetite NP (K_{eff} = 3.64 kJ/m^3, M_{s} = 381.6 kA/m) and simulate two magnetized cubes with the same volume as

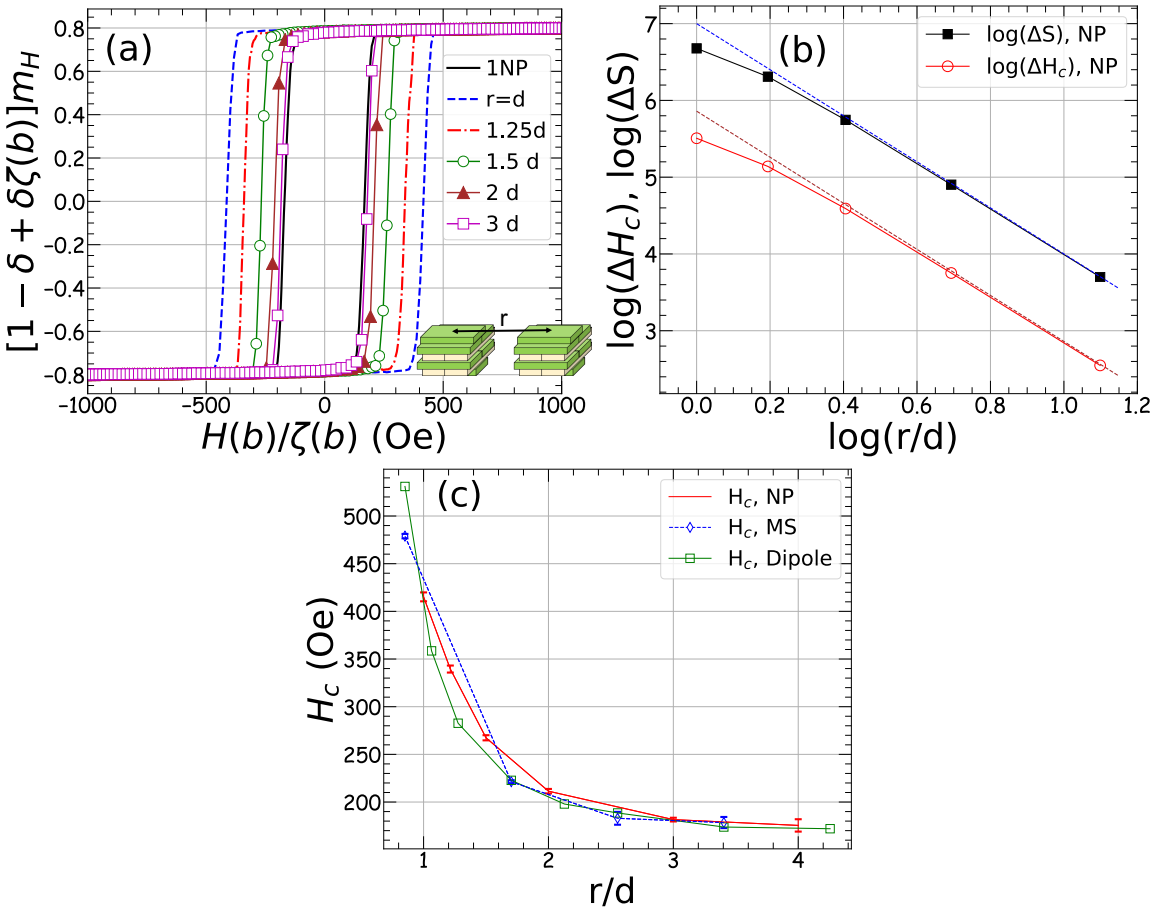

Figure 4.7: a) Hysteresis loops for a system of 2 magnetite $6z4y$ NPs as a function of centre-to-centre distance r. d is the NP diameter. b) The quantities ΔH_c and ΔS (see main text for definitions) as functions of r approach dipolar scaling near $r/d = 1.5$ ($\ln 1.5 \approx 0.405$). Dashed lines are r^{-3} power laws. (c) H_c as a function of r for the 2-NP loops from panel (a), along with H_c obtained from macrospin approximations to the NPs, realized through uniformly magnitized cubes (MS) and dipolar spheres (Dipole). Error bars for the dipole curve are comparable to symbol size.

the NP, placing their centres and anisotropy axes on the z axis, and calculating loops as we vary r. For these simulations, we include magnetostatics interactions, both between the cubes and within each cube. Allowing for self-demagnetization is technically inconsistent with our approach, because the effects of self-demagnetization are accounted for in K_{eff}. However, self-demagnetization leads only to cubic anisotropy

that has little effect on hysteresis loops. Similarly, we simulate with Vinamax software [56] two spheres with the same effective parameters as the cubes and dipole moment $vM_{\mathrm{s}}^{\mathrm{eff}}$, thus neglecting self-demagnetization (as is consistent with the effective parameters) and treating interaction between spheres in the dipolar approximation. We report H_c for the two macospin models and the $6z4y$ NPs in Fig. 4.7c, with cubes labelled *MS* and spheres labelled *Dipole*. The agreement between all three sets of data is satisfactory for $r \geq 1.5d$.

4.7 Conclusions

The present work represents the first comprehensive study of coarse-graining for use in micromagnetic simulations. We extend an RG-based coarse-graining scheme, previously developed and explored in I, to include magnetostatic interactions in micromagnetic simulations, and apply it to dynamic hysteresis loops at $T = 310$ K of magnetite (no magnetocrystalline uniaxial anisotropy) and maghemite nanorods, as well as collections of stacked nanorods that model NPs of varying internal orientational order.

For individual nanorods, the coarse-graining procedure reproduces loops even up to the representation of the nanorod as a block with a single magnetization. For collections of rods, the interplay between inter-rod exchange and magnetostatic interactions can lead to complex magnetization dynamics (as in appendix 4.B), and we limit our level of coarse graining to $b = 4$ (cell length four times larger than the unit cell of magnetite) when simulating 10-nanorod model NPs.

For both individual nanorods and NPs, we find the effective uniaxial anisotropy and saturation magentization parameters for SW macrospin models that yield equivalent loops. For nanorods, the effective anisotropy is approximately 15-16 kJ/m^3

for magnetite, and approximately 19 kJ/m^3 for maghemite. The effective saturation magnetization is 73% to 80% of the bulk value, depending on whether orientation with respect to the external field is assumed to be rotationally averaged or parallel. For our 47 nm-diameter NPs, the effective anisotropy falls in the range of 4 kJ/m^3 for our most orientationally disordered ($6z4y$) magnetite NP to 11 kJ/m^3 for our most ordered ($10z$) maghemite NP. The effective saturation magnetization is approximately 80% of the bulk value. For this modelling, we assume an inter-rod exchange strength of half the bulk value.

For simulations of two NPs, we find that loop area, or rather the difference in loop areas between interacting and noninteracting NPs, scales with distance in a dipole-like manner for centre-to-centre distances at and beyond 1.5 times the particle diameter. For this distance and beyond, we find good agreement between the two-NP results and those for two macrospin equivalents interacting via dipolar interactions.

We also find (appendix 4.A) that using a larger cell size allows the use of a larger step size in integrating the equations of motion. Over the range of cell sizes studied, we approximately find that if cell volume is increased, the step size may also be increased by the same factor.

Acknowledgment

We thank Michael J. Donahue for discussions and his expert guidance on how to achieve the scaling of magnetostatics with OOMMF. We also thank Mikko Karttunen for useful discussions, and both him and Styliani Consta for hosting our stay (RB and ISV) at Western University. We acknowledge the financial support from the Natural Sciences and Engineering Research Council (Canada). Computational resources were

provided by ACENET and Compute Canada.

Appendix 4.A. Time step dependence on simulation cell size

For a system of interacting micromagnetic cells with crystalline anisotropy under an external field, the Hamiltonian is,

$$\begin{aligned}
\mathcal{H} &= \mathcal{H}_{\text{exchange}} + \mathcal{H}_{\text{magnetostatics}} + \mathcal{H}_{\text{anisotropy}} + \mathcal{H}_{\text{Zeeman}} \\
\mathcal{H}_{\text{exchange}} &= -\frac{a}{2}\sum_{i}\sum_{j\in \text{NN}} A_{ij}(\mathbf{m}_i \cdot \mathbf{m}_j) \\
\mathcal{H}_{\text{magnetostatics}} &= -\frac{\mu_0 v}{2}\sum_{i,j}(\mathbf{M}_i \cdot \mathbf{N} \cdot \mathbf{M}_j) \\
\mathcal{H}_{\text{anisotropy}} &= -Kv\sum_{i}(\mathbf{m}_i \cdot \mathbf{u})^2 \\
\mathcal{H}_{\text{Zeeman}} &= -\mu_0 M_{\text{s}} v\sum_{i}(\mathbf{m}_i \cdot \mathbf{H})
\end{aligned} \tag{4.7}$$

where a is the length of a cubic cell and A_{ij} is the exchange stiffness constant. We note that the factor of 1/2 in the exchange Hamiltonian may or may not appear in the literature, reflecting whether or not interactions are effectively double counted, resulting in the apparent values of A_{ij} differing by a factor of 2. For example, for magnetite we use a value of $A_0 = 0.98 \times 10^{-11}$J/m, and to achieve this we give as input the parameter $A_{\text{OOMMF}} = 0.49 \times 10^{-11}$ J/m to OOMMF. $\mathbf{M}_k$ is a cell's magnetization with magnitude M_{s} and direction given by unit vector $\mathbf{m}_k$ $(k = i, j)$, $\mathbf{N}$ is the demagnetization tensor, representing the geometry of the system, μ_0 is the permeability of the free space and v is the cell volume. Uniaxial anisotropy is characterized by energy density K and unit vector $\mathbf{u}$, and the externally applied field is $\mathbf{H}$.

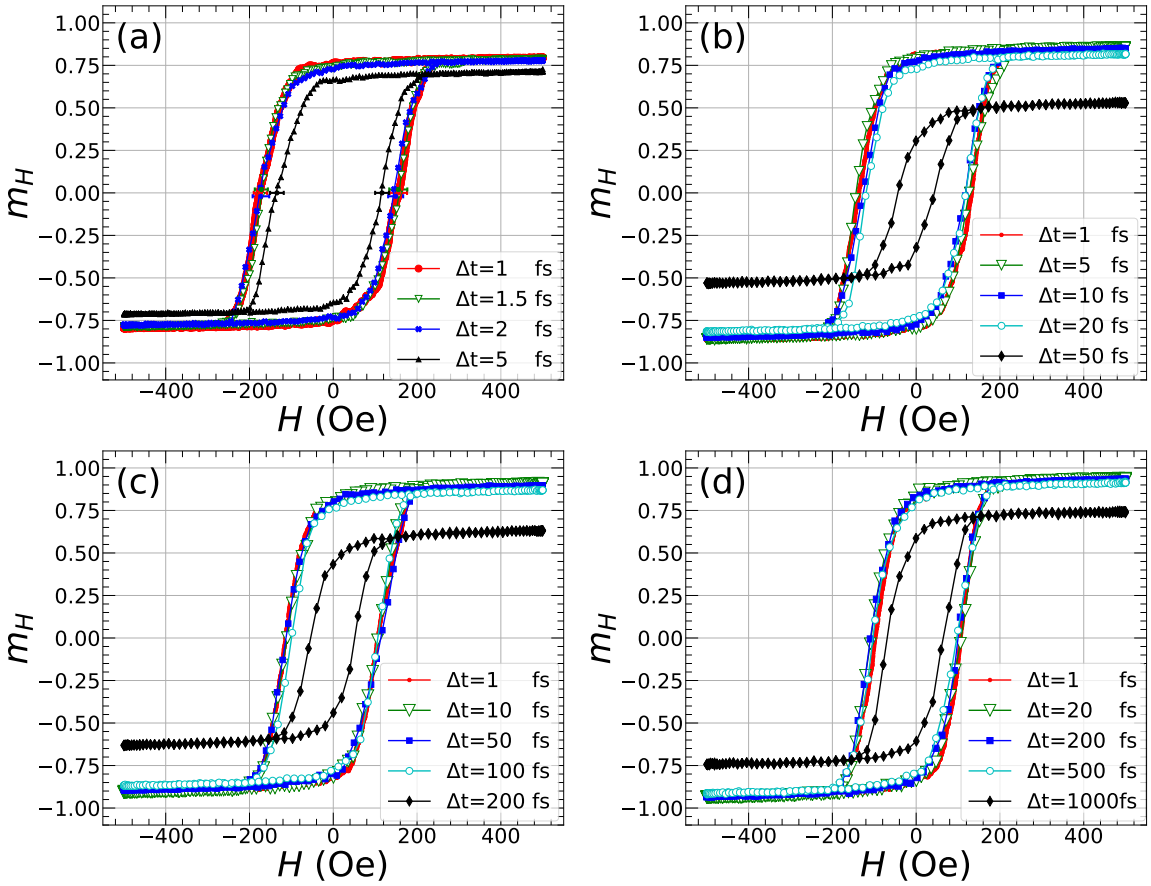

Figure 4.8: Dependence of MH loops on Δt for nanorods composed of cells of side length ba_0 for (a) $b = 1$, (b) $b = 2$, (c) $b = 4$ and (d) $b = 8$. The simulations are carried out at SR=2.5 Oe/ns, and $T = 310$ K, with $\alpha = 0.1$. Here, we neglect magnetostatic interactions.

Brown [31] modelled thermal effects with a random effective field (white noise) with spatial components drawn from a normal distribution with variance [56],

$$\sigma^2 = \frac{2\alpha k_B T}{\gamma \mu_0 M_s V \Delta t}, \tag{4.8}$$

where V is the switching volume, i.e. the volume of a micromagnetic cell, T is the absolute temperature, k_B is Boltzmann's constant, and Δt is the time step of the simulations. Eq. 4.8 implies that a larger Δt can be chosen for larger simulation cells. Therefore, when coarse-graining, not only are simulations faster on account of

employing fewer cells, but also on account of being able to use a larger Δt. In Fig. 4.8 we plot hysteresis loops for nanorods composed of cells with different volumes, given by $V = (ba_0)^3$, for different values of Δt. For these simulations, we use the RG-scaled exchange and anisotropy constants $A(b)$ and $K(b)$ as given by Eqs. 4.2 and 4.4; we also neglect magnetostatic interactions for simplicity. Overlapping curves indicate that results are independent of step size, and therefore indicate when Δt is "small enough". For $b = 1$, a small Δt of approximately 1 to 1.5 fs is required, and the optimal Δt increases to approximately 5 fs for $b = 2$, 50 fs for $b = 4$ and, remarkably, 200 fs for $b = 8$. Values of Δt larger than the optimum yield significantly smaller loop areas. This increase of time step with cell volume is consistent with previous results in the literature [24, 25].

OOMMF uses an Eulerian solver for simulations at finite T, and so the contribution to the changes in magnetization from the thermal field in a single step of the algorithm is proportional to $\sqrt{\Delta t/V}$, which implies that for $\Delta t \propto b^3$ the magnitude of these changes should remain constant. This proportionality provides a simple way of understanding the increase in optimal Δt that we observe. It should be cautioned, however, that care must always be taken to check that a sufficiently small Δt is used.

Appendix 4.B. Various 2-rod setups

Here we explore the effects of magnetostatic and exchange interactions for three different arrangements of two magnetite nanorods, providing some insight on their effects on the magnetization alignment for bundled nanorods. We use RG scaling with $b = 4$, and, for this section only, we do not carry out the scaling of magnetostatic interactions, and simply use M_s with no alteration in determining effective fields and energies. We

are simply interested in general effects of the interplay between magnetostatics and inter-rod exchange.

In the first arrangement, we consider only the effect of magnetostatic interaction between rods. One nanorod is placed along the z axis, and the other along x, with the y axis parallel to the line passing through the nanorod centers, as shown in the inset of Fig. 4.9a. The external field is along the z axis. Within each rod, magnetostatics and exchange are present. For the black curve in Fig. 4.9a, the rods do not interact: they are independent with $A_{\mathrm{r-r}} = 0$ and with no magnetostatic interactions between cells belonging to different rods. The loop, in fact, is just the average of two independent rods. The green curve in the same plot shows the loop for the case where the two rods interact magnetostatically: magnetostatic interactions are calculated between all cells in the 2-rod system. The hysteresis loop is smaller for the interacting case. This negative effect of magnetostatics on loop area is in agreement with studies reported by Cabrera et al. [22] and Serantes [18], wherein dipole interactions decrease the heating efficiency of magnetic particles when the dipoles are not arranged in end-to-end chains.

Panels b and c of Fig. 4.9 compare hysteresis loops, when inter-rod magnetostatic interactions are present, for three different inter-rod exchange strengths $A_{\mathrm{r-r}} = xA(b)$, with $x = 0$, 0.05, and 0.5. Here, the nanorods are side-by-side with their long axes parallel. Fig. 4.9b considers the case of rods with their largest faces making contact (area of contact is 84 a_4^2), and Fig. 4.9c considers the case where the nanorods are making contact through their second largest faces (area of contact is 28 a_4^2). The centers of adjacent parallel nanorods are 6.7 nm and 20 nm apart in panels b and c, respectively. In general, increasing x increases the magnetization alignment between the two nanorods, counteracting the anti-alignment induced by magnetostatics. In Fig. 4.9b, for $A_{\mathrm{r-r}} = 0$ the magnetization of one rod flips before H becomes negative.

For $A_{\mathrm{r-r}} = 0.05A(b)$ and $0.5A(b)$, the magnetizations of the two rods are locked, and higher exchange strength results in wider hysteresis loops. For the larger centre-to-centre separation (and therefore weaker inter-rod magnetostatic interactions) and smaller contact area presented in Fig. 4.9c, for $A_{\mathrm{r-r}} = 0$, the magnetization of one of the rods flips before the other, but only after the H becomes negative. At $A_{\mathrm{r-r}} = 0.05A(b)$, when the magnetization of one rod flips, it takes part of the second rod with it. Only at $A_{\mathrm{r-r}} = 0.5A(b)$ do the magnetizations of both rods flip in unison. We note that for $b = 4$, the exchange length is $\sqrt{\frac{2\zeta(4)A_0}{\mu_0 M_s^2}} \approx 7.0$ nm, and therefore significantly smaller than the centre-to-centre distance. The perhaps counter-intuitive observation is that as $A_{\mathrm{r-r}}$ increases, the loop area decreases. We conclude that the pairing of inter-rod exchange and magnetostatics can lead to complex magnetization dynamics within nanorod composites, and therefore counter-intuitive impacts of inter-rod exchange on heating efficiency.

In all 2-rod cases considered, we explicitly place the rods side-by-side and not end-to-end. Thus, we do not consider chain formation [17], which should enhance hysteresis, but rather the tendency of magnetostatics to cause anti-alignment of neighbouring nanorod magnetic moments. We note that the larger centre-to-centre distance considered in Fig. 4.9c means that the anti-aligning effects of magnetostatics is weaker, and so perhaps it is not surprsing to see a larger loop area than in Fig. 4.9b in the $A_{\mathrm{r-r}} = 0$ case.

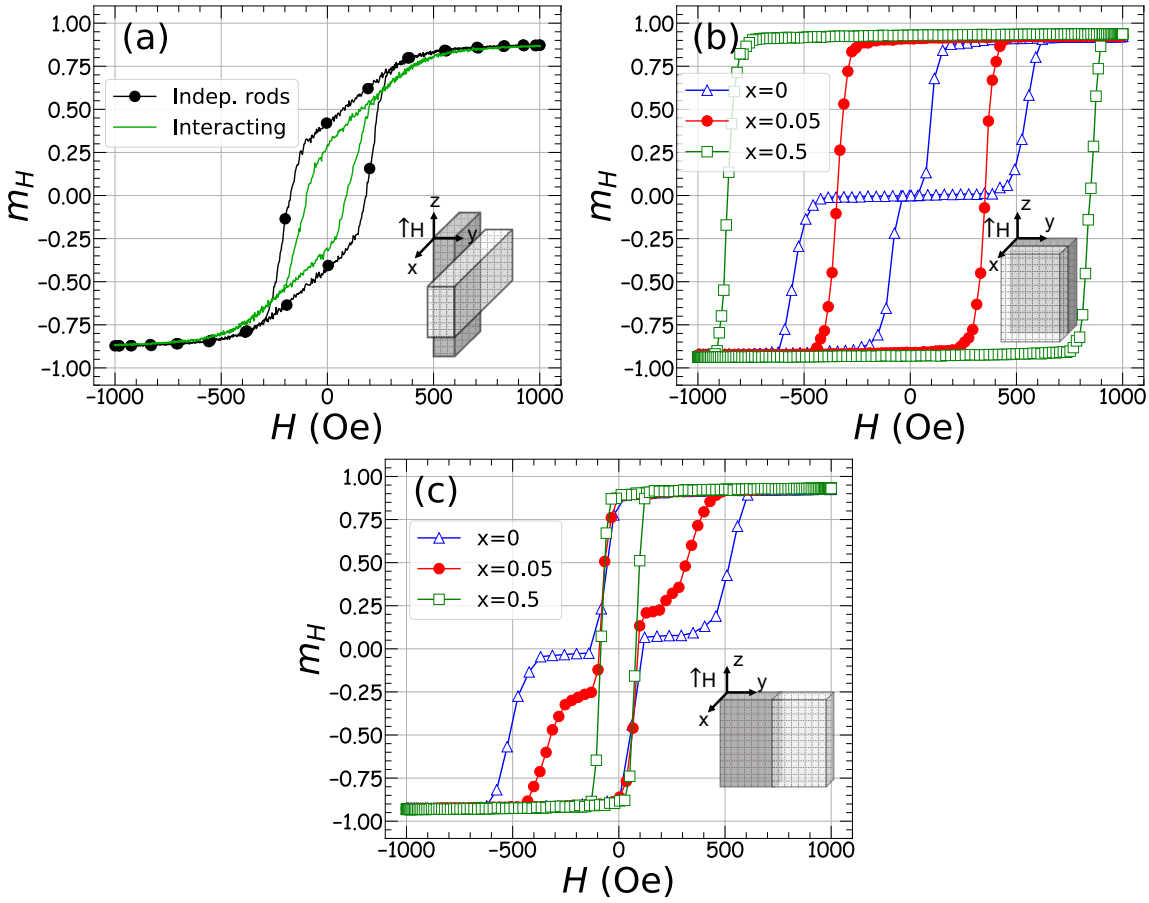

Figure 4.9: (a) Effect of inter-rod magnetostatic interactions. The black loop (circles) is for two perpendicular noninteracting nanorods (with neither exchange, nor magnetostatics between rods) and the green loop is for nanorods interacting magnetostatically only. In panel (b) nanorods interact magnetostatically and inter-rod exchange is $A_{\mathrm{r-r}} = xA(b)$, with $x = 0$ for the blue curve (triangles), 0.05 for the red curve (circles) and 0.5 for the green curve (squares). The two parallel nanorods are in contact with their largest faces and the center-to-center distance is 6.7 nm. Panel (c), as in (b), except a smaller face is shared, and center-to-center distance is 20 nm. In this case, increasing x does not result in a larger loop area.

Bibliography

[1] R. Behbahani, M. L. Plumer, and I. Saika-Voivod. Coarse-graining in micromagnetic simulations of dynamic hysteresis loops. *J. Phys. Condens. Matter*, 32(35): 35LT01, 2020.

[2] G. Grinstein and R. H. Koch. Coarse graining in micromagnetics. *Phys. Rev. Lett.*, 90(20):207201, 2003.

[3] C. L. Dennis, A. J. Jackson, J. A. Borchers, P. J. Hoopes, R. Strawbridge, A. R. Foreman, J. Van Lierop, C. Grüttner, and R. Ivkov. Nearly complete regression of tumors via collective behavior of magnetic nanoparticles in hyperthermia. *Nanotechnology*, 20(39):395103, 2009.

[4] M. J. Donahue and D. G. Porter. *OOMMF User's Guide, Version 1.0, Interagency Report NISTIR 6376*. National Institute of Standards and Technology, Gaithersburg, MD, Sept 1999. URL `https://math.nist.gov/oommf/`.

[5] G. Shi, R. Takeda, S. B. Trisnanto, T. Yamada, S. Ota, and Y. Takemura. Enhanced specific loss power from Resovist® achieved by aligning magnetic easy axes of nanoparticles for hyperthermia. *J. Magn. Magn. Mater.*, 473:148–154, 2019.

[6] J. Pearce, A. Giustini, R. Stigliano, and P. J. Hoopes. Magnetic heating of nanoparticles: the importance of particle clustering to achieve therapeutic temperatures. *J. Nanotechnol. Eng. Med.*, 4(1):011005, 2013.

[7] C. Munoz-Menendez, D. Serantes, J. M. Ruso, and D. Baldomir. Towards improved magnetic fluid hyperthermia: major-loops to diminish variations in local heating. *Phys. Chem. Chem. Phys.*, 19(22):14527–14532, 2017.

[8] B. Mehdaoui, R. P. Tan, A. Meffre, J. Carrey, S. Lachaize, B. Chaudret, and M. Respaud. Increase of magnetic hyperthermia efficiency due to dipolar interactions in low-anisotropy magnetic nanoparticles: Theoretical and experimental results. *Phys. Rev. B*, 87(17):174419, 2013.

[9] C. L. Dennis and R. Ivkov. Physics of heat generation using magnetic nanoparticles for hyperthermia. *Int. J. Hyperth.*, 29(8):715–729, 2013.

[10] P. Allia, G. Barrera, and P. Tiberto. Nonharmonic driving fields for enhancement of nanoparticle heating efficiency in magnetic hyperthermia. 12(3):034041, 2019.

[11] D. Chang, M. Lim, J. A. Goos, R. Qiao, Y. Y. Ng, F. M. Mansfeld, M. Jackson, T. P. Davis, and M. Kavallaris. Biologically targeted magnetic hyperthermia: Potential and limitations. *Front. Pharmacol.*, 9, 2018.

[12] B. Thiesen and A. Jordan. Clinical applications of magnetic nanoparticles for hyperthermia. *Int. J. Hyperth.*, 24(6):467–474, 2008.

[13] T. Sadhukha, T. S. Wiedmann, and J. Panyam. Inhalable magnetic nanoparticles for targeted hyperthermia in lung cancer therapy. *Biomaterials*, 34(21):5163–5171, 2013.

[14] N. A. Usov and B. Y. Liubimov. Dynamics of magnetic nanoparticle in a viscous liquid: Application to magnetic nanoparticle hyperthermia. *J. Appl. Phys.*, 112 (2):023901, 2012.

[15] K. Simeonidis, M. P. Morales, M. Marciello, M. Angelakeris, P. de La Presa, A. Lazaro-Carrillo, A. Tabero, A. Villanueva, O. Chubykalo-Fesenko, and D. Serantes. In-situ particles reorientation during magnetic hyperthermia application: Shape matters twice. *Sci. Rep.*, 6:38382, 2016.

[16] M. Anand, J. Carrey, and V. Banerjee. Spin morphologies and heat dissipation in spherical assemblies of magnetic nanoparticles. *Phys. Rev. B*, 94(9):094425, 2016.

[17] P. Torche, C. Munoz-Menendez, D. Serantes, D. Baldomir, K. L. Livesey, O. Chubykalo-Fesenko, S. Ruta, R. Chantrell, and O. Hovorka. Thermodynamics of interacting magnetic nanoparticles. *Phys. Rev. B*, 101(22):224429, 2020.

[18] D. Serantes, K. Simeonidis, M. Angelakeris, O. Chubykalo-Fesenko, M. Marciello, M. D. P. Morales, D. Baldomir, and C. Martinez-Boubeta. Multiplying magnetic hyperthermia response by nanoparticle assembling. *J. Phys. Chem. C*, 118(11): 5927–5934, 2014.

[19] J. S. Anandhi, G. A. Jacob, and R. J. Joseyphus. Factors affecting the heating efficiency of Mn-doped Fe_3O_4 nanoparticles. *J. Magn. Magn. Mater.*, page 166992, 2020.

[20] G. T. Landi. Role of dipolar interaction in magnetic hyperthermia. *Phys. Rev. B*, 89(1):014403, 2014.

[21] C. Haase and U. Nowak. Role of dipole-dipole interactions for hyperthermia heating of magnetic nanoparticle ensembles. *Phys. Rev. B*, 85(4):045435, 2012.

[22] D. Cabrera, A. Coene, J. Leliaert, E. J. Artés-Ibáñez, L. Dupré, N. D. Telling, and F. J. Teran. Dynamical magnetic response of iron oxide nanoparticles inside live cells. *ACS Nano*, 12(3):2741–2752, 2018.

[23] K. Wu and J.-P. Wang. Magnetic hyperthermia performance of magnetite nanoparticle assemblies under different driving fields. *AIP Adv.*, 7(5):056327, 2017.

[24] L. Lopez-Diaz, D. Aurelio, L. Torres, E. Martinez, M. A. Hernandez-Lopez, J. Gomez, O. Alejos, M. Carpentieri, G. Finocchio, and G. Consolo. Micromagnetic simulations using graphics processing units. *J. Phys. D*, 45(32):323001, 2012.

[25] M. Kapoor, X. Shen, and R. H. Victora. Effect of intragranular exchange on exchange-coupled composite media. *J. Appl. Phys.*, 99(8):08Q902, 2006.

[26] A. J. Newell, W. Williams, and D. J. Dunlop. A generalization of the demagnetizing tensor for nonuniform magnetization. *J. Geophys. Res. Solid Earth*, 98 (B6):9551–9555, 1993.

[27] A. Aharoni. Demagnetizing factors for rectangular ferromagnetic prisms. *J. Appl. Phys.*, 83(6):3432–3434, 1998.

[28] O. Lemcke. *ThetaEvolve for OOMMF release 1.2a3*, February 2004. `http://www.nanoscience.de/group_r/stm-spstm/projects/temperature/download.shtml`. See also `https://math.nist.gov/oommf/contrib/oxsext/oxsext.html`.

[29] B. D. Cullity and C. D. Graham. *Introduction to magnetic materials*. John Wiley & Sons, 2011.

[30] T. L. Gilbert. A phenomenological theory of damping in ferromagnetic materials. *IEEE Trans. Magn.*, 40(6):3443–3449, 2004.

[31] W. F. Brown Jr. Thermal fluctuations of a single-domain particle. *Phys. Rev.*, 130(5):1677, 1963.

[32] S. Serrano-Guisan, H.-C. Wu, C. Boothman, M. Abid, B. S. Chun, I. V. Shvets, and H. W. Schumacher. Thickness dependence of the effective damping in epitaxial Fe_3O_4/MgO thin films. *J. Appl. Phys.*, 109(1):013907, 2011.

[33] M. L. Plumer, J. van Lierop, B. W. Southern, and J. P. Whitehead. Micromagnetic simulations of interacting dipoles on an fcc lattice: application to nanoparticle assemblies. *J. Phys. Condens. Matter*, 22(29):296007, 2010.

[34] N. A. Usov. Low frequency hysteresis loops of superparamagnetic nanoparticles with uniaxial anisotropy. *J. Appl. Phys.*, 107(12):123909, 2010.

[35] K.-J. Lee, A. Deac, O. Redon, J.-P. Nozieres, and B. Dieny. Excitations of incoherent spin-waves due to spin-transfer torque. *Nat. Mater.*, 3(12):877, 2004.

[36] S. Dutz and R. Hergt. Magnetic nanoparticle heating and heat transfer on a microscale: basic principles, realities and physical limitations of hyperthermia for tumour therapy. *Int. J. Hyperth.*, 29(8):790–800, 2013.

[37] N. A. Usov, S. A. Gudoshnikov, O. N. Serebryakova, M. L. Fdez-Gubieda, A. Muela, and J. M. Barandiarán. Properties of dense assemblies of magnetic nanoparticles promising for application in biomedicine. *J. Supercond. Nov. Magn.*, 26(4):1079–1083, 2013.

[38] F. Heider and W. Williams. Note on temperature dependence of exchange constant in magnetite. *Geophys. Res. Lett.*, 15(2):184–187, 1988.

[39] J. S. Kouvel. Specific heat of a magnetite crystal at liquid helium temperatures. *Phys. Rev.*, 102(6):1489, 1956.

[40] B. M. Moskowitz and S. L. Halgedahl. Theoretical temperature and grain-size dependence of domain state in x= 0.6 titanomagnetite. *J. Geophys. Res. Solid Earth*, 92(B10):10667–10682, 1987.

[41] M. L. Glasser and F. J. Milford. Spin wave spectra of magnetite. *Phys. Rev.*, 130(5):1783, 1963.

[42] C. M. Srivastava, G. Srinivasan, and N. G. Nanadikar. Exchange constants in spinel ferrites. *Phys. Rev. B*, 19(1):499, 1979.

[43] C. M. Srivastava and R. Aiyar. Spin wave stiffness constants in some ferrimagnetics. *J. Phys. C: Solid St. Phys.*, 20(8):1119, 1987.

[44] M. Uhl and B. Siberchicot. A first-principles study of exchange integrals in magnetite. *J. Phys. Condens. Matter*, 7(22):4227, 1995.

[45] K. Abe, Y. Miyamoto, and S. Chikazumi. Magnetocrystalline anisotropy of low temperature phase of magnetite. *J. Phys. Soc. Jpn.*, 41(6):1894–1902, 1976.

[46] R. Řezníček, V. Chlan, H. Štěpánková, P. Novák, and M. Maryško. Magnetocrystalline anisotropy of magnetite. *J. Phys. Condens. Matter*, 24(5):055501, 2012.

[47] H. Shokrollahi. A review of the magnetic properties, synthesis methods and applications of maghemite. *J. Magn. Magn. Mater.*, 426:74–81, 2017.

[48] R. Hergt and S. Dutz. Magnetic particle hyperthermia—biophysical limitations of a visionary tumour therapy. *J. Magn. Magn. Mater.*, 311(1):187–192, 2007.

[49] H. A. Albarqi, L. H. Wong, C. Schumann, F. Y. Sabei, T. Korzun, X. Li, M. N. Hansen, P. Dhagat, A. S. Moses, O. Taratula, and O. Taratula. Biocompatible nanoclusters with high heating efficiency for systemically delivered magnetic hyperthermia. *ACS Nano*, 13(6):6383–6395, 2019.

[50] X. Feng and P. B. Visscher. Coarse-graining Landau–Lifshitz damping. *J. Appl. Phys.*, 89(11):6988–6990, 2001.

[51] M. Kirschner, T. Schrefl, F. Dorfbauer, G. Hrkac, D. Suess, and J. Fidler. Cell size corrections for nonzero-temperature micromagnetics. *J. Appl. Phys.*, 97(10): 10E301, 2005.

[52] M. Kirschner, T. Schrefl, G. Hrkac, F. Dorfbauer, D. Suess, and J. Fidler. Relaxation times and cell size in nonzero-temperature micromagnetics. *Physica B Condens. Matter*, 372(1-2):277–281, 2006.

[53] P. Bažant and B. H. Oh. Efficient numerical integration on the surface of a sphere. *ZAMM-J. Appl. Math. Mech./Zeitschrift für Angewandte Mathematik und Mechanik*, 66(1):37–49, 1986.

[54] H. Fukushima, Y. Nakatani, and N. Hayashi. Volume average demagnetizing tensor of rectangular prisms. *IEEE Trans. Magn.*, 34(1):193–198, 1998.

[55] A. F. Bakuzis, L. C. Branquinho, L. Luiz e Castro, M. T. de Amaral e Eloi, and R. Miotto. Chain formation and aging process in biocompatible polydisperse ferrofluids: Experimental investigation and Monte Carlo simulations. *Adv. Colloid Interface Sci.*, 191:1–21, 2013.

[56] J. Leliaert, A. Vansteenkiste, A. Coene, L. Dupré, and B. Van Waeyenberge. Vinamax: a macrospin simulation tool for magnetic nanoparticles. *Med. Biol. Eng. Comput.*, 53(4):309–317, 2015.

Chapter 5

Micromagnetic simulation of clusters of nanoparticles

This chapter represents the first draft of a planned manuscript for journal submission.

Abstract

We employ a previously developed coarse-graining method based on the renormalization (RG) group for simulating clusters of iron oxide nanoparticles (NPs) composed of nanorods. To study the heating performance of aggregates of magnetic NPs, we focus on the dynamic hysteresis loops of clusters of immobile NPs in chains, triangular lattices and in an FCC structure. We employ a previously introduced RG-based coarse-graining along with a time scaling based on the sweep rate of the external AC field and damping constant in the Landau-Lifshitz-Gilbert equation, which enables relatively fast simulations of dynamic hysteresis loops of multiple 50-nm NPs at finite temperature using hyperthermia-relevant sweep rates. In simulating clusters of

magnetic particles, we examine the macrospin (MS) model introduced, which is an approximation for generating equivalent hysteresis loops as a NP with the same coercivity H_c and remanent magnetization M_r, to study if this approximation is valid for simulating cluster of NPs. We change the strength of magnetostatic interactions between NPs by fixing the NPs at different distances, and study their magnetization dynamics in the various geometries. We also calculate the local hysteresis loops of individual MSs in a cluster to understand the impact of the geometry of their neighbours on their magnetic response.

5.1 Introduction

Magnetic nanoparticles (MNPs) have attracted much attention due to their wide range of potential applications [1, 2]. Among their biomedical applications, MNP hyperthermia is a novel developing method that uses NPs for cancer treatment by taking advantage of their heating upon exposure to an alternating external magnetic field [3–7]. Along with pre-clinical experiments [8–11], computer simulations of MNPs are used to better understand the details of the heating process [12–23], which lights the path for further experiments and more efficient cancer treatment. Magnetic heating of immobile NPs through Néel relaxation is quantified by their magnetization-field (MH) hysteresis loop area. We seek to calculate the hysteresis loop of multiple $6z4y$ magnetite NPs composed of ten nanorods ordered with six along the z axis and four along the y axis. The simulation model is motivated by a successful pre-clinical study of magnetite NPs for breast cancer treatment in mice [8].

Micromagnetic simulations of MNPs is a common numerical method that uses the Landau-Lifshitz-Gilbert (LLG) equation for describing the magnetization dynamics of

NPs. When the particle size decreases to the nanometer range, thermal fluctuations play a key role in the magnetization dynamics and micromagnetic simulations of NPs (in that thermal energy becomes of the same order as the energy barrier to magnetization flipping; see Eq. 1.6). Using uniformly magnetized cells with the same size as atomic unit cells can be computationally very expensive. To solve the problem of expensive calculations, using fewer but larger simulation cells for describing NPs is favorable. Different methods have been prescribed for scaling the magnetic parameters to provide results invariant with simulation cell size [24–27].

In two recent works [28, 29] (hereafter referred to as I and II), we implemented, amended and extended a renormalization group (RG) scaling approach introduced by Grinstein and Koch [27] for our model of dynamic hysteresis loops at 310 K to include magnetostatic interactions in addition to the initially considered interactions of magnetic field, exchange and magnetocrystalline anisotropy. In these works we showed that the RG scaling works properly for simulating fixed-volume nanorods over a range of cell sizes ($a = ba_0$), from $b = 1$ corresponding to the atomic unit cell size when a nanorod is made 10752 cells to $b = 22$ where a single block represents a nanorod. We also tested the scaling method for stacks of nanorods and showed that it is valid for simulating multiple nanorods with cell sizes as big as $a = 8a_0$. Employing the RG scaling method for simulating complex NPs enabled further investigations on a macrospin (MS) model to find the effective magnetization and uniaxial anisotropy of a same-volume MS with equal coercivity H_c and remanent magnetization M_r in MH hysteresis loops as a complex NP. The MS model is an approximation in which the collective effects of exchange interactions, magnetocrystalline anisotropy and self-demagnetization in a complex NP are captured with a single effective magnetization vector subject to uniaxial anisotropy, and can speed up the calculations remarkably. The next step in evaluating the MS model is to compare the heating performance of a

system of multiple NPs with a corresponding system of MSs. We showed in II that for two NPs at different separations, the hysteresis loops match those of the MS's beyond a centre-to-centre distance of 1.5 times the particle diameter. Our work also makes use of an approximate invariance of hysteresis loops under an increase in AC field sweep rate when the damping constant α in the LLG equation increases commensurately, which also reduces computational time.

Here we employ our previous methods and extend the investigations to the MS model for clusters of NPs. The first objective of this study is to examine the MS model with two perpendicular uniaxial anisotropies to get a better approximation for the complex NP's hysteresis loop. Also, we assign the direction of anisotropy axes of simulation cells from a distribution to mimic the effect of variations in magnetic parameters in real systems, and study the impact on the hysteresis loop. The second goal is to simulate clusters of NPs and compare the heating performance of complex NPs with the MS model at different particle separations. The third goal is to study the local loop of individual MSs in clusters to understand their heating mechanism under the effect of interparticle interactions. In the end, we explore the SR/α scaling for multiple NP simulations with the OOMMF [30] and Vinamax [31] software used in this study.

Different studies have looked into NPs clustering in a variety of arrangements as chains, rings, cubes, FCC, 2D hexagonal lattice, spheres or disordered structures and investigated their heating behavior under variation of various quantities [12, 14, 15, 18, 21, 23, 32–36]. For example, Anand [14] used Monte Carlo simulations to study the effect of dipole interactions on the heating efficiency of a chain of NPs when their uniaxial anisotropy axes make an angle θ with respect to the chain axis. He concluded that strong dipole interactions tend to align the NPs' magnetization parallel to the

chain axis, even when $\theta = 90°$. Valdes et al. [21] examined the effect of dipolar interactions on the heating efficiency of NP chains with different lengths when each particle's effective anisotropy axis is along the chain axis. They concluded that the chain formation of NPs could improve heating performance even if the chains are not aligned with respect to one another. Anand et al. [32] explored the heating behavior of micron-sized spherical clusters of NPs by changing the amplitude and frequency of the applied field. They reported different heating behavior for the core and surface NPs, which highly depends on the field parameters used. Serantes et al. [23] studied the effect of dipole interactions in clusters of NPs in the form of chains, 2D hexagonal lattices, cubes and rings. They reported a positive effect of dipole interactions on heating performance when NPs formed chains, in contrast to the negative effect when the NPs were found in other studied assemblies, although the beneficial effect tapered off once chains exceeded eight NPs in length. All of these studies assumed the MS model for the NPs. One goal of the present work is to examine the impact of internal structure on the relevant hysteresis loops.

While evaluating the heating efficiency of NP clusters is commonly done based on their collective heating, experimental studies reported cases of effective MNP therapies without a global rise in temperature [5, 37]. This can be attributed to the fast temperature drop of the surrounding tissue within a short distance (~ 10 nm) from the NP surface [38]. Although there are many unsolved questions on the ultimate reasons and mechanism of death in cancerous cells through magnetic nanoparticle hyperthermia (MNH), different studies investigated the local heating of NPs in clusters to try to understand the process [12, 13]. The present work addresses this issue for a number of different NP cluster geometries.

This paper is organized as follows. Our model is described in section 5.2. In

section 5.3, we explore the use of two anisotropy axes in the MS model in describing complex NPs, and quantify the effect of varying the distribution of (single) anisotropy directions on hysteresis loops. In section 5.4 we simulate three NPs in chain and triangular arrangements, and 13 NPs in an FCC structure. In section 5.5 MSs' local loop are studied. Section 5.6 tests the equivalence of simulation results when the ratio of the AC field sweep rate SR to damping constant α is held fixed for multiple particles. Finally, we report our conclusions in section 5.7.

5.2 The model

Our goal is to simulate iron oxide NPs composed of magnetite (Fe_3O_4) or maghemite (γ-Fe_2O_3) nanorods corresponding to MNPs used in an experimental study by Dennis et al. [8]. Among different possible assemblies of nanorods to make up NPs, we studied three combinations of parallel and perpendicular arrangements of increasing orientational order labelled $6z4y$, $8z2y$ and $10z$ in II, and here we use the $6z4y$ structure to explore clusters of NPs. Magnetite and maghemite, the most common candidate for MNH, are two iron oxides that the US Food and Drug Administration and European Medicine Agency approved for medical usage [39]. They have similar magnetic parameters except their magnetocrystalline anisotropy that is cubic in Fe_3O_4 and uniaxial in γ-Fe_2O_3.

For simulating complex NPs composed of ten nanorods with dimensions 6.7 nm$\times$ 20 nm$\times$ 47 nm, we used the OOMMF [30] software package and its Theta Evolve module [40] for finite temperature calculations. In micromagnetics, instead of simulating individual atomic spins, a magnetization vector represents the collective behavior of the spins in a simulation cell of size a, which is usually larger than the atomic unit

cell size a_0. In I and II, we explored an RG-based scaling approach for simulating fix-volume nanorods using fewer but larger cells (with size $a = ba_0$, $b > 1$), and here we employ the same approach for simulating clusters of multiple NPs. The LLG equation describes the magnetization dynamics of simulation cells and involves a damping constant α that quantifies the energy dissipation as the magnetic moments precess about the effective field, which is the sum of different contributions, such as the external magnetic field (Zeeman) and the effective fields arising from magnetocrystalline anisotropy, exchange, magnetostatics and temperature (stochastic thermal field). In magnetic hyperthermia, to control the unwanted heating of healthy tissue through eddy currents, the frequency f and amplitude $H_{\max}$ of the applied magnetic field should be chosen so that sweep rate (SR) of changing field be less than a threshold, i.e. SR $= 4fH_{\max} \leq 0.25$ Oe/ns [41, 42]. As we explored in I, equivalent hysteresis loops are achievable using faster SR for simulating nanorods, provided that the ratio SR/α remains constant. For the SR of 0.25 Oe/ns relevant to hyperthermia and an α of 0.1 for magnetite nanorods, the target ratio is SR/$\alpha = 2.5$. In this study, the NP simulations are performed in OOMMF with SR = 50 Oe/ns and $\alpha = 20$, preserving SR/$\alpha = 2.5$.

As in I and II, for simulating NPs with micromagentic cells of the same size as the crystalline unit cell ($a = a_0 = 0.839$ nm), we use magnetic parameters of bulk magnetite: saturation magnetization $M_{\mathrm{s}} = 480$ kA/m [42], and exchange constant $A_0 = 0.98 \times 10^{-11}$ J/m [43], which reproduces the experimental critical temperature of $T_c = 858$ K [44] by LLG simulations. Magnetite has cubic crystalline anisotropy, which we omit since it does not contribute significantly to hysteresis, especially given the relatively large shape anisotropy of the nanorods. For maghemite simulations, we include uniaxial anisotropy with energy density $K_0 = 10$ kJ/m^3[1]. Samples usually contain a mixture of both magnetite and maghemite [8], which one could simulate

with intermediate values of K_0. A $6z4y$ NP is made up of ten nanorods each with dimensions $8a_0 \times 24a_0 \times 56a_0$ and volume $V = 6350.0$ nm^3, with six of them lying along the z direction and four lying along the y direction. Using the modified RG-based coarse-graining procedure explained in I and II, we simulate NPs with micromagentic cells of side length $a = 4a_0$ (scaling parameter $b = 4$), and with scaled exchange, anisotropy and magnetostatic interactions at $T = 310$ K. Neighbouring cells on different nanorods interact via exchange with half the strength as cells within the same nanorod. We simulate using full magnetostatic interactions, including "self-demag" within cells. Including magnetostatics means that it is not necessary to include a non-zero value of K_0 for magnetite to approximate the effects of shape anisotropy.

To mimic lattice imperfections, for maghemite NP simulations, the anisotropy axes of cells is chosen within a 5° standard deviation around the long axes of the nanorods. Hysteresis loops are calculated by averaging over at least 100 independent runs, showing changes of the normalized magnetization component along the field $m_H = M(b)/M_\mathrm{s}$ in response to the external field $H(b) = H_\mathrm{max} \sin(2\pi f t)$.

We also use the MS models introduced in II, which refer to single-moment macrospins that exhibit dynamic hysteresis loops similar to those of NPs. The MS's effective magnetic parameters mimic effects of the NP's magnetic interactions and internal structure. In this study, we simulate clusters of $6z4y$ magnetite NPs in OOMMF and compare their hysteresis loops with clusters of equivalent MSs, using Vinamax [31] software, as it gives more flexibility in assigning the position of NPs in clusters. Owing to the smaller number of calculations for MSs, that interact just with dipole interactions, these hysteresis loop simulations can be performed directly with the clinically-relevant SR of 0.25 Oe/ns and with $\alpha = 0.1$.

The importance of coarse-graining is particularly pronounced when we model multiple NPs. For example, the simulation time for a cycle of AC field for 13 complex NPs in an FCC configuration, at the smallest nearest-neighbour separation, using OOMMF with $a = 4a_0$ cell size and SR = 25 Oe/ns, takes more than 16 days, whereas it takes around 11 s to simulate 13 MSs with SR = 0.25 Oe/ns, using Vinamax. This huge difference is due to various factors: the higher number of interactions required for modeling complex NPs compared to MSs; simulating the empty cells between NPs takes up some of the OOMMF simulation time, whereas this is not a consideration in Vinamax; and the small integration timestep of 10 fs required for the small cells used to model NPs compared to the time step of 1 ps for MSs. Without spatial coarse-graining, the simulation of complex NPs with OOMMF would take approximately $10 \times 4^3 = 640$ times as long (since a larger cell permits a longer time step).

5.3 Effective anisotropy in complex NPs

In II, we showed that a MS with $K_u = 4.80$ kJ/m^3 and $M_\mathrm{s} = 381.6$ kA/m exhibits a hysteresis loop with the same H_c and M_r as a same-volume $6z4y$ magnetite NP under a rotationally averaged field. But when the field is applied parallel to the z axis, MS's anisotropy should decrease to $K_u = 3.64$ kJ/m^3 along the field to produce an equivalent loop. Here, we continue our exploration to find a suitable anisotropy for MSs that provide equivalent hysteresis loops for different directions of the applied field for γ-Fe_2O_3 ($K_{u0} = 10$ kJ/m^3) and Fe_3O_4 ($K_{u0} = 0$) $6z4y$ NPs.

The internal structure of the $6z4y$ NP means that nanorod anisotropies are found to lie in both the z and y directions; modelling the MS with two anisotropy axes, along z and along y, may provide a route to finding a better quantitative match between

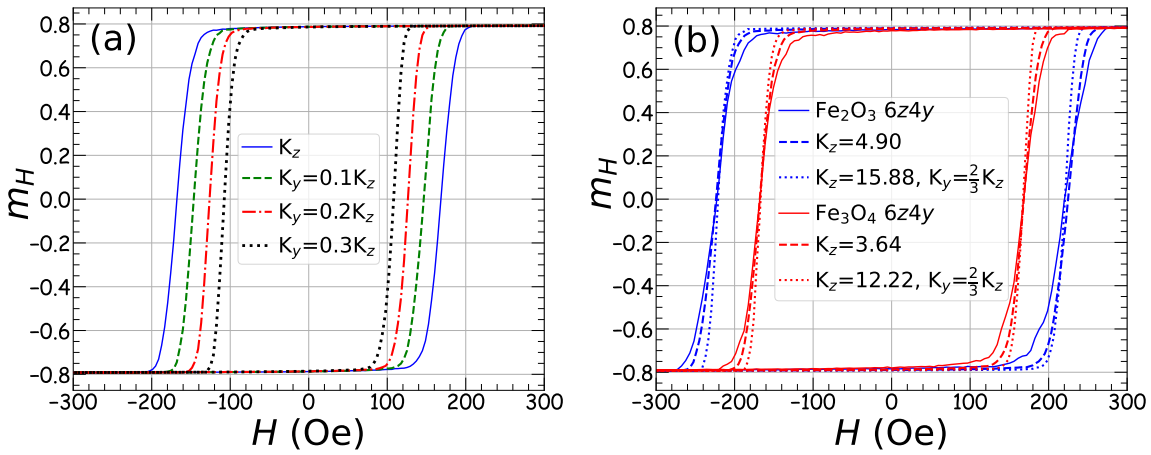

Figure 5.1: a) Changes to the hysteresis loop when a second anisotropy axis along the y direction with small strength K_y is added to a MS with $K_z = 3.64$ kJ/m^3 and $M_s = 381$ kA/m. b) Hysteresis loops for $6z4y$ NPs of Fe_3O_4 and γ-Fe_2O_3 and their equivalent MSs with single (dashed line) or double uniaxial anisotropies (dotted lines). The external field is along z for both panels.

MS and NP loops. As shown in Fig. 5.1a, simply adding K_y to the original K_z, even with a very small value, shrinks the hysteresis loop, which is not desired. Hence, for the assumption of having two perpendicular anisotropies with K_z and $K_y = 2K_z/3$ energy densities, analogous to ordering six nanorods along the z and four along the y axis, new parameters need to be used. As shown in Fig. 5.1b, the hysteresis loop of a $6z4y$ maghemite NP exposed to a field along the z axis (H_z), can be reproduced with a MS having either a single anisotropy $K_z = 4.90$ kJ/m^3 (dashed lines), or two perpendicular anisotropies with $K_z = 15.88$ kJ/m^3, $K_y = 2K_z/3$ (dotted line). Similarly, for a magnetite $6z4y$ NP, the best fit with only a z-axis anisotropy is with $K_z = 3.64$ kJ/m^3, whereas if $K_y = 2K_z/3$ is included, a value $K_z = 12.22$ kJ/m^3 works well.

To get better insight on the accuracy of replacing complex NPs with MSs using these anisotropy values, we compare the MS and NP loop areas upon tilting the field away from the z axis in the $z - y$ plane by an angle θ, as shown in the inset

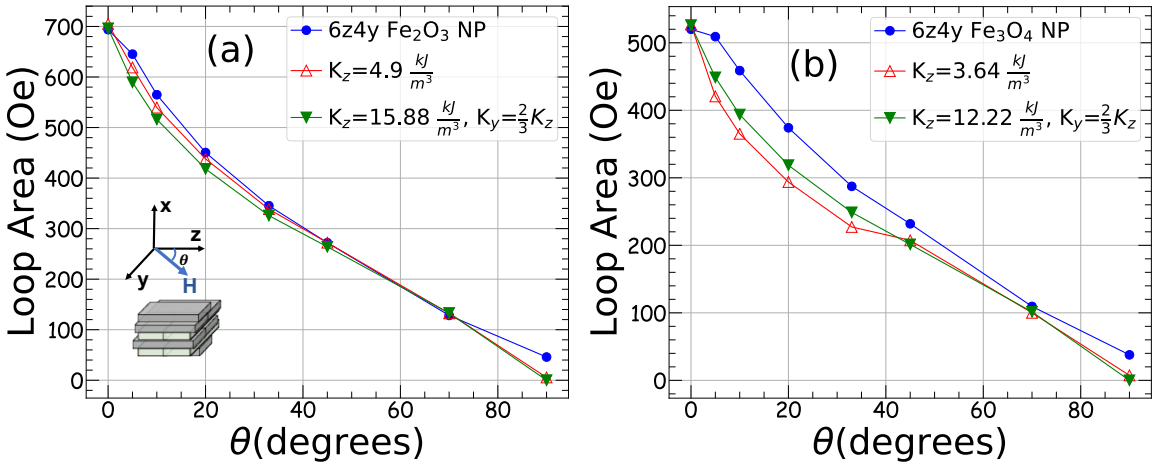

Figure 5.2: Hysteresis loop area changes as a function of applied field angle θ, see inset of panel (a), on $6z4y$ NPs and equivalent MSs with single and double uniaxial anisotropies for a) γ-Fe_2O_3 ($K_0 > 0$) and b) Fe_3O_4 ($K_0 = 0$) NPs.

of Fig. 5.2a. Comparing the loop areas for maghemite (Fig. 5.2a) and magnetite (Fig. 5.2b) NPs with respect to their equivalent MSs reveals that the presence of the magnetocrystalline anisotropy in maghemite encourages a closer match between complex NP and its equivalent MS. Also, adding the second anisotropy to a MS, slightly improves the loop area agreement for Fe_3O_4 when θ is in the range of $5 - 33°$ in contrast with γ-Fe_2O_3 that has a loop area closer to its single anisotropy MS. The relatively large value of K_z when two anisotropy axes are used is closer to that of the MS model of a single nanorod, and thus physically appealing. However, this larger value of K_z also likely causes the increased "squareness" in the shoulder area of the loops seen in Fig. 5.1 for the two-axes cases. Thus, further investigation into using two axes may prove to be fruitful, but it appears that there will be unavoidable trade-offs. For the remainder of this study, we employ only a single anisotropy axis in the MS models.

Real materials will have properties that vary depending on structural defects, chemical impurities, size polydispersity, and other forms of disorder. One way to

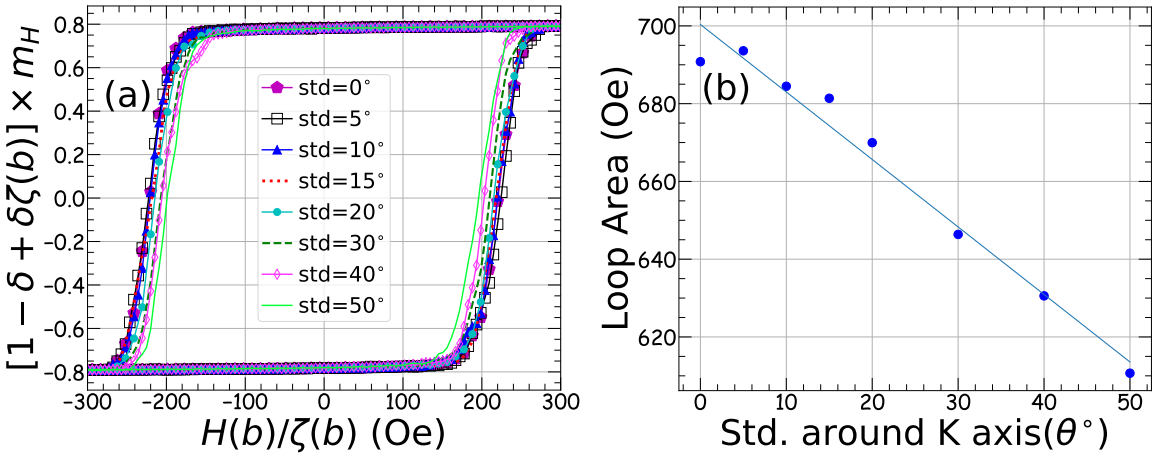

Figure 5.3: a) Hysteresis loops of $6z4y$ maghemite nanoparticles when the field is applied along the z axis, and the anisotropy axis of each cell has a random angular deviation from the long axis of the rod of which it is a part. The random angles are drawn from a normal distribution with zero mean and standard deviation (Std.) ranging from 0 to 50°. b) Loop area versus standard deviation of the anisotropy direction.

model such effects in simulations is to introduce distributions in micromagnetic cell properties [1]. While the relationships between the standard deviations of such distributions and the degree of various forms of disorder are often difficult to quantify, it is not uncommon to have variations of parameters in the range of 0 to 20% [6, 23]. Here, we simulate a $6z4y$ maghemite NP when each cell's anisotropy axis is chosen from a normal distribution around the direction given by the nanorod's longest edge. We vary the standard deviation (SD) of the distribution between 0 and 50 degrees and plot the resulting hysteresis loops. As shown in Fig. 5.3b, the loop area changes approximately linearly with the SD of the anisotropy axis direction with a slope of -1.74 Oe/degree and an intercept of 700 Oe. With SD = 10 degrees, the loop area is reduced by 1%, with SD = 20 it decreases by 3%, and with SD = 50 degrees it decreases by almost 12%. Thus we see that, for this system at 310 K, the effect of varying anisotropy directions is not very large.

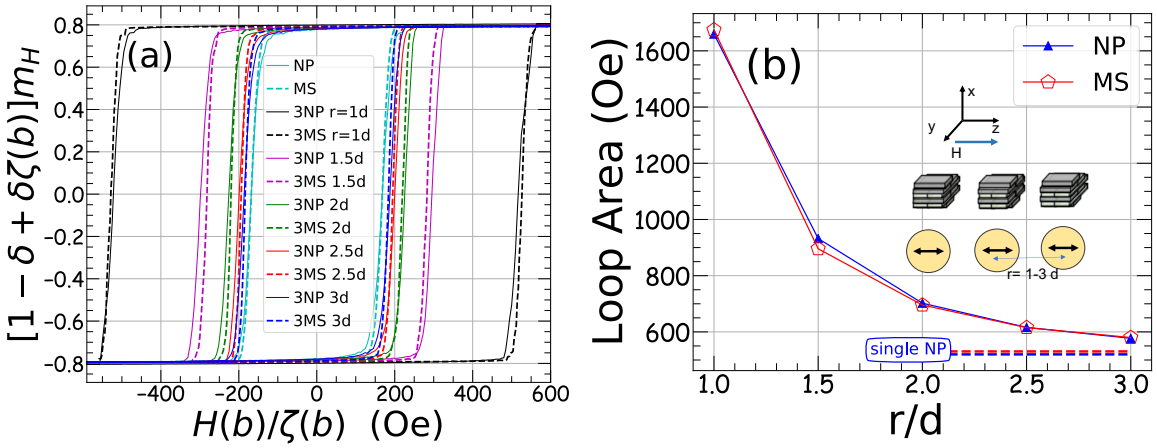

Figure 5.4: a) Hysteresis loops of three NPs and three MSs when their center-center distance varies from 1 - 3 NP-diameter (d). b) Loop areas vs center-center distance for three chained NPs and MSs as shown in the inset. The energy per loop per NP can be calculated via $E = \mu_0 M_s V_{NP} S_{loop}$.

5.4 Multiple NP heating efficiency

Our investigation on the heating efficiency of clusters of particles employs OOMMF software for simulating complex NPs and Vinamax for MSs. NPs are simulated using properties of magnetite ($M_s = 480$ kA/m, $K_u = 0$) with $6z4y$ internal structure and the equivalent MS has the same volume as ten nanorods ($\sim$ 50 nm size), uniaxial anisotropy of $K = 3.64$ kJ/m^3 and $M_s = 381.6$ kA/m. Because of the computational expense of simulating complex NPs, we use the time-scaling technique previously introduced in I and II and tested in Sec. 5.6, i.e. testing the equivalence of simulations done using SR = 50 Oe/ns and $\alpha = 20$ with those using SR = 0.25 Oe/ns and $\alpha = 0.1$.

5.4.1 Chained particles

Chains of NPs are the most common aggregation structure reported in simulation studies [12, 14, 21, 23]. We start with a chain of three particles and compare hysteresis loops of three complex magnetite NPs with three equivalent MSs. In addition to the

average hysteresis loop of particles at different center-center distances, a single NP and MS's loops are shown as benchmarks representing the limit of independent particles, i.e. when interactions have a negligible effect on the particle's magnetization response to the field. Corresponding loop areas are also calculated as a simpler metric of comparison. As shown in Fig. 5.4, the hysteresis loops corresponding to MSs are in reasonable agreement with those from NPs. The wider loops corresponding to the closer particles are a result of the effect of dipole interactions aligning the chain particles' magnetizations, in agreement with the results reported by Torche et al. [12], Anand [14], Valdes [21] and Serantes et al. [23]. Convergence of the loop area to the single NP or MS case implies that particles separated by more than 3 NP diameters (d), i.e., $r > 3d$, are approximately independent; see Fig. 5.4b.

5.4.2 Triangular order: when the internal structure matters

Serantes et al. [23] studied the heating efficiency of eight NPs in a hexagonal structure, which can be considered as an extended triangular cluster, and showed that dipole interactions diminish the hysteresis loop area compared to non-interacting particles. We consider here three NPs in triangular order when their center-center distance (r) varies relative to the NP diameter (d) and the applied field is along the z, parallel to the MS's uniaxial anisotropy and the $6z4y$ NP's shape anisotropy axis, as shown in the insets in Figs. 5.5a and b. The hysteresis loops, corresponding to the systems of three NPs on the vertices of an equilateral triangle with side lengths ranging from $r = d$ to $3d$ and similarly for three MSs with r between d and $4.5d$, and converging to the independent limit, are shown in Figs. 5.5a and b, respectively. The remarkable difference between the hysteresis loops of NPs and MSs for small r reveals that, for the triangular configuration, the combined effect of exchange and magnetostatics on spin

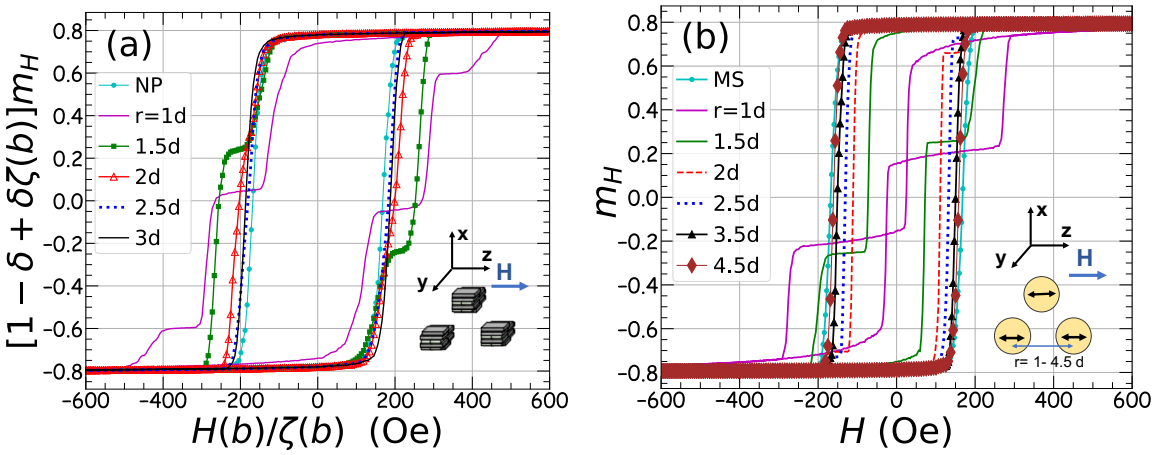

Figure 5.5: Hysteresis loops as a function of particle distances for systems of three interacting a) NPs b) MSs, on vertices of an equilateral triangle. d is a NP diameter and r is the particles center-center distance.

alignments of complex NPs is qualitatively different from that of dipole interactions for MSs, and results in significantly larger hysteresis loop areas for NPs compared to MSs. Fig. 5.6 displays the loop area as a function of particle distance, for the same arrangements considered in Figs. 5.5a and b. This serves to quantify the poor quality of the MS approximation, especially at small r. As expected, the loops converge to the single particle's as r grows.

Minimizing the energy of three dipoles on the vertices of a triangle in the absence of an external field shows that the lowest energy configuration is achieved when dipoles (magnetization vectors) make 120 degrees with respect to each other [45]. Fig. 5.7 compares the hysteresis loops of three NPs and MSs in triangular order when the MSs' anisotropy axes are aligned 120 degrees with respect to each other and when the effective anisotropy axes are along the field, with $r = 2.5d$, as shown in the insets. It is clear that the biggest loop area corresponds to three complex NPs with anisotropy aligned with the field. After that, the loop for three MSs with anisotropy axes along the external field has the second largest area, resulting from the larger spin alignment

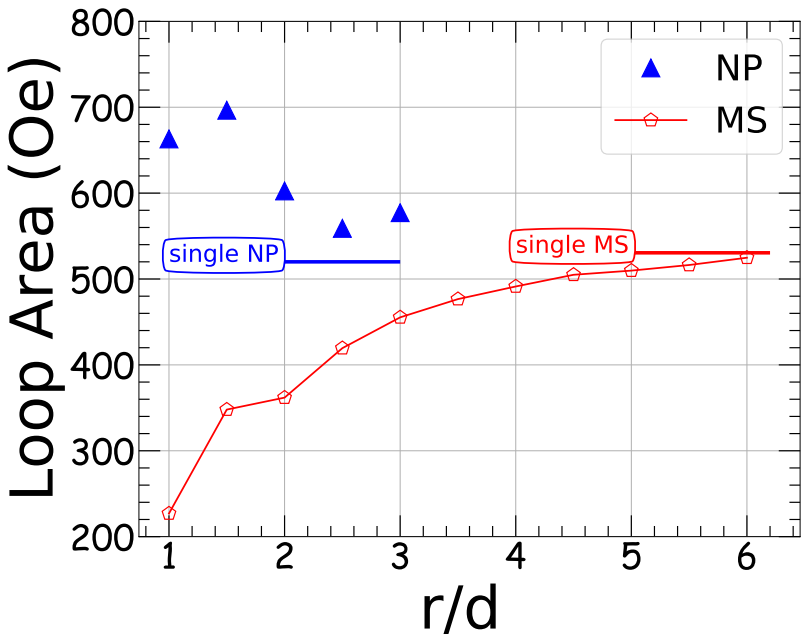

Figure 5.6: Loop area as a function of inter-particle distance (r) normalized with a NP diameter (d), for three NPs and MSs on vertices of an equilateral triangle.

to the anisotropy axes. The 120° alignment case exhibits the smallest area. As NPs are not fixed after injection into the body, the 120° configuration might be their preferred arrangement, and under application of an external field they may rearrange to align their anisotropy axes to the field. Different hysteresis loop areas for these cases reveal the necessity of more elaborate simulations that include particle rotation as well as their internal structure.

5.4.3 NPs in an FCC structure

Packed arrays of NPs in different arrangements such as spheres, cubes and FCC structures have been studied and reported in the literature [15, 18, 23, 32]. Fu et al. [18] investigated the dipole interaction effects on the heating performance of a cluster of 64 and 63 superparamagnets in simple cubic and FCC structures, respectively.

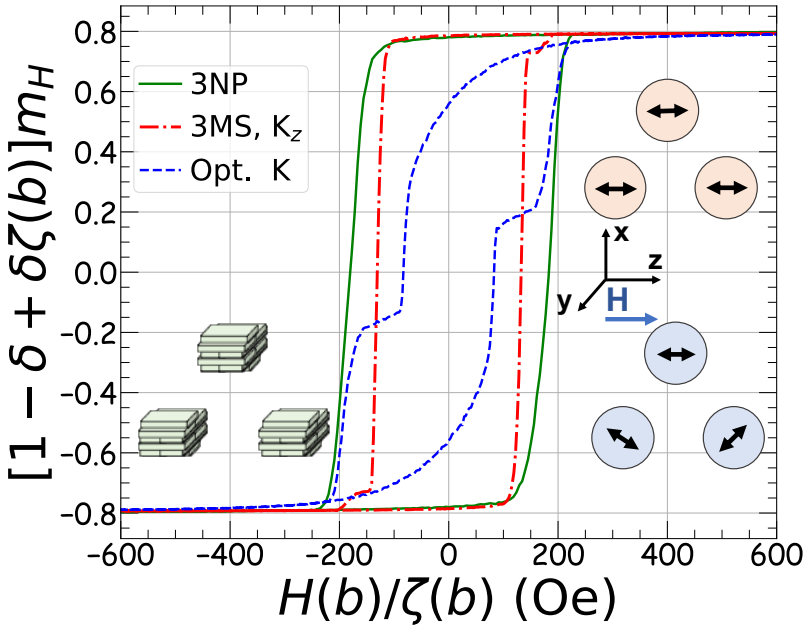

Figure 5.7: Comparison of NPs and MSs arranged in a triangle of side length $2.5d$. The green curve is the hysteresis loop for three $6z4y$ NPs, oriented as in the left inset. Black arrows represent the anisotropy axes in MSs. The dashed blue loop corresponds to assigning the MS anisotropy axes at 120° relative to each other (the lowest dipole energy arrangement at $H = 0$). The red dot-dashed loop corresponds to the case where the MS anisotropy axes are aligned with the field.

They introduced a concept called morphology anisotropy, which is defined in terms of the aspect ratio of the semi-axes of an ellipsoid which is equivalent to the cluster, and concluded that in the structures without morphology anisotropy the effect of dipole interaction is minimized and the cluster's loop area is almost the same as non-interacting particles. This can be interpreted to mean that the effect of dipole interactions is considerable so long as the cluster is extended in one direction, similar to a column of NPs. Serantes et al. [23] studied eight nanoparticles in a cubic structure and observed a negative effect of dipole interactions on their global heating compared to non-interacting nanoparticles, unlike in the case of chained particles, where dipolar interactions enhance heating. Here, by exploring the effect of dipolar interactions on the hysteresis loop at different inter-particle distances, we are comparing the response

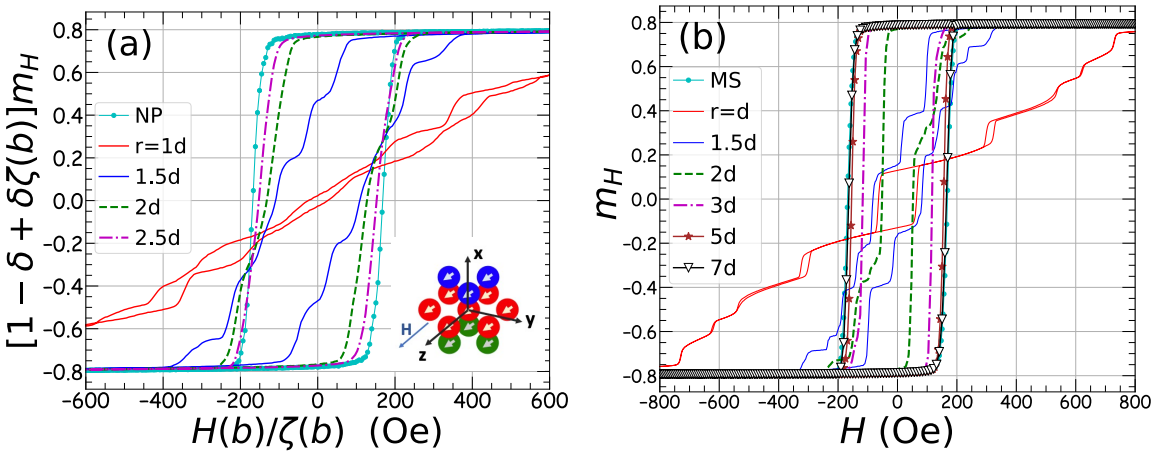

Figure 5.8: Hysteresis loops of particles on an FCC structure (as shown in the inset) containing 13 a) NPs, b) MSs, at different center-center distances. The effective anisotropy of particles is aligned to the applied field. White arrows show the effective anisotropy axes in magnetic particles.

of NPs and MSs in situations of the kind reported in Ref. [23]; however, they focus on eight MSs in various geometries, and at fixed inter-particle distance.

In this section, we simulate complex NPs and MSs in an FCC structure at different center-center distances. Figs. 5.8a and b exhibit the hysteresis loops of thirteen NPs and thirteen MSs in the FCC structure shown in the inset of panel (a). Similar to particles in the triangular order, the internal structure of the NP plays a role in determining the loop shape that is not accounted for by the equivalent MSs. Comparing the hysteresis loops in Fig. 5.8 shows that the biggest loop differences are related to smaller r when particles are closer to each other. For example, for $r = d$ and $1.5d$, the steeper slope of the loop in a cluster of MSs originates from bigger jumps in the total magnetization than in a cluster of NPs. This can be attributed to the fact that the smallest contribution due to each MS flip is more pronounced in the total magnetization of thirteen MSs compared to the smallest contributions from each simulation cell among 21840 cells in a cluster of NPs.

As shown in Fig. 5.9, changes of the hysteresis loop area with varying particle

distance implies that the intraparticle exchange and self-demag counteract some effects of the interparticle interactions, so that NPs further than $2.5d$ apart have a loop area close to a single NP's, whereas the role of dipole interaction between the MSs can not be ignored for $r < 5d$.

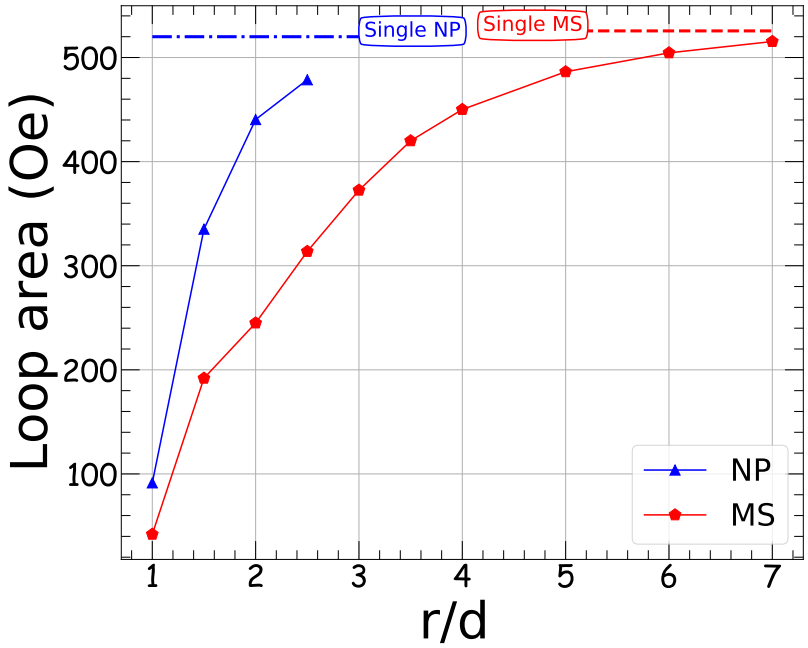

Figure 5.9: Loop area as a function of particle distance for clusters of complex NPs and MSs in an FCC structure.

5.5 Local vs global loops

Recent studies emphasize the importance of local heating of NPs in clusters rather than their collective (global) heating, as the temperature of the surrounding tissue is different in vicinity of the individual NPs [5, 37]. While exploring local hysteresis loops – those of individual NPs – is a good first step in understanding the distribution of heating near and within a collection of NPs, whether or not the individual loops represent actual heating of individual NPs is not obvious, especially when interacting

particles have inverted local loops [12, 13]. In this section, we explore the local hysteresis loops of individual MSs in collections of particles.

5.5.1 Chains and triangles

First, we consider clusters of three MSs as shown in Fig. 5.10. We use different line styles and colors to differentiate local loops. Furthermore, to make it clear when we have inverted loops, the portion of the magnetization curve corresponding to the first half of an AC field cycle, when the field decreases from $H_{\max}$ to $-H_{\max}$, is plotted with symbols; the magnetization curve for the second half of an AC field cycle, when the field increases from $-H_{\max}$ to $H_{\max}$, appears with no symbols.

As summarized in Fig. 1.4, as long as dipoles are parallel to the joining line (chain axis), the dipole energy is in favor of their head-to-tail alignment. In Fig. 5.10a, MS1 and MS3, the MSs at the two ends of the chain, feel the same dipole interaction, which is different from the net dipole field from MS1 and MS3 acting on the particle in the middle of the chain, MS2. The competition between dipole interactions, uniaxial anisotropy and Zeeman energy determines stable magnetic states and their dynamics. In this case, the difference in the dipole energy that the MSs at the ends and middle of the chain experience is not big enough compared to their anisotropy and Zeeman energy to cause different magnetization dynamics, as shown in Fig. 5.10a. When the chain is made of smaller NPs, due to the smaller volume-dependent anisotropy energy, this energy difference can be considerable and results in different local loops, as reported by Torche et al. [12].

In contrast, if our MSs are in a triangular arrangement, as in Fig. 5.10b, the magnetization of particles at the base (MS1, MS2) exhibit the same dynamics, which are very different from that of MS3. As mentioned before, the lowest energy arrangement

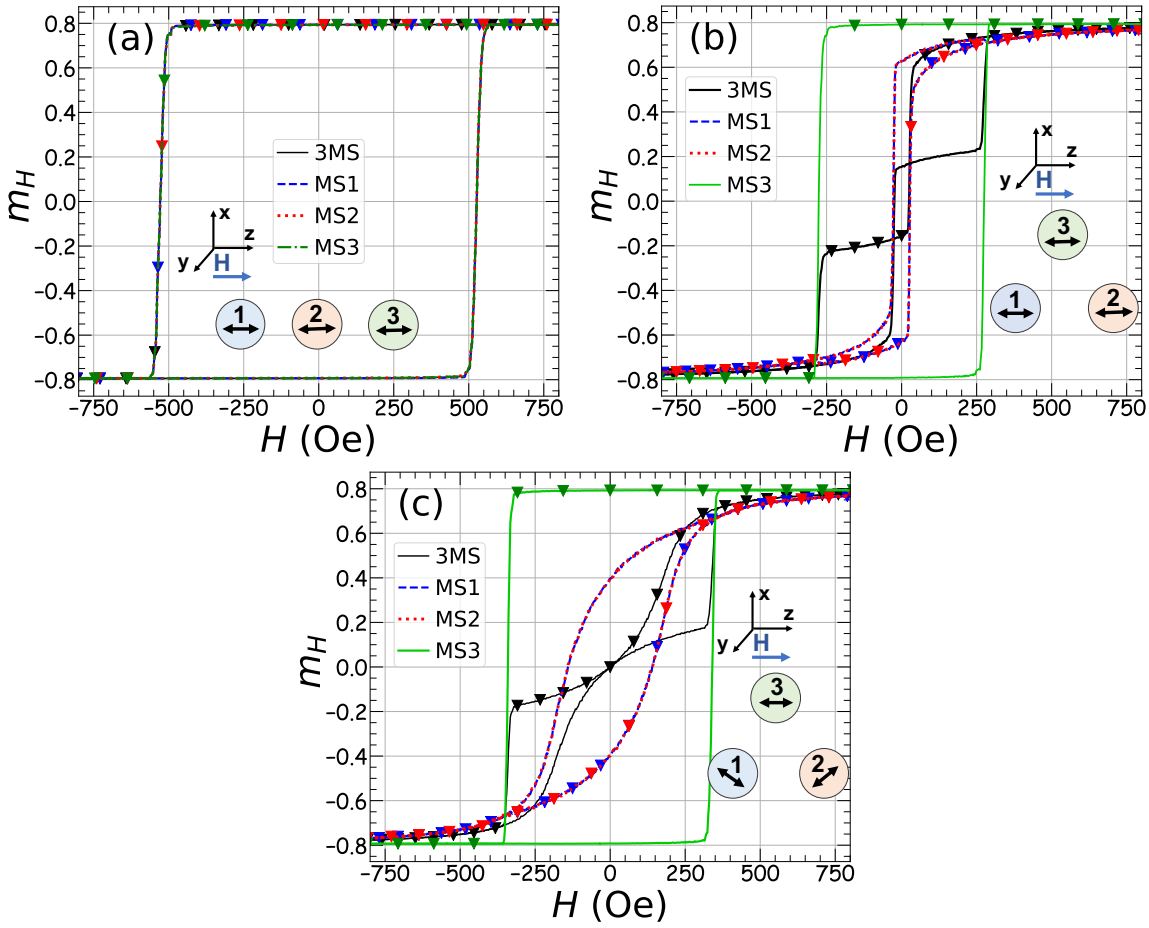

Figure 5.10: Comparing individual MSs' hysteresis loops with the global loop for three MSs ordered as a) a chain and b) a triangle with the anisotropy axes along the field, c) same as b except the anisotropy axes of the MSs make 120 degrees with each other. In all the arrangements MSs are at the closest distance to each other, $r = d$, $M_s = 381.6$ kA/m and $K = 3.64$ kJ/m^3. Filled triangles distinguish the magnetization changes at the first half of a cycle, i.e. when $H_{max} \to -H_{max}$. We get $M_s = 0.8$ as MS parameters are corresponding to its equivalent NP and the magnetization is scaled by 0.795.

at $H = 0$ and $K = 0$ with three dipoles in a triangle is when they make 120° with respect to each other. Starting from the highest spin alignment to the high external field in the z direction, as the field decreases the dipole fields tend to tilt MS1 and MS2 towards the 120° state and away from the z axis. When the field is very small, but still positive, the net effect of the Zeeman, anisotropy and, most importantly, dipole

interactions results in a magnetization flip of MS1 and MS2. The hysteresis loops of MS1 and MS2 in Fig. 5.10b are called "inverted" since the (positive) loop area implies that the NP is doing work on its surroundings and thus absorbing heat. Considering that a normal hysteresis loop is due to the delayed alignment of the magnetization with the applied field, an inverted loop occurs when a spin flips in advance of the external field changing direction. In the inverted case, a spin is "helped along" by the dipolar interactions of neighboring particles. MS3 exhibits a loop similar to that of an independent particle, but with a larger H_c arising from the dipolar interactions with MS1 and MS2. The average hysteresis loop of these MSs represents the global heating performance and is shown with a black curve in Fig. 5.10b, with an inverted middle portion.

Another triangular arrangement to study is one in which the MSs' anisotropy axes follow the alignment favored by dipole interactions, as shown in the inset of Fig. 5.10c. In this case, we see no sudden magnetization flips for MS1 and MS2 which means there is no energy barrier for dipoles to overcome to get to the global minimum energy state, i.e. MS1 and MS2 dipoles lie in positions with minimum energy during the entire field cycle. The loops for MS1 and MS2 are inverted from start to finish. Similar to the previous case, MS3 experiences competing interactions and undertakes a magnetization flip only when the external field overpowers the anisotropy and dipolar fields from MS1 and MS2. Put in another way, for the $H = 0$ and $K = 0$ ground state, if MS3 points along positive z, then MS1 and MS2 have negative z components, and this is what we see in the loop for decreasing H at $H = 0$; the inverted loops are a reflection of the dipolar ground state. In this ground state configuration, the dipolar field due to MS1 and MS2 at MS3 has a component in the z direction, and this tends to counteract the increasingly negative H, resulting in a much wider loop for MS3 than expected from anisotropy alone. The average of the local loops results in a global

loop with 21% smaller area compared to the previous ordering with anisotropies along the z-axis.

Munoz et al. [13] has a detailed discussion about how local hysteresis loops of interacting NPs do not represent their heating because particles exchange work with their neighbours through dipole interactions. They calculated local heating by considering the dynamical process of energy dissipation through the damping torque. We note that the loops that we have presented thus far are calculated with respect to the external field alone, and not with respect to the local field (the effective field) acting on an individual NP. Calculating such loops may help us bridge the insights from Munoz et al's dynamical theory and local heating based on a thermodynamic description.

5.5.2 FCC structure

Different dynamics of MSs in a triangular order encourages us to look at the local loops for MSs in the FCC structure. A labeled model of MSs and their local loops for nearest neighbour distance $r = d$ and $1.5d$ are shown in Fig. 5.11 and 5.12, respectively, with the MSs' uniaxial anisotropy and applied field both along the z axis.

Spatial coordinates of the MSs in FCC structure are reported in Table. 5.1 as a function of r. Owing to the symmetries of the structure, some sites should have identical loops, which are plotted in the same panel in Figs. 5.11 and 5.12. As in Fig. 5.10, magnetization changes through a decreasing field half cycle are distinguished with filled symbols on the hysteresis loops and each loop is calculated via averaging over 1000 independent field cycles.

Table 5.1: Particle coordinates at FCC structure as a function of r, which is the nearest neighbor center-center distance, $x = r/\sqrt{3}$ and $\theta = \sin^{-1}(1/\sqrt{3})$. Colors refer to Fig. 5.11.

MS No.	x	y	z	color
1	0	0	0	pink
2	0	0	r	pink
3	0	0	$-r$	pink
4	0	$r\sin(\pi/3)$	$r\cos(\pi/3)$	pink
5	0	$-r\sin(\pi/3)$	$-r\cos(\pi/3)$	pink
6	0	$r\sin(\pi/3)$	$-r\cos(\pi/3)$	pink
7	0	$-r\sin(\pi/3)$	$r\cos(\pi/3)$	pink
8	$r\cos(\theta)$	$r\sin(\theta)\sin(\pi/6)$	$r\sin(\theta)\cos(\pi/6)$	blue
9	$r\cos(\theta)$	$r\sin(\theta)\sin(\pi/6)$	$-r\sin(\theta)\cos(\pi/6)$	blue
10	$r\cos(\theta)$	$-r\sin(\theta)$	0	blue
11	$-r\cos(\theta)$	$r\sin(\theta)$	0	green
12	$-r\cos(\theta)$	$-r\sin(\theta)\sin(\pi/6)$	$r\sin(\theta)\cos(\pi/6)$	green
13	$-r\cos(\theta)$	$-r\sin(\theta)\sin(\pi/6)$	$-r\sin(\theta)\cos(\pi/6)$	green

As shown in Fig. 5.11a, the central particle MS1 is the symmetry center of the structure with the same distance from 12 neighbouring MSs. When $r = d$, the effect of neighbouring dipoles on MS1 results in a sudden magnetization flip at a small coercivity (H_c); see Fig. 5.11b. The average of individual local loops results in the global hysteresis with small area, small H_c and M_r. As shown in the labeled model in Fig. 5.11a, MS2 and MS3 have equivalent positions and exhibit similar dynamics. Their hysteresis loops have the same H_c as MS1 but smaller M_r, as shown in Fig. 5.11c. MS4-MS6 and MS5-MS7 are two other pairs of MSs exhibiting similar magnetization dynamics with inverted loops. The slight difference in the two pairs' hysteresis in the low field range is attributed to the finite number of instances averaged over in each loop calculation; see Fig. 5.11d and e. Moreover, the positions of MS8-MS9 and MS12-MS13 are also symmetric; therefore, they have similar local loops with a slight difference in the low field range, which is expected to vanish upon increasing the number of samples in the loop averaging calculations; see Fig. 5.11f and h. MS10

and MS11 are the last equivalent pair, having opposite magnetization dynamics and loop areas (one is positive, one is negative); see Fig. 5.11g.

Looking at the locations of the MSs with inverted loops, i.e., MS4, MS5, MS6 and MS7, we see that all are placed in the middle plane bounded with upper and lower layer dipoles, which put them in a configuration at the base of a triangle as the cases examined earlier. In contrast, MS8, MS9, MS11, and MS12 have positive loops and configurations similar to the dipole in the upper corner of the 2D triangle.

Looking at the local loops for MSs in the FCC structure with an interparticle distance of $r = 1.5d$ in Fig. 5.12, we see no inverted loops, which is expected for weaker dipole interactions, and we get a global loop with bigger area. These local loops appear to have more random shapes compared to $r = d$ on account of averaging of ten times fewer loops. Having our findings and the description of local loops from Munoz et al. [13] in mind, we conclude that although the global heating is less for $r = 1d$ compared to $r = 1.5d$, inverted local loops may mean high local heating near particular MSs. It would be interesting to apply the framework of Munoz et al. for calculating local heating to this configuration of MSs.

5.6 SR/α scaling for multiple NPs

In addition to coarse-graining and using an MS model, a useful technique for decreasing the calculation time is to simulate the magnetic system with a faster SR but keeping the ratio SR/α constant, in our case equal to the one arising from the clinically and physically appropriate parameters SR = 0.25 Oe/ns and $\alpha = 0.1$. A more detailed explanation of this equivalence can be found in I and here we test this technique for assemblies of NPs and MSs using OOMMF and Vinamax, respectively.

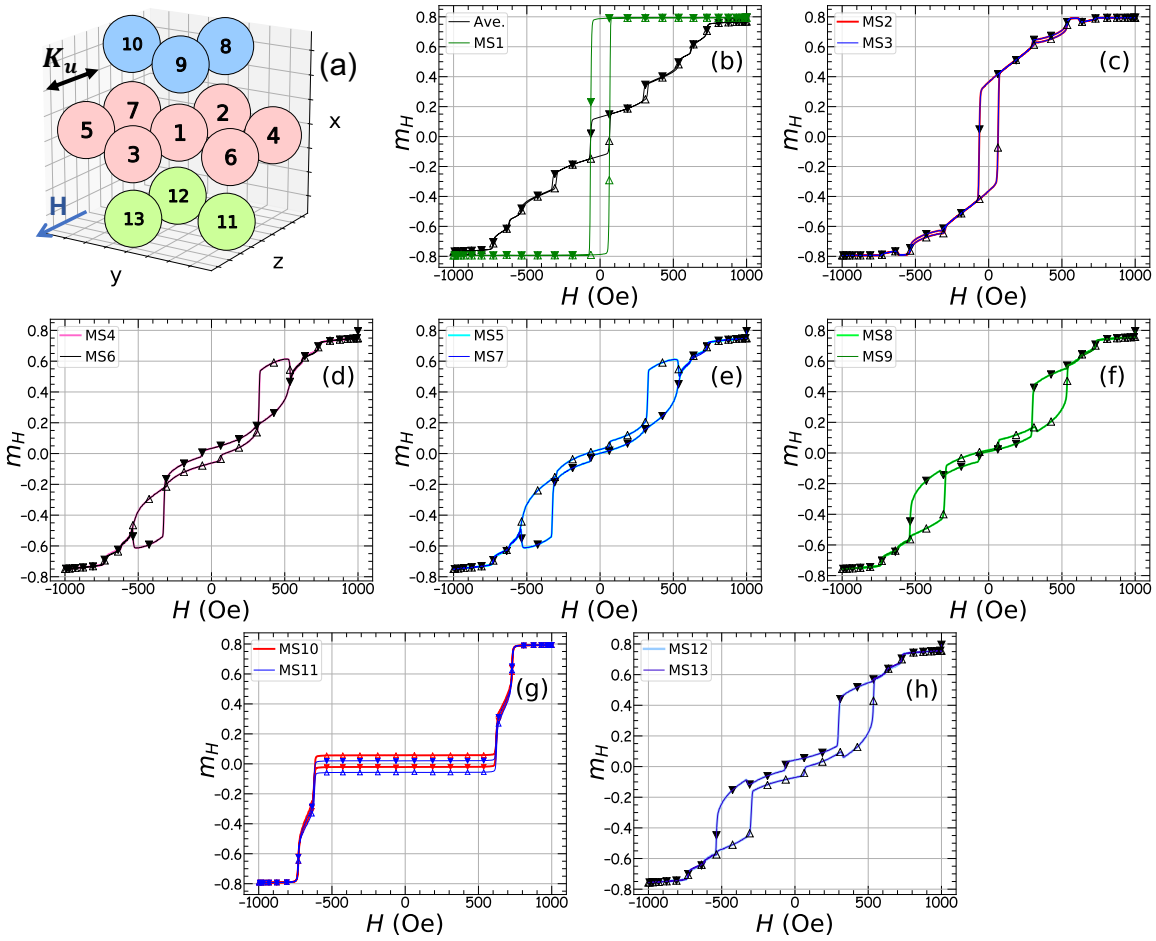

Figure 5.11: FCC structure made of 13 MSs, and their global and local hysteresis loops when particles are at the closest distance, $r = d$. Closed and open markers distinguish the first ($H_{\max} \to -H_{\max}$) and second ($-H_{\max} \to H_{\max}$) halves of a cycle, respectively. a) Labeled MSs on the particle arrangement having uniaxial anisotropy along the applied field. b) Global hysteresis loop for 13 MSs shown in black and the local loop for the central MS (labeled with 1 in a) in green. Local hysteresis loops for c) MS2 and MS3, d) MS4 and MS6, e) MS5 and MS7, f) MS8 and MS9, g) MS10 and MS11, h) MS12 and MS13 in the FCC structure as labeled in (a). Each loop is calculated via averaging over 1000 independence field cycles

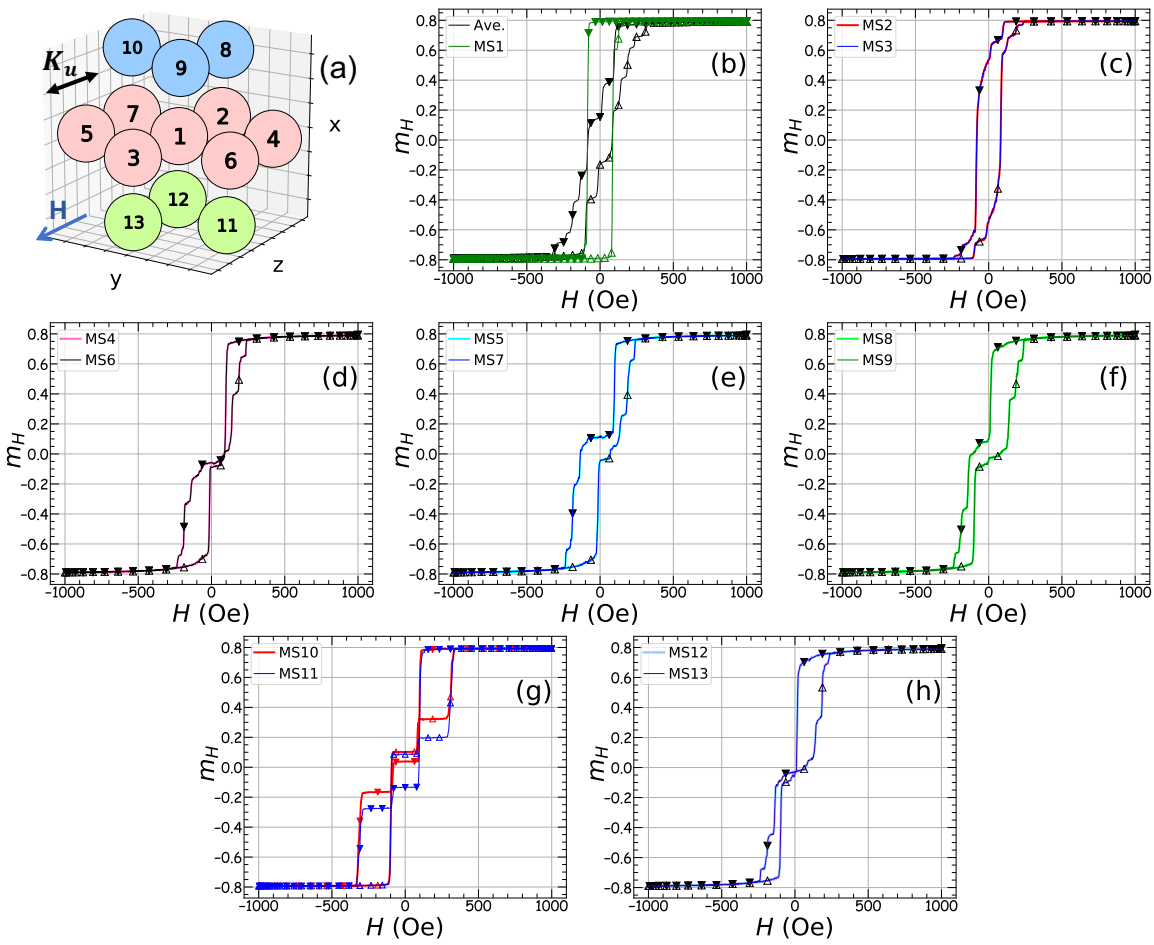

Figure 5.12: Global and local loops for 13 MSs making an FCC structure with uniaxial anisotropy along the applied field when $r = 1.5d$. a) Labeled MSs on the FCC structure. b) Average hysteresis loop for 13 MSs in black and the local loop for the central MS (MS1) shown in green. Local hysteresis loops for c) MS2 and MS3, d) MS4 and MS6, e) MS5 and MS7, f) MS8 and MS9, g) MS10 and MS11, h) MS12 and MS13 in the FCC structure as labeled in (a). Closed and open markers distinguish the first ($H_{\max} \to -H_{\max}$) and second ($-H_{\max} \to H_{\max}$) halves of a cycle, respectively. Each loop is calculated via averaging over 100 independence field cycles.

We start our investigation with NPs at the closest distance ($r = d$) in a triangular array. As shown in Fig. 5.13a, except for slight mismatches at the shoulders of the loop, we still get an acceptable loop agreement for loop areas with values 641, 663,

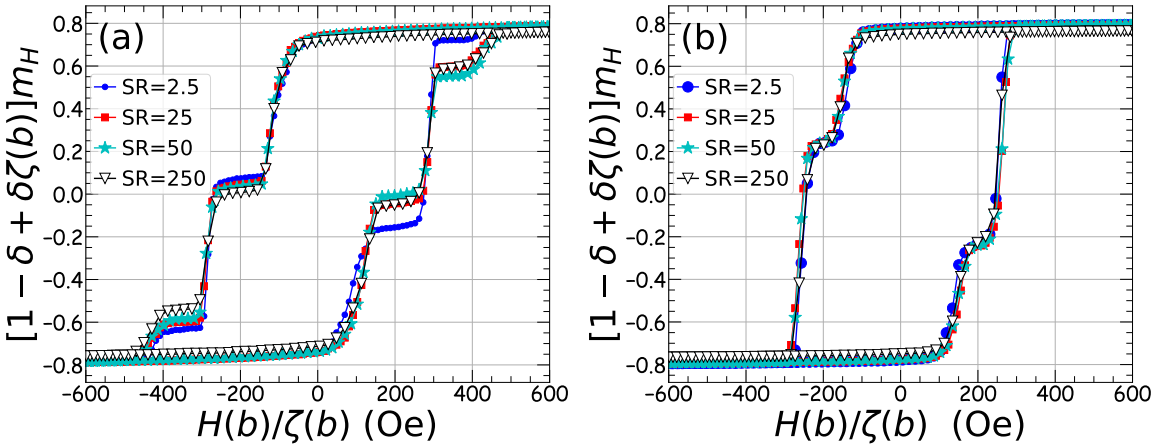

Figure 5.13: Test of SR/α scaling for three NPs (simulated in OOMMF) in triangular order with different separation a) $r = d$, b) $r = 1.5d$, where d is a NP diameter.

662, 637 Oe for SR = 2.5, 25, 50 and 250 Oe/ns, respectively. At higher particle separation, $r = 1.5d$, the loop agreement is even better over the two orders of magnitude of SR simulated; see Fig. 5.13b.

Testing Vinamax for validity of this technique, we first compare a single MS hysteresis loop over a range of SR and α values, and as shown in Fig. 5.14a, the limit of validity of this scaling appears to be SR = 1 Oe/ns, which is only four times faster than SR = 0.25 Oe/ns. This perhaps can be attributed to the numerical approach that Vinamax is based upon, the Dormand-Prince solver (an embedded Runge-Kutta method) [46], versus Euler for OOMMF. Moreover, a combination of three MSs in a triangular order simulated with Vinamax confirms the results that SR = 1 Oe/ns is the threshold of validity of the scaling using this software. The difference in the limits of applicability for the SR/α scaling technique for different numerical solvers is a matter of future investigation.

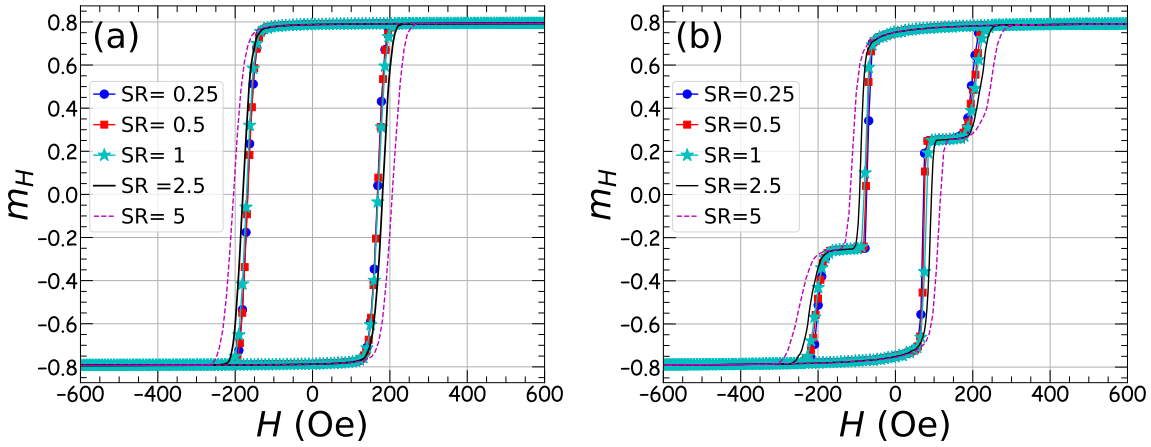

Figure 5.14: Test of SR/α scaling for simulations in Vinamax for a) a single MS, b) three MSs in triangular order, $r = d$.

5.7 Conclusions

This work reports on an application of the RG-based coarse-graining method, explored and extended in I and II, to simulate larger collections of magnetic nanoparticles that would otherwise not be numerically feasible, and examines the validity of the macrospin approximation. We apply this method to simulate dynamic hysteresis of clusters of three and thirteen magnetite complex nanoparticles, made of nanorod building blocks at $T = 310$ K.

We investigate a MS model, a macrospin having single or double uniaxial anisotropies with tailored anisotropy strength and saturation magnetization to produce equivalent hysteresis loops as a complex NP with the same volume. After finding the effective parameters for a single MS in II, we explore here whether a cluster of MSs is a good approximation for a cluster of complex NPs via their global hysteresis loops. We compare what we call their independence distance, the nearest-neighbour distance at which the cluster's global loop becomes approximately the same as for independent particles. For simulations of chains of three NPs and MSs, we find that the loop areas

in both cases scale in a similar way with interparticle distance, decaying as $1/r^3$ as one expects for dipoles. Also, MSs and complex NPs further apart than three NP diameter act as non-interacting particles. In contrast, for triangular order, the nontrivial effect of the interactions between complex NPs compared to the dipole effects between equivalent MSs results in dissimilar hysteresis loops for a range of interparticle distances. In this structure, MSs interact more strongly than NPs, as their independence distance is $5d$ compared to $2.5d$ for NPs. Similarly, for the FCC structure, the independence distance of MSs reaches $7d$ while, based on mild extrapolation of the apparent trend, it is roughly $3.5d$ for complex NPs.

We examined the local hysteresis loops of individual MSs in different clusters and compared their magnetization dynamics in terms of the dipole interactions they experience due to their location in a cluster. The appearance of inverted loops, while not directly yielding the degree of local cooling or heating, do signify significant work being done by NPs on each other, which can mean that local heating around NPs is uneven.

Most simulation studies of magnetic nanoparticles are based on the MS model. We explore and compare the MS model and complex NP model through micromagnetic simulations of dynamic hysteresis for three of many possible aggregations of magnetic particles. Noting that interparticle distance in clusters is controlled by many factors such as medium viscosity, temperature, particle shape, size and their coating shell thickness, our results suggest that the MS model, which approximates magnetostatic interactions with dipole interactions, does not reproduce the NP case for the more complex arrangements of the particles. Analyzing the loop area changes for clusters of particles at different particle distances and various configurations gives an idea of the negative or positive magnetostatics effects on their heating efficiency. It also

determines a threshold interparticle distance beyond which the impact of dipole interactions is negligible, and we find that the particles' magnetization dynamics is more entangled in more complex structures.

As far as using two anisotropy axes in the MS description of a NP, we do not see significant improvement at the level of a single particle. However, it would be worth testing whether having two anisotropies yields improvement in describing NPs in non-chain clusters, where the single-axis MS model breaks down at smaller interparticle distances.

We also looked at the loop area changes for a $6z4y$ NP when each cell's uniaxial anisotropy is drawn from a normal distribution with a standard deviation of θ degrees around the long axes of nanorods. This is to model the effect of natural variations in magnetic parameters, and we find a linear relation between the loop area and θ. Finally, the SR and α scaling technique for multiple particles is validated for both OOMMF and Vinamax, two micromagnetic software packages that we use here, although the scaling has a wider range of validity with OOMMF, which is likely due to the type of solver employed.

Acknowledgment

We thank Jonathan Leliaert for his guidance on employing the updated version of Vinamax. R.B. thanks Mikko Karttunen for hosting her stay at Western University. We acknowledge the financial support from the Natural Sciences and Engineering Research Council (Canada). Computational resources were provided by ACENET and Compute Canada.

Bibliography

[1] M. L. Plumer, J. van Lierop, B. W. Southern, and J. P. Whitehead. Micromagnetic simulations of interacting dipoles on an fcc lattice: application to nanoparticle assemblies. *J. Phys. Condens. Matter*, 22(29):296007, 2010.

[2] Y. Labaye, O. Crisan, L. Berger, J.-M. Greneche, and J. M. D. Coey. Surface anisotropy in ferromagnetic nanoparticles. *J. Appl. Phys.*, 91(10):8715–8717, 2002.

[3] Y. V. Kolen'ko, M. Bañobre-López, C. Rodríguez-Abreu, E. Carbó-Argibay, A. Sailsman, Y. Piñeiro-Redondo, M. F. Cerqueira, D. Y. Petrovykh, K. Kovnir, O. I. Lebedev, et al. Large-scale synthesis of colloidal Fe_3O_4 nanoparticles exhibiting high heating efficiency in magnetic hyperthermia. *J. Phys. Chem. C*, 118(16):8691–8701, 2014.

[4] Z. Surowiec, A. Miaskowski, and M. Budzyński. Investigation of magnetite Fe_3O_4 nanoparticles for magnetic hyperthermia. *Nukleonika*, 62, 2017.

[5] A. Villanueva, P. De La Presa, J. M. Alonso, T. Rueda, A. Martinez, P. Crespo, M. P. Morales, M. A. Gonzalez-Fernandez, J. Valdes, and G. Rivero. Hyperthermia hela cell treatment with silica-coated manganese oxide nanoparticles. *J. Phys. Chem. C*, 114(5):1976–1981, 2010.

[6] R. Hergt, R. Hiergeist, M. Zeisberger, D. Schüler, U. Heyen, I. Hilger, and W. A. Kaiser. Magnetic properties of bacterial magnetosomes as potential diagnostic and therapeutic tools. *J. Magn. Magn. Mater.*

[7] G. Shi, R. Takeda, S. B. Trisnanto, T. Yamada, S. Ota, and Y. Takemura. Enhanced specific loss power from Resovist® achieved by aligning magnetic easy axes of nanoparticles for hyperthermia. *J. Magn. Magn. Mater.*, 473:148–154, 2019.

[8] C. L. Dennis, A. J. Jackson, J. A. Borchers, P. J. Hoopes, R. Strawbridge, A. R. Foreman, J. Van Lierop, C. Grüttner, and R. Ivkov. Nearly complete regression of tumors via collective behavior of magnetic nanoparticles in hyperthermia. *Nanotechnology*, 20(39):395103, 2009.

[9] J.-H. Lee, J.-t. Jang, J.-s. Choi, S. H. Moon, S.-h. Noh, J.-w. Kim, J.-G. Kim, I.-S. Kim, K. I. Park, and J. Cheon. Exchange-coupled magnetic nanoparticles for efficient heat induction. *Nat. Nanotechnol.*, 6(7):418–422, 2011.

[10] H. A. Albarqi, L. H. Wong, C. Schumann, F. Y. Sabei, T. Korzun, X. Li, M. N. Hansen, P. Dhagat, A. S. Moses, O. Taratula, and O. Taratula. Biocompatible nanoclusters with high heating efficiency for systemically delivered magnetic hyperthermia. *ACS Nano*, 13(6):6383–6395, 2019.

[11] D. Chang, M. Lim, J. A. Goos, R. Qiao, Y. Y. Ng, F. M. Mansfeld, M. Jackson, T. P. Davis, and M. Kavallaris. Biologically targeted magnetic hyperthermia: Potential and limitations. *Front. Pharmacol.*, 9, 2018.

[12] P. Torche, C. Munoz-Menendez, D. Serantes, D. Baldomir, K. L. Livesey, O. Chubykalo-Fesenko, S. Ruta, R. Chantrell, and O. Hovorka. Thermodynamics of interacting magnetic nanoparticles. *Phys. Rev. B*, 101(22):224429, 2020.

[13] C. Muñoz-Menendez, D. Serantes, O. Chubykalo-Fesenko, S. Ruta, O. Hovorka, P. Nieves, K. L. Livesey, D. Baldomir, and R. Chantrell. Disentangling local heat contributions in interacting magnetic nanoparticles. *Phys. Rev. B*, 102(21): 214412, 2020.

[14] M. Anand. Hysteresis in a linear chain of magnetic nanoparticles. *J. Appl. Phys.*, 128(2):023903, 2020.

[15] N. A. Usov, O. N. Serebryakova, and V. P. Tarasov. Interaction effects in assembly of magnetic nanoparticles. *Nanoscale Res. Lett.*, 12(1):1–8, 2017.

[16] N. A. Usov and Y. B. Grebenshchikov. Hysteresis loops of an assembly of superparamagnetic nanoparticles with uniaxial anisotropy. *J. Appl. Phys.*, 106(2): 023917, 2009.

[17] N. A. Usov, S. A. Gudoshnikov, O. N. Serebryakova, M. L. Fdez-Gubieda, A. Muela, and J. M. Barandiarán. Properties of dense assemblies of magnetic nanoparticles promising for application in biomedicine. *J. Supercond. Nov. Magn.*, 26(4):1079–1083, 2013.

[18] R. Fu, Y. Yan, and C. Roberts. Study of the effect of dipole interactions on hyperthermia heating the cluster composed of superparamagnetic nanoparticles. *AIP Adv.*, 5(12):127232, 2015.

[19] J.-L. Déjardin, F. Vernay, and H. Kachkachi. Specific absorption rate of magnetic nanoparticles: Nonlinear AC susceptibility. *J. Appl. Phys.*, 128(14):143901, 2020.

[20] A. F. Bakuzis, L. C. Branquinho, L. Luiz e Castro, M. T. de Amaral e Eloi, and

R. Miotto. Chain formation and aging process in biocompatible polydisperse ferrofluids: Experimental investigation and Monte Carlo simulations. *Adv. Colloid Interface Sci.*, 191:1–21, 2013.

[21] D. P. Valdés, E. Lima Jr, R. D. Zysler, and E. De Biasi. Modeling the magnetic-hyperthermia response of linear chains of nanoparticles with low anisotropy: a key to improving specific power absorption. *Phys. Rev. Appl.*, 14(1):014023, 2020.

[22] R. E. Rosensweig. Heating magnetic fluid with alternating magnetic field. *J. Magn. Magn. Mater.*, 252:370–374, 2002.

[23] D. Serantes, K. Simeonidis, M. Angelakeris, O. Chubykalo-Fesenko, M. Marciello, M. D. P. Morales, D. Baldomir, and C. Martinez-Boubeta. Multiplying magnetic hyperthermia response by nanoparticle assembling. *J. Phys. Chem. C*, 118(11): 5927–5934, 2014.

[24] X. Feng and P. B. Visscher. Coarse-graining Landau–Lifshitz damping. *J. Appl. Phys.*, 89(11):6988–6990, 2001.

[25] M. Kirschner, T. Schrefl, F. Dorfbauer, G. Hrkac, D. Suess, and J. Fidler. Cell size corrections for nonzero-temperature micromagnetics. *J. Appl. Phys.*, 97(10): 10E301, 2005.

[26] M. Kirschner, T. Schrefl, G. Hrkac, F. Dorfbauer, D. Suess, and J. Fidler. Relaxation times and cell size in nonzero-temperature micromagnetics. *Physica B Condens. Matter*, 372(1-2):277–281, 2006.

[27] G. Grinstein and R. H. Koch. Coarse graining in micromagnetics. *Phys. Rev. Lett.*, 90(20):207201, 2003.

[28] R. Behbahani, M. L. Plumer, and I. Saika-Voivod. Coarse-graining in micromagnetic simulations of dynamic hysteresis loops. *J. Phys. Condens. Matter*, 32(35): 35LT01, 2020.

[29] R. Behbahani, M. L. Plumer, and I. Saika-Voivod. Multiscale modelling of magnetostatic effects on magnetic nanoparticles with application to hyperthermia. *J. Phys. Condens. Matter*, 33(21):215801, 2021.

[30] M. J. Donahue and D. G. Porter. *OOMMF User's Guide, Version 1.0, Interagency Report NISTIR 6376*. National Institute of Standards and Technology, Gaithersburg, MD, Sept 1999. URL `https://math.nist.gov/oommf/`.

[31] J. Leliaert, A. Vansteenkiste, A. Coene, L. Dupré, and B. Van Waeyenberge. Vinamax: a macrospin simulation tool for magnetic nanoparticles. *Med. Biol. Eng. Comput.*, 53(4):309–317, 2015.

[32] M. Anand, J. Carrey, and V. Banerjee. Spin morphologies and heat dissipation in spherical assemblies of magnetic nanoparticles. *Phys. Rev. B*, 94(9):094425, 2016.

[33] B. Mehdaoui, R. P. Tan, A. Meffre, J. Carrey, S. Lachaize, B. Chaudret, and M. Respaud. Increase of magnetic hyperthermia efficiency due to dipolar interactions in low-anisotropy magnetic nanoparticles: Theoretical and experimental results. *Phys. Rev. B*, 87(17):174419, 2013.

[34] C. Haase and U. Nowak. Role of dipole-dipole interactions for hyperthermia heating of magnetic nanoparticle ensembles. *Phys. Rev. B*, 85(4):045435, 2012.

[35] D. Cabrera, A. Coene, J. Leliaert, E. J. Artés-Ibáñez, L. Dupré, N. D. Telling, and F. J. Teran. Dynamical magnetic response of iron oxide nanoparticles inside live cells. *ACS Nano*, 12(3):2741–2752, 2018.

[36] G. T. Landi. Role of dipolar interaction in magnetic hyperthermia. *Phys. Rev. B*, 89(1):014403, 2014.

[37] M. Creixell, A. C. Bohórquez, M. Torres-Lugo, and C. Rinaldi. EGFR-targeted magnetic nanoparticle heaters kill cancer cells without a perceptible temperature rise. *ACS Nano*, 5(9):7124–7129, 2011.

[38] A. Riedinger, P. Guardia, A. Curcio, M. A. Garcia, R. Cingolani, L. Manna, and T. Pellegrino. Subnanometer local temperature probing and remotely controlled drug release based on azo-functionalized iron oxide nanoparticles. *Nano Lett.*, 13 (6):2399–2406, 2013.

[39] M. Colombo, S. Carregal-Romero, M. F. Casula, L. Gutiérrez, M. P. Morales, I. B. Böhm, J. T. Heverhagen, D. Prosperi, and W. J. Parak. Biological applications of magnetic nanoparticles. *Chem. Soc. Rev.*, 41(11):4306–4334, 2012.

[40] O. Lemcke. *ThetaEvolve for OOMMF release 1.2a3*, February 2004. `http://www.nanoscience.de/group_r/stm-spstm/projects/temperature/download.shtml`. See also `https://math.nist.gov/oommf/contrib/oxsext/oxsext.html`.

[41] R. Hergt and S. Dutz. Magnetic particle hyperthermia—biophysical limitations of a visionary tumour therapy. *J. Magn. Magn. Mater.*, 311(1):187–192, 2007.

[42] S. Dutz and R. Hergt. Magnetic nanoparticle heating and heat transfer on a microscale: basic principles, realities and physical limitations of hyperthermia for tumour therapy. *Int. J. Hyperth.*, 29(8):790–800, 2013.

[43] F. Heider and W. Williams. Note on temperature dependence of exchange constant in magnetite. *Geophys. Res. Lett.*, 15(2):184–187, 1988.

[44] P. G. Bercoff and H. R. Bertorello. Exchange constants and transfer integrals of spinel ferrites. *J. Magn. Magn. Mater.*, 169(3):314–322, 1997.

[45] M. S. Holden, M. L. Plumer, I. Saika-Voivod, and B. W. Southern. Monte Carlo simulations of a kagome lattice with magnetic dipolar interactions. *Phys. Rev. B*, 91(22):224425, 2015.

[46] J. R. Dormand and P. J. Prince. A family of embedded Runge-Kutta formulae. *J. Comput. Appl. Math.*, 6(1):19–26, 1980.

Chapter 6

Summary and future work

6.1 Summary

We present a coarse-graining method for simulating dynamic MH hysteresis loops of immobile magnetic nanoparticles (NPs) with complex internal structure, based on a previously reported renormalization-group approach. Our method enables one to simulate loops for multiple NPs at hyperthermia-relevant sweep rates (SR) in a reasonable simulation time that otherwise would take months using the computational resources available to us. Although we extend and apply the coarse-graining methodology to calculate the dynamic hysteresis loop of NPs composed of nanorods, it should be applicable to other magnetic systems at finite temperature.

The coarse-graining scheme enables simulating magnetic nanoparticle using larger, and thus fewer, simulation units than the atomic unit cells to get the MH hysteresis loops invariant with simulation cell size. It prescribes scaling of the magnetic parameters and interactions with the simulation cell size and temperature. This method was

initially introduced by Grinstein and Koch [1] and they reported its successful application for a 2D system that included Zeeman and exchange interactions. Our approach uses the formalism of Grinstein and Koch applied to a 3D system, and is modified to get a more accurate description of the temperature dependence of the magnetization. It is also extended to include magnetostatic interactions in addition to the Zeeman, exchange and magnetocrystalline anisotropy, which allows for simulating a wide range of magnetic systems.

Furthermore, we introduce a time scaling method that involves performing simulations with faster SR, along with an appropriately scaled damping factor α in the LLG equation, to produce equivalent results. This is useful since the slow (from the simulation perspective) sweep rates corresponding to hyperthermia applications are time consuming. We determine the range of validity for applying this technique to multiple complex NPs and MSs using both OOMMF and Vinamax software.

The importance of our approach can be summarized in three main points. First, using this coarse-graining method decreases the number of calculations and the simulation time by a factor up to 8^3. Second, one can benefit from using up to 10 times larger integration time steps with larger simulation cells. Third, the time scaling technique allows for simulations with up to 1000 times faster SRs.

Equipped with the time scaling and coarse-graining techniques, we model clusters of NPs comprised of nanorods – NPs similar to those used in an experimental study for treating human breast cancer in mice [2]. We simulate NPs at different levels, starting from nanorods, the building blocks of NPs, and then stacking them to form roughly 50 nm size NPs with different internal structures. Then we simulate clusters of NPs in chains, triangular and FCC configurations.

Simulating complex NPs enables us to evaluate the macrospin (MS) model, being

widely used in micromagnetic studies, as an approximation for NPs. We explore the primary idea of the MS model, in which the combined effect of exchange interactions, self-demag and magnetocrystalline anisotropy on the magnetization dynamics of a complex NP is modelled with a single magnetization vector subject to uniaxial anisotropy. By comparing hysteresis loops of NPs and MSs to get similar values for H_c and M_r, we find the effective magnetization and anisotropy constants for MSs corresponding to NPs with various internal structures.

Additionally, in particle clustering, the MS model approximates the magnetostatics between complex NPs with dipole interactions. Comparing hysteresis loops of NPs and MSs in clusters shows that the MS model breaks down in approximating the NPs' magnetization dynamics at small particle separations. Further investigation is recommended for finding MS-like models in this regime.

In order to better understand the magnetization dynamics of clusters of MSs, we evaluate their local hysteresis loops and see that owing to interparticle interactions we get inverted local loops. Further exploration of the energy exchange between MSs can answer some of the questions about local heating of individual particles and the effect on potential cancer treatments.

6.2 Future work

Our coarse-graining method is, in principle, applicable to other magnetic systems, for example, those with application to magnetic recording media [3]. It also provides a framework for a variety of possibilities to consider in order to find acceptable approximations for describing clusters of NPs. As we have already started exploring MSs with two uniaxial anisotropies for describing a single NP, it is worth looking into their

functionality in clusters of MSs.

Our procedure for finding effective MS parameters for both nanorods and NPs involves carrying out simulations of MSs with different values of K_{eff} and interpolating to find the value that yields the value of H_c obtained from detailed or coarse-grained simulations, essentially a fitting procedure. For nanorods, we hope to find a way of using the coarse-graining method to predict $M_{\text{s}}^{\text{eff}}$ and K_{eff} directly, without needing to fit. For NPs, predicting MS parameters is likely less straightforward, but examining trends in parameter values for different internal configurations of nanorods might yield useful guidance.

Another open task is to probe the effect of work exchange between clustered particles, and how it affects their local heating. This problem has been addressed from different aspects [4, 5] but a clear formalism for measuring this internal effect is still missing.

Surface anisotropy has not been included in our coarse-graining method but finding how to coarse-grain it and estimate its effect on NP magnetization dynamics is a potential research direction.

The key feature of magnetic NPs is their response to an applied magnetic field, and how their magnetization aligns with the applied field. This alignment can occur via different rotation mechanisms. The common process, used in this thesis, involves a particle's magnetic moment rotating inside the particle to align with the field through so-called Néel relaxation. The delayed aligning of the magnetic moment with the changing field is quantified through an MH hysteresis loop, and the enclosed area of the loop represents the amount of the magnetic energy added to the system, which is usually assumed to dissipate as heat. Another process involves the whole particle rotating to align its magnetic moment with the field. This is called Brownian rotation,

and the friction between NPs and the surrounding fluid molecules results in heating. The relevant process is determined by which reversal process occurs on a shorter time scale.

In the Néel process, the changing field alters the magnetization's stable positions. The energy minima are separated by an energy barrier due to crystalline and shape anisotropy. When the size of NPs is smaller than $15 - 20$ nm, thermal fluctuations provide the required energy for the magnetization to flip before the whole nanoparticle rotates. So, for these particles, Néel relaxation is dominant, and their Brownian rotation is usually ignored due to its longer relaxation time [6]. Various studies have used Néel-rotation particles for magnetic hyperthermia applications [6–8].

In contrast, for larger single domain nanoparticles, in the size range of $20 - 80$ nm, the Brownian and Néel relaxation times can be comparable [6]. In this case, a nanoparticle's rotation continuously changes the magnetization's relative alignment to the field and perturbs the internal rotation process. Therefore, the magnetization aligns with the field due to the coupling of the Néel and Brownian relaxation. Recently, Usadel [9] derived the differential equations for magnetization dynamics in this coupling process, but the methodology has not yet been applied in the context of hyperthermia, where the internal magnetization dynamics of NPs may be complex. Exploring this coupling process through simulations can be done from at least two perspectives. The first is to study systems at the nanoparticle level, where the magnetization of a mobile NP immersed in solvent is coupled to its rotational motion. Simulating mobile magnetic NPs may give more in-depth insight into nanoparticle functionality in the body and unveil potentials for more effective magnetic hyperthermia. The second is to study the coupling between magnetic and translational degrees of freedom at the atomic level, by which the process of magnetic heating is directly simulated. This kind of

fine-grained simulation will be limited in terms of spatial and temporal scales, but may, for example, provide hints on how to incorporate atomic-scale effects, such as those arising from defects, impurities and surfaces, into coarse-grained models.

Bibliography

[1] G. Grinstein and R. H. Koch. Coarse graining in micromagnetics. *Phys. Rev. Lett.*, 90(20):207201, 2003.

[2] C. L. Dennis, A. J. Jackson, J. A. Borchers, P. J. Hoopes, R. Strawbridge, A. R. Foreman, J. Van Lierop, C. Grüttner, and R. Ivkov. Nearly complete regression of tumors via collective behavior of magnetic nanoparticles in hyperthermia. *Nanotechnology*, 20(39):395103, 2009.

[3] M. D. Leblanc, J. P. Whitehead, and M. L. Plumer. Monte Carlo simulations of intragrain spin effects in a quasi-2D Heisenberg model with uniaxial anisotropy. *J. Phys. Condens. Matter*, 25(19):196004, 2013.

[4] P. Torche, C. Munoz-Menendez, D. Serantes, D. Baldomir, K. L. Livesey, O. Chubykalo-Fesenko, S. Ruta, R. Chantrell, and O. Hovorka. Thermodynamics of interacting magnetic nanoparticles. *Phys. Rev. B*, 101(22):224429, 2020.

[5] C. Muñoz-Menendez, D. Serantes, O. Chubykalo-Fesenko, S. Ruta, O. Hovorka, P. Nieves, K. L. Livesey, D. Baldomir, and R. Chantrell. Disentangling local heat contributions in interacting magnetic nanoparticles. *Phys. Rev. B*, 102(21):214412, 2020.

[6] R. E. Rosensweig. Heating magnetic fluid with alternating magnetic field. *J. Magn. Magn. Mater.*, 252:370–374, 2002.

[7] D. P. Valdés, E. Lima Jr, R. D. Zysler, and E. De Biasi. Modeling the magnetic-hyperthermia response of linear chains of nanoparticles with low anisotropy: a key to improving specific power absorption. *Phys. Rev. Appl.*, 14(1):014023, 2020.

[8] D. Cabrera, A. Coene, J. Leliaert, E. J. Artés-Ibáñez, L. Dupré, N. D. Telling, and F. J. Teran. Dynamical magnetic response of iron oxide nanoparticles inside live cells. *ACS Nano*, 12(3):2741–2752, 2018.

[9] K. D. Usadel and C. Usadel. Dynamics of magnetic single domain particles embedded in a viscous liquid. *J. Appl. Phys.*, 118(23):234303, 2015.

Appendix A

Magnetostatics Induced Shape Anisotropy

The goal of this appendix is to provide an outline of the calculation of the magnetostatically induced shape anisotropy of a magnetized particle. To do this, we first review the demagnetization tensor calculations and then compute the shape anisotropy constant corresponding to a rectangular prism. At the end, simulation results are reported that can be compared to our $T = 0$ calculations. Background material for this appendix is taken from Refs. [1–3].

A demagnetization field is defined as a magnetostatic field generated by the magnetization of an object. For a uniformly magnetized object, the demagnetization field can be defined in terms of a demagnetization tensor, $\mathbf{N}$ [1]. A uniform demagnetization field inside of a magnetized object can only be achieved in ellipsoids [2], and can be written in terms of the demagnetization tensor,

$$\mathbf{H} = -\mathbf{N} \cdot \mathbf{M}. \tag{A.1}$$

For shapes other than ellipsoids, a uniformly magnetized body does not produce a uniform internal field. In this case, Eq. A.1 still applies if we consider the internal field averaged over the volume of the object [1]. When we have two uniformly magnetized volumes v and v', which may overlap, with respective magnetizations $\mathbf{M}$ and $\mathbf{M}'$, the average field in v due to the magnetization in v' is,

$$\langle \mathbf{H} \rangle_v = -\mathbf{M}' \cdot \mathbf{N}, \tag{A.2}$$

where the i and j components of $\mathbf{N}$ are,

$$N_{ij} = -\frac{1}{4\pi v} \int_v dv \int_{v'} \nabla'_i \nabla'_j \left(\frac{1}{|\mathbf{r} - \mathbf{r}'|} \right) dv', \tag{A.3}$$

and the resulting energy in v due to v' is,

$$E_d = -\frac{\mu_0}{2} \mathbf{M} \cdot \mathbf{N} \cdot \mathbf{M}' v. \tag{A.4}$$

It should be noted that $\mathbf{N}$ depends on the distance between the two volumes, as well as their shapes and relative orientations.

For simulating a ferromagnetic body with nonuniform magnetization, we divide the body into smaller cells, such that each cell can be considered to have a uniform magnetization. To calculate the demagnetization field in the body we need to average over all the cells' demag fields. Each cell's demag field ($\mathbf{H}_i$) is a sum of the products of the magnetization and the demag tensor of all the cells of the body,

$$\mathbf{H}_i = -\sum_j \mathbf{N}(\mathbf{r}_i - \mathbf{r}_j) \cdot \mathbf{M}_j \tag{A.5}$$

where the sum is over all the cells in the body, including the i^{th} cell itself, and

$$\mathbf{N}(\mathbf{r}_i - \mathbf{r}_j) = \frac{1}{4\pi v_i} \int_{S_i} d\mathbf{S} \int_{S'_j} \frac{d\mathbf{S}'}{|\mathbf{r} - \mathbf{r}'|}. \tag{A.6}$$

$\mathbf{N}(\mathbf{r}_i - \mathbf{r}_j)$ is the demagnetization tensor calculated for source cell j and target cell i. The notation $\mathbf{N}(\mathbf{r}_i - \mathbf{r}_j)$ indicates the implicit dependence of $\mathbf{N}_{ij}$ on the distance between, and relative orientations and sizes of cells i and j.

For calculating the averaged demagnetization field at a target cell i, one approach is to consider the observing point at the center of cell i and use a point-function demagnetizing tensor. Another practice is to average over the point functions calculated at all the points of the target cell i. Fukushima et al. [3] worked out a set of formulas for calculating the demagnetization tensor components of a rectangular prism using the volume average approach. We employ their formulas for our nanorod model that has aspect ratios of $1 \times 3 \times 7$ along x, y and z, respectively, and obtain,

$$\mathbf{N}_{\mathbf{VolumeAve}} = \begin{bmatrix} 0.65992 & 0 & 0 \\ 0 & 0.24061 & 0 \\ 0 & 0 & 0.09947 \end{bmatrix}. \tag{A.7}$$

OOMMF also provides functionality for reporting the demagnetization tensor, and we confirm that we obtain the same numerical result using OOMMF.

Using Eq. A.4 to calculate the self-demagnetization energy, i.e., $v = v'$, $\mathbf{M} = \mathbf{M}'$, and using the fact that the demagnetization tensor is symmetric, the self-demagnetization

energy is,

$$E_d = -\frac{\mu_0 v}{2}\Big(M_x^2 N_{xx} + M_y^2 N_{yy} + M_z^2 N_{zz} + 2M_x M_y N_{xy} + 2M_x M_z N_{xz} + 2M_y M_z N_{yz} \Big). \tag{A.8}$$

The uniaxial anisotropy energy is $E = -K_u \sin^2\theta$, and we would like to write E_d in this form. Writing the components of $\mathbf{M}$ in terms of spherical coordinates as $M_x = M\sin\theta\cos\varphi$, $M_y = M\sin\theta\sin\varphi$ and $M_z = M\cos\theta$, and noting that $\mathbf{N}$ is diagonal in our case, E_d can be written up to a constant as [2],

$$\frac{E_d}{v} = -K_{\rm sh}\sin^2\theta, \tag{A.9}$$

with the shape anisotropy energy density given by,

$$K_{\rm sh} = \frac{\mu_0 M^2}{2}\left(N_{xx}\cos^2\varphi + N_{yy}\sin^2\varphi - N_{zz}\right). \tag{A.10}$$

Here, $K_{\rm sh}$ depends on the angle φ since $N_{xx} \neq N_{yy}$. However, the most probable direction of the magnetization corresponds to the value of φ at which $K_{\rm sh}$ is minimized. Finding the roots of the first derivative and sign of the second derivative of $K_{\rm sh}$ with respect to φ, for $N_{yy} < N_{xx}$ (i.e. prism is longer in y than in x), $\varphi = \pi/2$ and $3\pi/2$ (on $[0, 2\pi]$) give positions with the minimum energy for the magnetization. Substituting $\varphi = \pi/2$ in Eq. A.10 and demagnetization tensor values from Eq. A.7, we get the shape anisotropy energy density,

$$K_{\rm sh} = \frac{\mu_0 M^2}{2}(N_{\rm yy} - N_{\rm zz}) = 20432.074 = 20.4\ \text{kJ/m}^3. \tag{A.11}$$

As a first step in testing the above findings, we compare the coercivity of a block

having magnetostatic interactions (self-demag) with that of a macrospin with uniaxial anisotropy and anisotropy energy density $K_u = K_{\rm sh}$, the latter of which can be calculated analytically given the formalism presented in section 2.1. Fig. A.1a shows the coercivity as a function of θ_0 (field angle) obtained from simulating at $T = 0$ a nanorod modelled with a single micromagnetic cell and (self) magnetostatic interactions, and compares it to the coercivity given by Eq.2.3 for a macrospin; in both instances, the anisotropy and long nanorod axes are along z. The results are nearly identical, validating the value of $K_{\rm sh}$ obtained theoretically.

Also, the hysteresis loop obtained numerically for the (magnetized) nanorod matches that of the equivalent MS obtained analytically, when $\theta_0 = 0.1$ (a small deviation of the field direction away from the anisotropy axis is useful to induce a torque on $\mathbf{M}$) at $T = 0$, as shown in Fig. A.1b. At finite T, thermal fluctuations allow the magnetization to overcome the energy barrier and flip before the barrier disappears. Therefore, we get smaller H_c as compared to $T = 0$. As shown in Fig. A.1c, the overall effect of thermal fluctuations result in a larger effective shape anisotropy $K_u \simeq 22$ kJ/m^3 compared to the $T = 0$ value of $K_u = 20.5$ kJ/m^3. The larger value of the effective K_u at $T > 0$ may reflect the fact that at $T > 0$, the path of the magnetization does not pass through the saddle point on the energy surface exactly, but samples higher energies.

In summary, calculating the demagnetization tensor for a rectangular prism provides a way of modelling magnetostatic effect with a uniaxial shape anisotropy and calculating the effective anisotropy energy density, particularly at low T. At higher T, the precise value of the effective anisotropy energy must either be obtained numerically, or perhaps by a more detailed comparison of the φ dependence of the magnetization energy landscape for both the magnetized nanorod and MS.

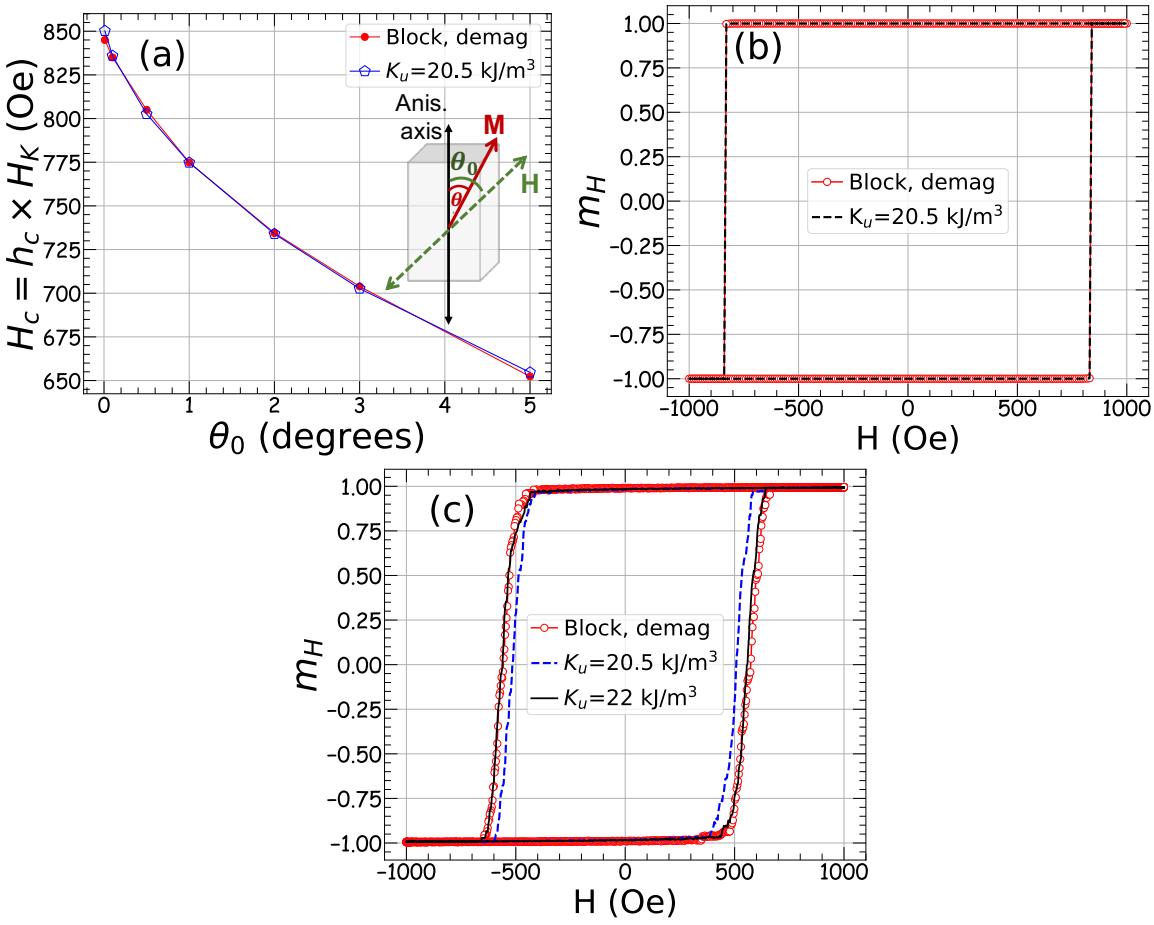

Figure A.1: a) Calculated H_c for a MS with $K_u = 20.5$ kJ/m^3 compared to the coercivity in the hysteresis loop of a block with magnetostatic interactions (demag) for different angles between the field and anisotropy axes. b) Equilibrium hysteresis loop of a block including self-demag and an equivalent MS with the same v, $M_s = 480$ kA/m and $K_u = 20.5$ kJ/m^3 at $T = 0$. c) Same as part b, except $T = 310$ K and simulations are performed with SR = 25 Oe/ns and α=10.

Bibliography

[1] A. J. Newell, W. Williams, and D. J. Dunlop. A generalization of the demagnetizing tensor for nonuniform magnetization. *J. Geophys. Res. Solid Earth*, 98(B6): 9551–9555, 1993.

[2] B. D. Cullity and C. D. Graham. *Introduction to magnetic materials*. John Wiley & Sons, 2011.

[3] H. Fukushima, Y. Nakatani, and N. Hayashi. Volume average demagnetizing tensor of rectangular prisms. *IEEE Trans. Magn.*, 34(1):193–198, 1998.